Plasmonic devices for surface optics and refractive index sensing

Benedikt Stein

Université de Strasbourg

École Doctorales des Sciences Chimiques

UMR n° 7006 : Institut de Sciences et d'Ingénierie Supramoléculaire

THÈSE

présentée par

Benedikt Alexander Hugo STEIN

soutenue le 3 Juillet 2012

pour obtenir le grade de

Docteur de l'université de Strasbourg

Discipline / Spécialité : Physique

Plasmonic Devices for Surface Optics and Refractive Index Sensing

Thèse dirigée par :
M. EBBESEN Thomas Prof. Dr., ISIS, Université de Strasbourg

Rapporteurs:
M. SANDOGHDAR Vahid Prof. Dr., Max-Planck-Institut für die Physik des Lichts
M. HECHT Bert Prof. Dr., Universität Würzburg

Président du jury:
M. HAACKE Stefan Prof. Dr., Université de Strasbourg

Résumé de Thèse

Ce manuscrit s'inscrit dans le contexte du contrôle de la propagation des plasmons de surface. A cet effet, des nanostructures diélectriques et métalliques ont été conçues et caractérisées par microscopie à champ de fuite dans les espaces réel et réciproque. La manipulation des plasmons de surface à l'aide de lentilles diélectriques et d'éléments à gradient d'indice est présentée, et la réfraction négative, la direction et l'auto-collimation des plasmons de surface dans des cristaux plasmoniques à une ou deux dimensions sont démontrées. Ces résultats ont été utilisés pour le guidage de nanoparticules à l'aide de forces optiques, ainsi que pour deux méthodes permettant de renforcer le facteur de mérite de sondes plasmoniques de variation d'indice de réfraction, basées l'une sur les résonances de Fano naturelles de la microscopie à champ de fuite, et pour la seconde sur les structures des bandes plasmoniques anisotropes.

La photonique est une technologie clé qui connait une grande variété d'applications, notamment dans les télécommunications, la fabrication industrielle, ou les sciences de la vie. Mais la diffraction limite en général les systèmes optiques à l'échelle de la longueur d'onde de la lumière. Afin de surmonter cette limite, le domaine de la plasmonique est devenu un domaine de la recherche très important ces dernières années en raison de sa capacité à confiner la lumière dans des dimensions sub-longueurs d'onde.

Les plasmons de surface sont des ondes électromagnétiques, couplées aux oscillations de charges sur les surfaces métalliques. En tant qu'onde de surface, un plasmon peut se propager librement le long d'une interface diélectrique-métal, tout en étant confiné à la surface avec des amplitudes du champ qui décroissent de façon exponentielle loin de celle-ci. Les plasmons de surface ont été décrits il y a plus d'un siècle par la théorie de Maxwell et le traitement des propriétés optiques des métaux de Drude, mais il a fallu attendre la fin des années 1950 pour que leur existence soit démontrée clairement. Les premières expériences ont rapidement suivi, menant à des applications immédiates pour la détection d'indice de réfraction et la spectroscopie Raman exaltée de surface, notamment.

Les recherches plasmoniques se sont accélérées deux décennies plus tard, avec l'apparition

d'outils permettant la nanofabrication, ainsi que de techniques d'imagerie donnant accès à l'optique en champ proche, telles que la microscopie optique en champ proche et la microscopie à champ de fuite. De nombreuses découvertes ont suivi, telles que la transmission extraordinaire, et les antennes optiques sub-longueurs d'onde. D'autres applications dans des domaines variés, tels que les circuits optiques ou la micromanipulation optique, ont été développées peu de temps après. Ce sont ces travaux fondateurs qui stimulent la recherche plasmonique actuelle, et qui ont généré le formidable développement de la plasmonique.

Parce que le domaine a acquis une certaine maturité, ces applications avancées nécessitent un contrôle précis des champs plasmoniques propageants. Des nanostructures complexes sont conçues pour étudier des phénomènes physiques fondamentaux, parmi lesquels, par exemple, l'optique de transformation des plasmons, les réseaux métalliques adaptés ou les géométries topologiquement chargées. C'est sur ce contrôle que les travaux présentés dans cette thèse se sont concentrés en concevant, en espace réel et réciproque, de divers composants optiques diélectriques et métalliques. La microscopie à champ de fuite a servi d'outil polyvalent, rapide et fiable pour la caractérisation de ces composants. En outre, il sera montré comment utiliser ce nouveau degré de contrôle pour la manipulation de nanoparticules d'or, et la conception de détecteurs de faibles variations d'indice de réfraction.

La première partie de ce manuscrit discute certains aspects de la théorie des plasmons de surface, l'état actuel de la recherche dans ce domaine, et les techniques expérimentales principales, donnant le cadre dans lequel s'intègrent les résultats présentés dans cette thèse.

Dans le chapitre 2, les principes fondamentaux des plasmons de surface sont abordés. Après une discussion sur les propriétés optiques des métaux, la relation de dispersion des plasmons de surface à l'interface d'un demi-espace métallique est étudiée par l'analyse des coefficients de réflexion de Fresnel. Cette méthode est étendue par la suite à des films métalliques minces, qui sont utilisés dans la plupart des expériences de cette thèse, et la dépendance de la longueur de propagation des plasmons de surface à l'épaisseur du film métallique est étudiée.

Après uns discussion sur les composants optiques en deux dimensions pour les plasmons de surface, les techniques de couplage de la lumière aux plasmons de surface sont abordées, notamment dans le cas du couplage à l'aide de nanostructures. La dépendance de la distribution du champ plasmonique à la forme des nanostructures et au champ incident

est calculée à l'aide d'un modèle de Huygens-Fresnel et les distributions du champ obtenues pour une variété de configurations sont présentées. Les méthodes pour contrôler la propagation des plasmons de surface sont également rappelées.

Enfin, le domaine de la détection des variations d'indice à base de plasmons de surface est introduit. Un aperçu des régimes de sondage possibles et des instruments de mesure correspondants est donné. En outre les définitions de paramètres de performance tels que la sensibilité, la résolution et le facteur de mérite de la sonde sont rappelées.

Dans le chapitre 3, la microscopie à champ de fuite, qui sera la méthode retenue pour la plupart des caractérisations expérimentales dans cette thèse, est discutée en détails. Un bref rappel est fait de certaines autres techniques d'imagerie, notamment le montage d'imagerie par fluorescence, mis-en-place dans le cadre de cette thèse.

Les propriétés de la microscopie à champ de fuite sont ensuite présentées avec l'imagerie dans l'espace réciproque et les techniques de filtrage. Les interférences entre la transmission, la diffraction directe et la radiation de fuite des plasmons lancés par des nano-ouvertures illuminées sont examinées dans les espaces réel et réciproque. De plus, l'optimisation de l'épaisseur du film pour la microscopie à champ de fuite est abordée.

On présente enfin le montage optique qui a été mis en œuvre dans le cadre de cette thèse, ainsi que certaines fonctionnalités particulières, telles que l'extension à la détection d'indice et à l'imagerie à grande gamme dynamique.

Dans la deuxième partie de ce manuscrit sont introduits les composants optiques de surface qui permettent de contrôler de plusieurs façons le flux des plasmons de surface propageants.

Les éléments optiques homogènes tels que les prismes et les lentilles ont été fabriqués au cours de cette thèse par lithographie électronique sur des films de polymère, et sont présentés dans le chapitre 4. L'approche a été étendue à la conception d'un métamatériau fait de tiges de polymère. Un tel système a rendu possible une dépendance spatiale de l'indice de réfraction effectif pour les plasmons de surface. Les prismes et les lentilles à gradient d'indice pourraient être créés à l'aide de cette approche. En outre, les structures à gradient d'indice pourraient être utilisées pour permettre une transition progressive à des dispositifs diélectriques homogènes, ceci afin de s'attaquer à l'un des problèmes majeurs de ces structures, qui est la perte par diffusion sur des interfaces à forte variation d'indice. Les résultats présentés dans ce chapitre ont été publiés dans la revue Optics Express en 2010 [1].

Chapitre 5 présente les composants métalliques diffractifs, constitués de réseaux sinusoïdaux

à une et deux dimensions. Le couplage des différents ordres de diffraction dans ces réseaux conduit à la formation de bandes interdites pour les plasmons. L'influence de la modulation d'amplitude du réseau sur les pertes lors de la propagation et sur la largeur de la bande interdite est d'abord étudiée, puis la mise en œuvre des miroirs de Bragg simples est décrite.

Le voisinage de la bande interdite a été exploité afin de contrôler des faisceaux plasmoniques dans les réseaux à une et deux dimensions, un équivalent plasmonique de l'effet superprisme des cristaux photonique. Cet effet est expliqué par l'analyse des diagrammes isofréquence des réseaux, calculés théoriquement et mesurés expérimentalement. La courbure inversée de ces diagrammes se révèle également être la cause d'une réfraction négative des faisceaux de plasmons de surface, sans indice de réfraction négative.

Les structures de bandes ont été ajustées spécifiquement afin de créer des régions plates isolées dans l'espace réciproque. On montre alors que les plasmons de surface dans de tels réseaux possèdent des propriétés d'auto-collimation. En utilisant une imagerie à grande gamme dynamique, on a pu montrer une propagation des plasmons de surfaces sans diffraction sur des distances jusqu'ici jamais atteintes. Les résultats présentés dans ce chapitre ont été publiés dans la revue Physical Review Letters en 2010 et dans la revue Optics Letters en 2012 [2, 3].

Dans le chapitre 6, ce contrôle de la propagation des plasmons de surfaces a été appliqué pour obtenir un contrôle dynamique de trajectoires de nanoparticules métalliques. La déviation du vecteur de Poynting plasmonique provoquée par les plasmons de surface négativement réfractés se révèle être un moyen de déplacer les nanoparticules métalliques dans une large gamme de directions. Afin d'observer ces effets, un montage de couplage avec un prisme dédié et une imagerie sur fond noir des nanoparticules a été mis en œuvre dans le laboratoire. Un article présentant les résultats de ce chapitre a été publié dans la revue Nano Letters en 2012 [4].

Dans la troisième et dernière partie de cette thèse, la microscopie à champ de fuite est présentée en tant qu'outil pour la détection plasmonique des variations d'indice de réfraction.

L'asymétrie des résonances de Fano présentée dans le chapitre 7 permet d'améliorer les facteurs de mérite des sondes utilisant les plasmons de surface. Ces résonances apparaissent naturellement comme images réciproques des plasmons de surfaces lancés à partir de nano-ouvertures, découlant de l'interférence entre les champs diffractés et la radiation de fuite. Le niveau de sensibilité atteignable a été analysé en fonction de l'épaisseur du film,

et comparé à une simple Lorentzienne ou aux profils de réflexion totale interne atténuée couramment utilisés.

En utilisant des solutions aqueuses avec des concentrations d'éthanol différentes comme références pour l'indice de réfraction, une expérience de détection à haute résolution est présentée pour les profils optimisés. Une augmentation du facteur de mérite de 75% par rapport aux conditions optimales de la réflexion totale atténuée est démontrée. Une analyse détaillée du bruit du système nous permet d'estimer que la résolution de la sonde est de l'ordre de 10^{-7} unités d'indice de réfraction, ce qui est comparable aux meilleurs systèmes connus jusqu'à ce jour. Les résultats présentés dans ce chapitre ont été publiés dans la revue Journal of Physical Chemistry C en 2012 [5].

Dans le chapitre 8, ce n'est pas le profil de résonance, mais la dispersion des plasmons de surface elle-même qui est modifiée pour améliorer la performance de la sonde. L'anisotropie des structures de bande, observée dans les diagrammes d'isofréquence en espace réciproque, montre une capacité à améliorer la sensibilité à l'indice de réfraction dans un schéma d'interrogation du vecteur d'onde. Utilisant l'imagerie défocalisée en espace réciproque, on montre une amélioration des facteurs de mérite pour cette géométrie de la sonde. En utilisant à nouveau des solutions aqueuses d'éthanol en tant que références pour l'indice de réfraction, une expérience de détection à haute-résolution a été effectuée, et des résolutions de détection de l'ordre de 10^{-6} ont été obtenues. Une publication du contenu présenté dans ce chapitre est en préparation.

Les résultats de cette thèse et leur impact éventuel sont résumés dans ce chapitre de conclusion. Les perspectives pour de futures directions de recherche sont discutées.

Acknowledgments

First and foremost I would like to thank my supervisor Prof. Thomas W. Ebbesen for giving me the opportunity to join his laboratory, and to enjoy the outstanding resources at ISIS. His support, guidance and advice helped me growing as a scientist as well as a human being.

I would also like to especially thank Dr. Cyriaque Genet. He was always available for discussion and sharing ideas, and his enthusiasm and excitement were a constant source of motivation and inspiration.

I want to express my gratitude to Prof. Bert Hecht, Prof. Vahid Sandoghdar and Prof. Stefan Haacke for accepting to be on my thesis jury, and for the interest they showed in my work.

For offering me the possibility to teach with him for one semester in Karlsruhe, and for participating in my thesis defense, I would like to thank Prof. Uli Lemmer. Furthermore I would like to thank Prof. Kenneth Crozier, Prof. Jelena Vučković, Prof. Serge Haroche, and Dr. Geoffrey Burr for giving me the opportunity to join their laboratories during my undergraduate studies. The rich experience I could gather during that time finally motivated me to pursue a PhD in the fascinating field of nano-photonics.

I am moreover indebted to Dr. Eloise Devaux, who had the knowledge and patience that kept our nanofabrication tools breathing, and to Marie-Claude Jouaiti, who was always a step ahead of any administrative issues. For his help with first steps in microfluidics fabrication, I moreover want to thank Dr. Christian Rick, as well as Dr. Oliver Vogel and Chiara Musumeci for their help with AFM imaging.

I want to extend my gratitude to all members of the nanostructures laboratory. In particular, I would like to thank Dr. Jean-Yves Laluet for teaching me some essential experimental techniques, and for always having an open door during my first months in the lab. I would also like to thank my long term office mates Oussama Mahboub, Emmanuel Lombard and Juemin Yi, as well as Frédéric Przybilla, Eric Laux, Aurélien Drezet, Adi Salomon, Tal Schwartz, James Hutchison, Deirdre O'Carroll, Yuri Gorodetski, Aurélien

Cuche, Antoine Canaguier-Durand, Shaojun Wang, Gabriel Schnoering, Jino George, and Nina Matoussevitch, and moreover all members of Prof. Paolo Samori's group, for the warm and intercultural everyday atmosphere. Together with the other members of ISIS, especially the 7 pm cafeteria group, you made this a great place to work and live.

My friends off-campus, I want to thank for reminding me that there is a world outside the laboratory. Especially I want to thank Dr.-Ing. Matthias Wissert for proof-reading my manuscript and for sharing PhD student life across borders.

I would also like to express my gratitude to the *Studienstiftung des deutschen Volkes* and the *Stiftung der Deutschen Wirtschaft* for funding my doctoral studies, and for giving me the opportunity to join their PhD symposia, which allowed me to develop a broader view of the beautiful world of science beyond physics.

Finally, I want to thank my parents for their patience and unconditional support, and I want to thank Judith for her love, and for the understanding she showed over the past years.

List of Publications

Journal Publications

Work covered in this thesis:

- **B. Stein**, E. Devaux, C. Genet, T.W. Ebbesen, *Plasmonic crystal based refractive index sensing*, in preparation
- A. Cuche, **B. Stein**, A. Canaguier-Durand, E. Devaux, C. Genet, and T. W. Ebbesen, *Brownian motion in a designer force field: dynamical effects of negative refraction on nanoparticles*, Nano Lett. **12**, 8 (2012)
- **B. Stein**, E. Devaux, C. Genet, T.W. Ebbesen, *Self-collimation of surface plasmon beams*, Opt. Lett. **37**, 11 (2012)
- **B. Stein**, J.-Y. Laluet, E. Devaux, C. Genet, T.W. Ebbesen, *Fano resonances and leakage radiation for high-resolution plasmonic sensing*, J. Phys. Chem. C **116**, 10 (2012)
- **B. Stein**, J.-Y. Laluet, E. Devaux, C. Genet, T.W. Ebbesen, *Surface plasmon mode steering and negative refraction*, Phys. Rev. Lett. **105**, 266804 (2010)
- E. Devaux, J.-Y. Laluet, **B. Stein**, C. Genet, T.W. Ebbesen, *Refractive micro-optical elements for surface plasmons: from classical to gradient index optics*, Optics Express **18**, 20 (2010)

Other publications:

- Y. Gorodetski, K. Y. Bliokh, **B. Stein**, C. Genet, N. Shitrit, V. Kleiner, E. Hasman, T.W. Ebbesen, *Weak measurements of light chirality with a plasmonic slit*, Phys. Rev. Lett. **109**, 013901 (2012)
- A. Hohenau, J. R. Krenn, A. Drezet, O. Mollet, S. Huant, C. Genet, **B. Stein**, T.W. Ebbesen, *Surface plasmon leakage radiation microscopy at the diffraction limit*, Optics Express **19**, 25 (2011)

Oral Conference Presentations

- **B. Stein**, E. Devaux, C. Genet, T.W. Ebbesen, *High-resolution plasmonic sensing by leakage radiation microscopy*, to be presented at O10.6, **E-MRS 2012 Spring Meeting**, Strasbourg, France, (17/05/2012)
- **B. Stein**, E. Devaux, C. Genet, T.W. Ebbesen, *Self-collimation, steering and negative refraction of surface plasmon beams*, to be presented at N11.5, **E-MRS 2012 Spring Meeting**, Strasbourg, France, (17/05/2012)
- **B. Stein**, J.-Y. Laluet, E. Devaux, C. Genet, T.W. Ebbesen, *Steering and negative refraction of surface plasmon polariton beams*, DS37.1, O41.1, **75th Annual Meeting of the DPG and DPG Spring Meeting**, Dresden, Germany, (16/03/2011)
- **B. Stein**, J.-Y. Laluet, E. Devaux, C. Genet, T.W. Ebbesen, *Surface plasmon mode steering and negative refraction*, THU4oBis.1 (91), **3rd International Topical Meeting on Nanophotonics and Metamaterials (Nanometa)**, Seefeld, Austria (6/1/2011)
- **B. Stein**, J.-Y. Laluet, E. Devaux, C. Genet, T.W. Ebbesen, *Control of surface plasmon propagation by refractive micro-optical elements*, MC28O6, **12ème Journée de la Matière Condensée**, Troyes, France (26/08/2010)

Contents

1 Preface

Since the development of the laser in 1960, photonics has grown into a key technology, which found widespread application from telecommunications and industrial manufacturing to the life sciences. However, optical systems are typically limited to lengthscales of the wavelength of light because of diffraction. As one way of overcoming these limitations, the field of plasmonics has gained great interest in the past years due to its capability of localizing light to subwavelength dimensions.

Surface plasmons (SPs) consist of electromagnetic waves at optical frequencies which are coupled to charge oscillations on the surfaces of metal films. While as a surface wave an SP can freely propagate along the dielectric-metal interface, it is trapped normal to the surface with exponentially decaying field strengths. Surface plasmons could in principle have been fully described by Maxwell's theory and Drude's treatment of the optical properties of metals more than a century ago. However, it took until the late 1950s until their excitance was proposed. First experiments followed rapidely, leading to applications of the concentrated SP field for refractive index sensing and surface enhanced Raman spectroscopy.

Plasmonic research flourished two decades later at the advent of suitable nanofabrication tools, as well as imaging techniques which gave access to the optical near-field, such as scanning near-field optical microscopy and leakage radiation (LR) microscopy. This opened the way to a variety of breakthrough inventions, such as extraordinary light transmission through subwavelength holes and optical antennas. Other applications in a variety of fields, such as optical circuitry or optical micromanipulation, were found soon after. It is these promises that drive today's SP research, and that have inspired the tremendous development plasmonics experienced over the past two decades.

As the field has left its infancy, such advanced applications require precise control over propagating plasmon fields. Complex nanostructures are being designed for this purpose exploring fundamental physical phenomena, among which, e.g., plasmon transformation optics, taylored metal gratings, or topologically charged geometries.

It is this control that the work presented in this thesis tried to extend by real and reciprocal space design of novel dielectric and metallic surface optical components. Leakage radiation microscopy served as a versatile, fast and reliable tool for the characterization of these components. Moreover, it will be shown how to put this novel degree of control to use for the manipulation of gold nanoparticles, and the design of advanced SP refractive index senors.

In the first part of this thesis a selection of theoretical fundamentals, experimental techniques and the current state of the art of surface plasmon photonics will be discussed, setting the frame in which the results achieved during this thesis have been carried out: In **chapter 2** a brief review of surface plasmon photonics will be given. After a discussion of the optical properties of metals, the complex dispersion relation of surface plasmons on thick and thin metal films will be derived, and characteristic parameters will be examined. Strategies of surface plasmon excitation will be analyzed in the following, with special attention on nanostructure coupling techniques. A Huygens-Fresnel model describing SP excitation will be presented alongside, and methods to mold SP flow by dedicated source fields and structures will be introduced. Subsequently, techniques of controlling SP flow will be recalled. Finally, the fundamentals of SP refractive index sensing will be summarized, including a review of sensor instrumentation and related performance parameters.

As the major tool of analysis used throughout the presented work, surface plasmon imaging by leakage radiation microscopy will be discussed in **chapter 3**. Real and reciprocal space imaging and filtering techniques will be examined. The designed optical setup will be presented, and customized features for LR based refractive index sensing and high dynamic-range imaging will be introduced.

The second part of this manuscript covers the major results on two-dimensional surface optical devices which have been obtained during this thesis: First in **chapter 4** refractive optical elements for surface plasmons will be presented, such as homogeneous dielectric prisms and lenses. Subsequently a metamaterial consisting of polymer rods on metal will be introduced. It will be shown how, using such a material, the effective refractive index of surface plasmons can be tailored and spatially varied at will. The implementation of resulting gradient index prisms, lenses and waveguides will be discussed, and it will be demonstrated how gradient transitions can reduce scattering losses on structure interfaces.

In **chapter 5**, devices based on one- and two-dimensional metal gratings will be introduced for passive manipulation of SP fields. The bandstructure of SPs in such gratings will

be analyzed in detail, and the influence of grating modulation amplitudes on losses and SP bandgaps will be investigated. After a demonstration of simple SP Bragg mirrors, tailored bandstructures will be shown to lead to SP steering and negative refraction in such gratings. Moreover, doubly periodic gratings have been engineered to possess flat bandstructures, leading to self-collimating propagation of plasmon beams.

The achieved control over the flow of plasmon energy by redirection of the SP Poynting vector will be applied in **chapter 6** for the routing of metal nanoparticles. Propulsion of large ensembles of such particles in a wide range of directions by only weak modifications of the optical excitation conditions will be demonstrated.

In the last part of this manuscript, leakage radiation microscopy will be introduced as a tool for plasmonic refractive index sensing: In **chapter 7** asymmetric Fano lineshapes, which are natural to reciprocal space leakage radiation images of plasmons launched from nanoapertures, will be used to improve the sensitivity and figure of merit of refractive index sensors. A high-resolution sensing experiment will be presented, revealing refractive index resolutions on the order of 10^{-7}.

A complementary approach will be presented in **chapter 8**, in which not the resonance profile, but the SP dispersion relation itself has been optimized. The anisotropic bandstructure of SP Bloch modes in sinusoidal gratings, as observed in steering experiments, will be shown to lead to increased sensing sensitivities.

The achieved results will be summarized in the concluding **chapter 9**, and prospective directions of future research will be developed.

Part I.

Fundamentals

2 Surface Plasmon Polaritons

In this first chapter the fundamentals of surface plasmon (SP) photonics will be discussed. The optical properties of bulk metals, as well as basic principles of SPs on thick and thin metal films will be reviewed. Calculations of SP dispersion relations together with propagation lengths for the configurations implemented in this thesis will be presented.

Subsequently, an overview of recent progress in two-dimensional SP surface optics will be given, emphasizing nanostructure coupling techniques that are used extensively in this thesis. A Huygens-Fresnel model for SP excitation and propagation will be presented. The properties of different nanostructure sources will be discussed with the help of experimental as well as theoretical results.

The chapter will close with an introduction to SP based refractive index sensing. Optical instrumentation of such sensors will be reviewed, and sensing performance parameters will be introduced, which will appear to be reaching their theoretical limits.

2.1. Surface Plasmon Theory

Surface plasmons are coupled oscillations of the electromagnetic field and the free electron gas at a metal-dielectric interface. Of particular interest for this thesis are the properties of SPs on thin metal films. They will be described through the analysis of the Fresnel reflection coefficients on dielectric-metal-dielectric layer systems in the last part of this section. Optical properties of bulk metals, which will be required for all further calculations, as well SPs on single metal-dieletric interfaces will be discussed beforehand.

2.1.1. Optical Properties of Metals

Most of the effects discussed throughout this thesis rely on the frequency dependent complex permittivity $\varepsilon(\omega)$ of metals. These can be described to a wide extent by a

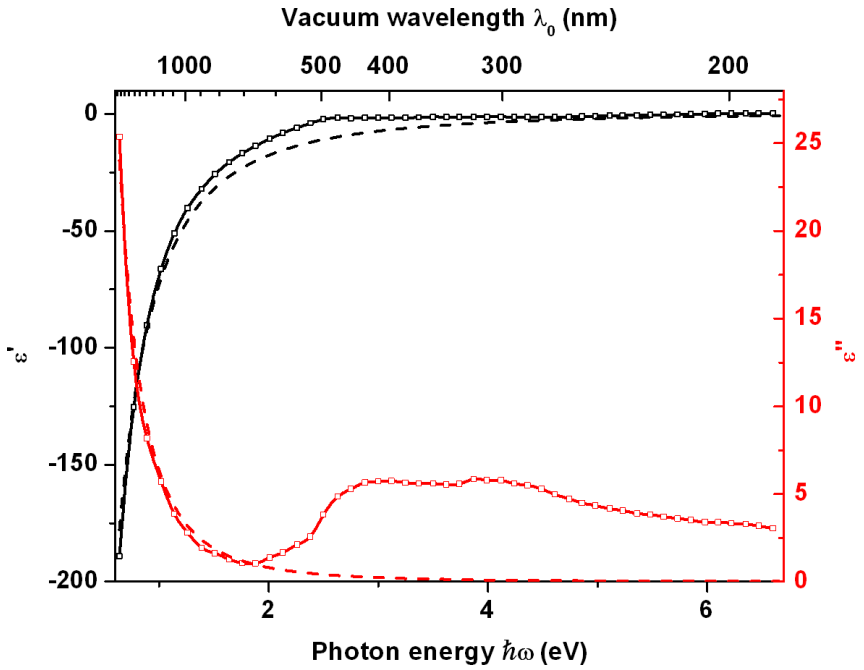

Figure 2.1.: Frequency dependent complex permittivity $\varepsilon(\omega) = \varepsilon'(\omega) + i\varepsilon''(\omega)$ of gold: Experimental data (squares) was taken from [6] interpolated by cubic splines (solid lines). The free-electron contribution (dashed) was calculated according to the Drude model with a plasma frequency $\omega_{\mathrm{p,\,Au}} = 8.63$ eV$/\hbar$ and a damping rate $1/\tau = 86.0$ meV$/\hbar$, extracted from fits to experimental data in the infrared.

free-electron gas model, which will be addressed in the first part of this section. In the visible range, however, mostly interband transition dominate, which will be discussed in the second part.

Drude-Sommerfeld Model

In the following, the results of classic solid-state theory of metals will be recalled. Extended treatments can be found in [7–10]. In 1900, Drude described electrons in the conduction band of metals in analogy to kinetic gas theory. Electrons were assumed to move like free particles which collide with lattice defects, impurities, phonons or other electrons at a total scattering rate $1/\tau$ [11]. Of the latter, electron-phonon scattering was found to dominate noble metal properties at ambient temperatures [12].

Sommerfeld extended this classic picture to quantum-mechanics by incorporating Fermi-Dirac statistics for electrons [13]. As these statistics allow only electrons close to the Fermi energy to scatter, τ can be understood as the relaxation time of the electron gas at the Fermi energy. Effects of the bandstructure are incorporated in assigning an effective

mass m^* to the electrons. Assuming an incident electric field applying a force on the charges inside the solid, and further neglecting movement of the metal ion lattice and frequency-dependence of the scattering rate $1/\tau$, the movement of the electron gas can be described in a semi-classical approach as

$$m^*\ddot{\mathbf{r}} + \frac{m^*}{\tau}\dot{\mathbf{r}} = -\mathrm{e}\mathbf{E}. \tag{2.1}$$

Here $\mathbf{E}$ is the driving electric field, $\mathbf{r}$ the charge displacement, and e is the elementary charge. Note that, contrary to the Lorentz model of charge oscillation in dielectrics, there is no restoring force included in equation (2.1), which represents the free character of the electron gas.

The microscopic displacement of the free electron gas results in a macroscopic polarization $\mathbf{P} = -n\mathrm{e}\mathbf{r}$, with the free charge carrier density n. Solving the equation of motion for a harmonic driving field $\mathbf{E} = \mathbf{E}_0 e^{-i\omega t}$ and recalling the definition of the permittivity in a linear, homogeneous and isotropic material as $\mathbf{D} = \varepsilon_0\mathbf{E} + \mathbf{P} = \varepsilon_0\varepsilon\mathbf{E}$, one finds

$$\varepsilon(\omega) = 1 - \frac{\omega_\mathrm{p}^2}{\omega^2 + i\omega/\tau} = \left[1 - \frac{\omega_\mathrm{p}^2}{\omega^2 + 1/\tau^2}\right] + i\left[\frac{\omega_\mathrm{p}^2/\tau}{\omega\left(\omega^2 + 1/\tau^2\right)}\right]. \tag{2.2}$$

Here $\omega_\mathrm{p}^2 = n\mathrm{e}^2/\varepsilon_0 m^*$ describes the resonance frequency of the electron gas, the so called plasma frequency. The longitudinally polarized charge oscillations associated with this frequency are also commonly termed bulk or volume plasmons.

Most experiments carried out as part of this thesis have been performed on evaporated gold films. From fits to experimental data for bulk gold in the infrared a typical value of $\omega_\mathrm{p} = 8.63$ eV$/\hbar$ has been extracted. Together with a scattering rate of $1/\tau = 86.0$ meV$/\hbar$, the resulting permittivity $\varepsilon(\omega) = \varepsilon'(\omega) + i\varepsilon''(\omega)$ of gold is depicted in Fig. 2.1. Note the large negative real part ε' at the depicted energies. It is responsible for the high reflectivity of gold at visible frequencies and below, and turns out essential for the existence of SP modes.

Empirical Permittivity of Bulk Gold

The extraction of the permittivity of gold from a free-electron gas model, just discussed, has its limitations, as can be seen in Fig 2.1, where are also plotted the experimental data of Johnson and Christy [6]. While for low energies the free-electron model seems to reproduce the experimental results well, in the visible regime below $\lambda_0 = 600$ nm, strong

deviations of the experimental data from the free-electron contribution are observed.

In this region energies are high enough to allow electrons to cross the internal bandgap, leading to interband absorptions in the metal. Analyzing the bandstructure of gold, absorption from the d-band to the Fermi surface around different lattice directions has been shown to cause the double-peak structure observed for ε'' above 2 eV [14]. These absorption peaks are also responsible for the distinct color of gold at visible frequencies. For practical applications such as numerical electromagnetic simulations, these features can be conveniently modeled with multiple Lorentzian resonances [15, 16]. For calculations presented in subsequent chapters of this thesis, the spline-interpolated $\varepsilon(\omega)$ data presented in Fig. 2.1 has been used. Compared to other experimentally recorded data [17], it is particularly interesting as it covers the near-infrared regime in detail, which will play a key role for the remainder of the work presented here.

2.1.2. Surface Plasmon Polaritons

In the following resonances of the free electron gas on metal-dielectric interfaces will be discussed. By analysis of poles of Fresnel reflection coefficients at such interfaces, these resonances will be identified as propagating surface bound hybrid electromagnetic waves. The dispersion relation of these so called surface plasmon polaritons will be discussed first for the most simple case of an interface of semi-infinite metal and dielectric half-spaces. It represents a good approximation for real metal films which are thick compared to the penetration depth of light in metal, e.g., $d_{\text{skin}} \approx 26$ nm for gold at 782 nm. However, for metal films with thicknesses on the order of this skin depth, as used throughout this thesis, the coupling between both interfaces has to be taken into account. It will be discussed in the second part of this section how such coupling can modify the properties of propagating surface plasmon polaritons.

Two Semi-Infinite Media

It has been shown how electromagnetic fields can lead to collective oscillations of the free electron gas. An oscillating electric dipole in the vicinity of a metal-dielectric interface similarly induces a displacement of the free electron gas, leading to a localized charge separation in the metal. As such separation induces itself a field, leading anew to charge separation, a coupled oscillation of the electromagnetic field and the electron gas can propagate as a longitudinally polarized wave. A sketch of the coupled system of

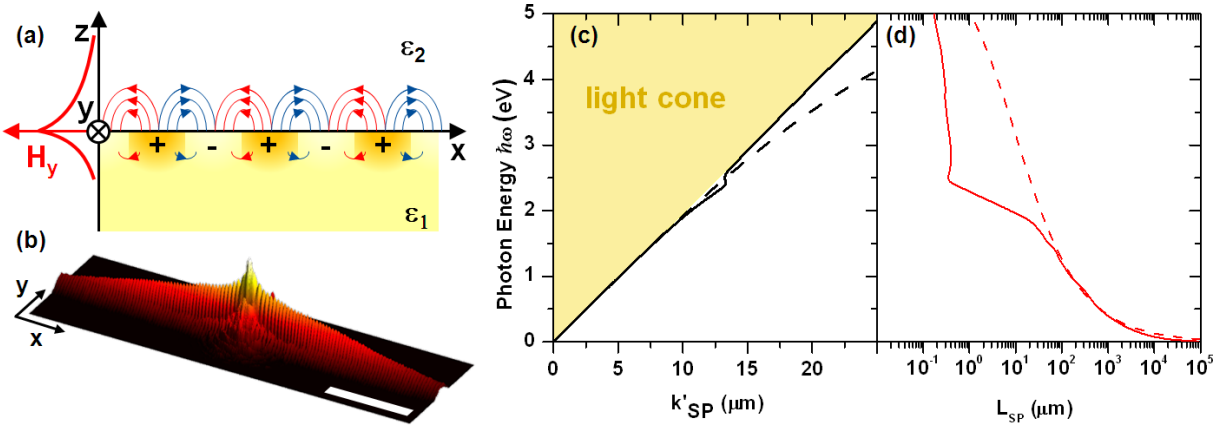

Figure 2.2.: Surface Plasmon Polariton: (a) Sketch of a propagating SP at the interface of a metal with the permittivity ε_1 and a dielectric ε_2. Charge oscillations in the metal are coupled to the electromagnetic field. The field is TM polarized and exponentially decaying normal to the interface. (b) 3D plot of logarithmic SP intensity, launched by a nanoslit and detected by leakage radiation microscopy. The exponential decay along the $\hat{\mathbf{x}}$-direction is clearly visible, the scale bar corresponds to 50 µm. For details of the SP excitation geometry see Fig. 2.6(c). - (c-d) Real part k'_{SP} of the wavevector and propagation length L_{SP} of a SP at a metal-air interface from Drude model (dashed) and experimental (solid line) values of ε_1. All modes lie outside the light cone in the dielectric half space (yellow). The propagation length in the visible is significantly reduced for experimental ε_1 data due to interband transitions.

electromagnetic field and electron gas is depicted in Fig. 2.2. The wave is called a surface plasmon polariton, with the term polariton expressing its hybrid nature. For convenience, we will refer to such a wave simply as surface plasmon (SP) for the remainder of this thesis.

In the following the properties of surface plasmons will be summarized. It is possible to solve the problem of a bound electromagnetic surface wave on the interface of dielectric and metal half-spaces by solving directly Maxwell's equations and the implied material boundary conditions [18]. However, we want here to resort to a different strategy: Analysis of the poles of the Fresnel coefficients on such an interface has been shown to similarly reveal the SP dispersion relation. This can be understood as, on the one hand, Fresnel-coefficients guarantee already all boundary conditions to be fulfilled, which enforces a constant in-plane component $k_{||}$ of the wavevector. On the other hand, a pole is naturally associated with a resonance at the metal interface. The strategy of analyzing poles of reflection coefficients will prove especially useful in the following section for studies of multilayer systems such as embedded thin metal films.

We are interested in the reflection of a plane wave in medium i with a permittivity ε_i

at the interface to a second medium j. The wavevector in each medium is described as $\mathbf{k}_i = (k_{ix}, k_{iy}, k_{iz})$ with $|\mathbf{k}_i| = k_i = \sqrt{\varepsilon_i} k_0$. Without loss of generality $k_{iy} = 0$ is chosen. For a wave whose electric field is parallel to the plane of incidence (termed TM (transverse magnetic) or p-polarized (*parallel*)) the reflection coefficient is

$$r_{ij}^{\mathrm{p}} = \frac{k_{iz}/\varepsilon_i - k_{jz}/\varepsilon_j}{k_{iz}/\varepsilon_i + k_{jz}/\varepsilon_j}. \tag{2.3}$$

For r_{12}^{p} poles are found as solutions to the equation $k_{1z}/\varepsilon_1 + k_{2z}/\varepsilon_2 = 0$. Squaring the terms yields the dispersion relation of SPs,

$$k_{\mathrm{SP}} := k_x = \pm k_0 \sqrt{\frac{\varepsilon_1 \varepsilon_2}{\varepsilon_1 + \varepsilon_2}}. \tag{2.4}$$

With the complex metal permittivity ε_1, the complex SP wavevector $k_{\mathrm{SP}} = k'_{\mathrm{SP}} + i k''_{\mathrm{SP}}$ corresponds to exponentially decaying waves, propagating in the positive and negative $\hat{\mathbf{x}}$ directions. The $1/e$ decay length of SP intensity thus can be expressed as $L_{\mathrm{SP}} = 1/2k''_{\mathrm{SP}}$, the so called SP propagation length. The exponentially decaying character of the SP is visualized by a three-dimensional plot of spatial SP intensity distribution in Fig. 2.2(b), the dispersions of k'_{SP} and L_{SP} on a gold-air interface is depicted in Fig. 2.2(c-d).

For polarization orthogonal to the plane of incidence (termed TE (transverse electric) or s-polarized (for German *senkrecht*)), the amplitude reflection coefficient is $r_{ij}^{\mathrm{s}} = (k_{iz} - k_{jz})/(k_{iz} + k_{jz})$, which does not contain any poles. Consequently surface plasmons with such a polarization do not exist, which can be understood as transverse polarization is not able to excite longitudinal oscillations of the electron gas (see Fig. 2.2(a)).

As resonances in the reflection coefficients are observed for TM polarized light, SP fields can be expressed as $\mathbf{E}_i = (E_{ix}, 0, E_{iz})$ of the character $E_{ix} = E_0 e^{i(k_x x + k_{iz} z)}$. For the field dependence in $\hat{\mathbf{z}}$, equation 2.4 implies $k_{\mathrm{iz}} = \pm k_0 \sqrt{\varepsilon_i^2/(\varepsilon_1 + \varepsilon_2)}$. Looking for surface bound waves which are decaying exponentially away form the surface, the signs have to be chosen as $k_{1\mathrm{z}} = +k_0 \sqrt{\varepsilon_1^2/(\varepsilon_1 + \varepsilon_2)}$ and $k_{2\mathrm{z}} = -k_0 \sqrt{\varepsilon_2^2/(\varepsilon_1 + \varepsilon_2)}$, defining the SP decay normal to the interface in the metal and the dielectric, respectively.

Thin Metal Films

So far our analysis has been limited to surface waves at the interface of a metal half-space. Experiments, however, will always be performed on metal films of finite thickness. In

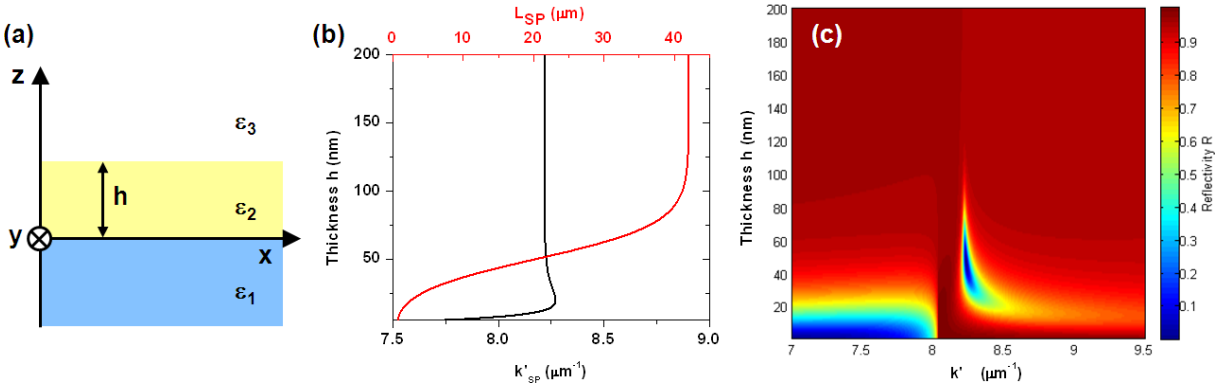

Figure 2.3.: Surface Plasmons on thin metal films: (a) Geometry considered here of a thin film of thickness h and complex permittivity ε_2 between two dielectric half spaces for which $\varepsilon_1 > \varepsilon_3$. - (b) Real part k'_{SP} of the wavevector (black) and propagation length L_{SP} (red) of an SP, propagating on the 23-interface and leaking into the substrate ε_1, as a function of the film thickness h. For the calculation a glass-gold-air structure at $\lambda_0 = 782$ nm has been considered. - (c) Reflectivity $R = |r^{\mathrm{p}}_{123}|^2$ as a function of the film thickness h.

this section the influence of such finite thickness on the complex SP wavevector and the associated SP properties will be examined. It will be found that SPs can tunnel though thin films, a property which is widely exploited for SP excitation as well as SP imaging, and which will play an important role for the presented work.

The geometry of interest is depicted in Fig. 2.3(a): a film with complex permittivity ε_2 of thickness h is sandwiched between two dielectric half-spaces with $\varepsilon_1 > \varepsilon_3$ (typically glass and air). To calculate $k_{\mathrm{SP}}(\omega)$, again poles of the amplitude reflection coefficient are identified [18]. For TM polarized light incident from medium 1, one finds

$$r^{\mathrm{p}}_{123} = \frac{r^{\mathrm{p}}_{12} + r^{\mathrm{p}}_{23} e^{2ik_{2z}h}}{1 + r^{\mathrm{p}}_{12} r^{\mathrm{p}}_{23} e^{2ik_{2z}h}}. \tag{2.5}$$

When calculating the poles $k_x = k_{\mathrm{SP}}$ of r^{p}_{123}, choices of the signs of the involved $k_{iz} = \pm\sqrt{\varepsilon_i k_0^2 - k_x^2}$ have to be made. While the dispersion relation is invariant under the choice of the sign of k_{2z}, the 4 possible permutations for k_{1z} and k_{3z} correspond to bound, growing or leaky solutions [19, 20].

We are particularly interested in solutions bound to the interface of media 2 and 3 (e.g. metal-air), which can leak into the dielectric substrate 1 (typically glass). To select such modes, $k_{1z} = -\sqrt{\varepsilon_1 k_0^2 - k_x^2}$, $k_{2z} = +\sqrt{\varepsilon_2 k_0^2 - k_x^2}$ and $k_{3z} = -\sqrt{\varepsilon_3 k_0^2 - k_x^2}$ have to be chosen, where the choice for the sign of k_{2z} is arbitrary as mentioned above.

Solving the implicit dispersion relation for SPs on the air side of a glass-gold-air structure

at $\lambda_0 = 782$ nm yields k'_{SP} and L_{SP} as shown in Fig. 2.3(b), together with the reflectivity $R = |r^{\mathrm{p}}_{123}|^2$ in Fig. 2.3(c). While the real part k'_{SP} of the wavevector, and thus the SP wavelength, only weakly varies with film thickness above ~ 30 nm, the propagation length L_{SP} is strongly reduced for films thinner than ~ 100 nm. This reduction compared to an infinitely thick film can be attributed to additional SP propagation loss due to tunneling of the SP field through the thin film. As $k'_{\mathrm{SP}} < \sqrt{\varepsilon_1}k_0$ for a glass-gold-air sandwich, the tunneled field can decouple to modes propagating in the glass. Such a process becomes particularly efficient for film thicknesses below the SP penetration depth into the metal. The extracted light, so called leakage radiation, can be used for SP imaging as will be discussed in detail in chapter 3 [21].

Besides the presented glass-gold-air layer system, which will be of particular importance for most experiments dealing with SP circuitry in this thesis, symmetric dielectric-metal-dielectric systems have also been extensively explored [22]. They can sustain so called long-range surface-plasmons which, to the cost of reduced surface confinement, can provide significantly enhanced propagation lengths (for a recent review see [23]). Another important geometry consists in glass-metal-water structures, which are the basis of most SP sensing systems. This type of structures will be covered in detail in section 2.3.

2.2. Surface Plasmon Optics

The field confinement of SPs in the normal direction, and the associated local field enhancement and high surface sensitivity, are the main ingredients driving SP based research. In this section different ways of controlling the in-plane flow of SPs will be addressed, which is important in the field of optical signal processing. Allowing sub-wavelength integration of circuits while still maintaining the large bandwidth of the optical frequency range, plasmonic devices appear to be suitable candidates for future integrated optical circuits.

However, propagating plasmons also possess great potential in combination with micro- and nanofluidics: as one of the earliest applications of plasmonics [24], sensing of local refractive index variations is widely used. Advancing from classic prism-based large-area sensing geometries, shaping of SP fields provides microscopic control of such sensing environments. Compact plasmonic circuits also allow integrated on-chip sensor designs. A detailed review of SP based refractive index sensing will be given in section 2.3.

Full control of plasmonic fields can be moreover applied for optical manipulation of

nanoscale particles. Approaches for pushing [25] and trapping [26] of nanoparticles with propagating SPs have already been reported. It will be presented in chapter 6 how plasmonic crystal structures can be utilized for routing metal nanoparticles.

For all such metal optical circuits, means to launch, shape, route and direct SP fields are required. In the first part of this section, several ways of how to couple to SP fields will be addressed. Special attention will be given to nanostructured SP sources, which offer a large control of SP beam shaping. In the second part, an overview of recent progress in the development of SP surface optical components for guiding, directing and modulating SPs will be given.

2.2.1. Excitation of Surface Plasmons

As SPs are exponentially decaying normal to the metal surface, the question raised is how to excite such bound modes. The problem can be understood by analyzing the SP dispersion relation, which is shown for a gold-air interface again in Fig. 2.4(a). The SP dispersion curve is located outside the light cone in air, i.e., $|\mathbf{k}'_{\mathrm{SP}}(\omega)| > k_0 = \omega/c_0$. Thus coupling to, but also decoupling of SP waves requires to overcome the mismatch between SP momentum $\mathbf{k}'_{\mathrm{SP}}$ and the in-plane projection $\mathbf{k}_{||} = (k_{x,\mathrm{in}}, k_{y,\mathrm{in}}, 0)$ of the momentum of incident light $\mathbf{k}_{\mathrm{in}} = k_0\hat{\mathbf{k}}_{\mathrm{in}}$.

Different strategies have been developed for SP launching, most of which can be understood as means of ensuring this momentum matching. First two important schemes relying on glass prims will be discussed. Subsequently a variety of nanostructures will be presented that permit coupling to and shaping of plasmonic beams. As part of this study, a Huygens-Fresnel model for SPs will moreover be discussed.

A variety of other techniques for excitation of propagating SPs has also been reported: phase-matching has been ensured, e.g., by evanescent waveguide coupling [27] or localized sources, such as near-field aperture probes [28], the latter allowing random placement of an SP dipole source. Moreover, nonlinear four-wave mixing has been applied recently for SP excitation by free-space light [29]. Also transverse mode-matching via end-fire coupling [30] has been implemented. Historically direct excitation of SPs by accelerated electron-beams [31] has played an important role. Promising strategies for plasmonic circuitry consist in integrated SP sources such as SP diodes [32] and lasers (see [33] for a recent review). However, as this work will not involve such methods, they will not be discussed further here.

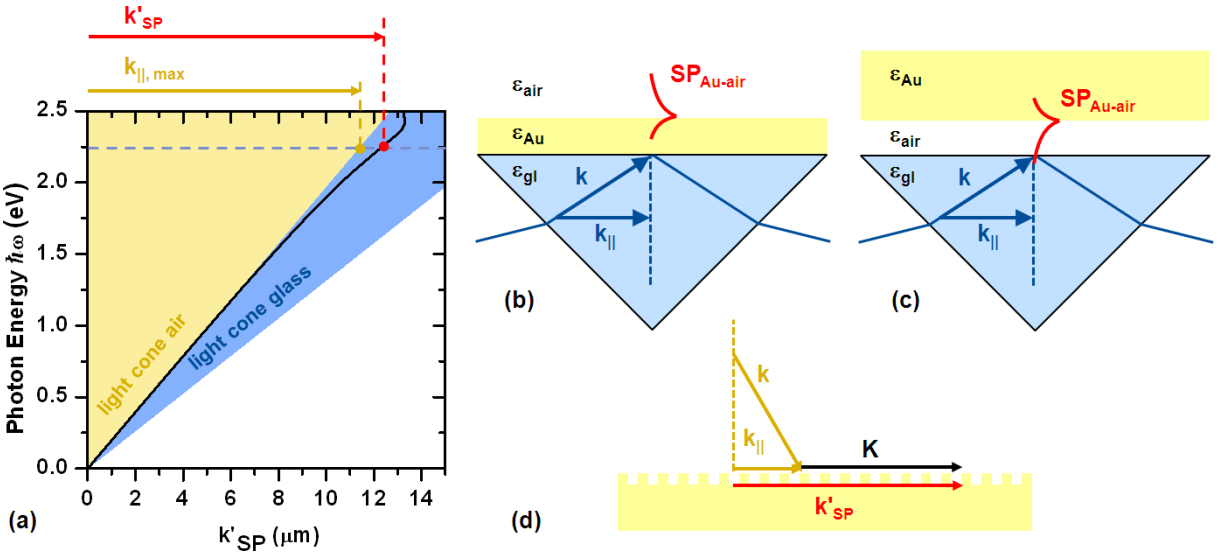

Figure 2.4.: Excitation of SPs: (a) SP dispersion relation for a gold-air interface from Fig. 2.2. SP modes at this interface lie outside the light cone in air, but inside the light cone in glass. - (b) Kretschmann-Raether configuration: Light is incident from a glass prism above the critical angle, i.e., under total internal reflection (TIR) conditions. The evanescent field can tunnel through the thin metal film, thus allowing phase-matched excitation of SPs on the opposing interface. - (c) Otto configuration: The evanescent field of light incident from a glass prism under TIR conditions can tunnel through a small air gap to permit SP excitation on thick gold films. - (d) Grating-coupling: Phase matching to SPs is achieved by illuminating a grating which provides an additional momentum through its grating vector **K**.

Prism Coupling

Prism coupling exploits the reduced wavelength of light in high index media for phase-matching SPs to propagating light. The modulus of the wavevector of light in a medium with refractive index n increases to nk_0, and the light cone is widened equivalently, overlapping the SP dispersion as depicted in Fig. 2.4(a).

To transfer the momentum from the glass prism to the metal-air interface, the two have to be brought close enough to permit light to couple. This has been achieved on the one hand by placing a thin metal film directly on glass, or by glass-immersion oil combinations (see Fig. 2.4(b)) [34]. For a sufficiently small thickness of the gold film, light incident under an appropriate angle can tunnel from the glass side through the metal film to the metal-air interface. As the SP wavevector lies outside the light cone in air, the angle for phase-matching to SPs is always larger than the critical angle of total internal reflection at a glass-air interface. This so called Kretschmann-configuration is still widely used for SP based refractive index sensing, which will be discussed in section 2.3.

On the other hand, the metal film can be brought in close proximity of a prism from the dielectric medium in the so called Otto-configuration [35] as shown in Fig. 2.4(c). This technique also allows exciting SPs on thick metal films. Interestingly, SPs excited by both methods can also decouple back to the high-index medium, and are hence leaky waves. This fact can be exploited for SP imaging as it will be discussed in chapter 3.

Nanostructure Coupling

A second approach to overcome the momentum mismatch between a plasmon and freely propagating light is the use of nanostructures. First a simple grating will be considered before focusing on more advances geometries.

By shining a plane wave on a one-dimensional grating with period P in the $\hat{\mathbf{x}}$ direction, an additional momentum is provided which corresponds to multiples of the grating vector $\mathbf{K} = 2\pi/P\hat{\mathbf{x}}$ (see Fig. 2.4(d)). The phase matching condition which has to be fulfilled for SP launching can therefore be expressed as $\mathbf{k}'_{\mathrm{SP}} = \mathbf{k}_{||} \pm m\mathbf{K}$ with an integer m denoting the diffraction order [36].

This phase matching argument is in fact very general, and more complex structures can also act as SP launchers. First the field resulting from a single dipole source will be considered. Omitting the z and time dependencies, the SP field at a point $\mathbf{r} = (x, y)$ launched by a horizontal dipole in the origin polarized along $\hat{\mathbf{x}}$ can be described as [37] $\mathbf{E}_{\mathrm{dip}} \propto \mathbf{e}x/|\mathbf{r}| \cdot H_1^{(1)}(k_{\mathrm{SP}}|\mathbf{r}|)$. Here $H_1^{(1)}$ is the Hankel function of the first kind, and the vector $\mathbf{e}$ ensures transverse fields in the two media according to $\nabla \cdot \mathbf{E}_{\mathrm{dip}} = 0$. Using the asymptotic form of the Hankel function for $|\mathbf{r}| > 1/k_{\mathrm{SP}}$, the expression reduces to a cylindrical wave:

$$\mathbf{E}_{\mathrm{dip}}(x, y) = \mathbf{e}E_0 \frac{x}{|\mathbf{r}|} \frac{e^{ik_{\mathrm{SP}}|\mathbf{r}|}}{\sqrt{k_{\mathrm{SP}}|\mathbf{r}|}} \tag{2.6}$$

A complex 2D nanostructure, described by a structure function $\mathcal{A}(x, y)$, can be decomposed into single dipoles scatterers, similar to classic Huygens-Fresnel modeling of diffraction [38, 39]. Every point of the source acts as a dipole source with a complex amplitude given by a space-dependent illumination field $E_{\mathrm{ill}}(x, y)$, stemming, e.g., from a focus laser spot. The

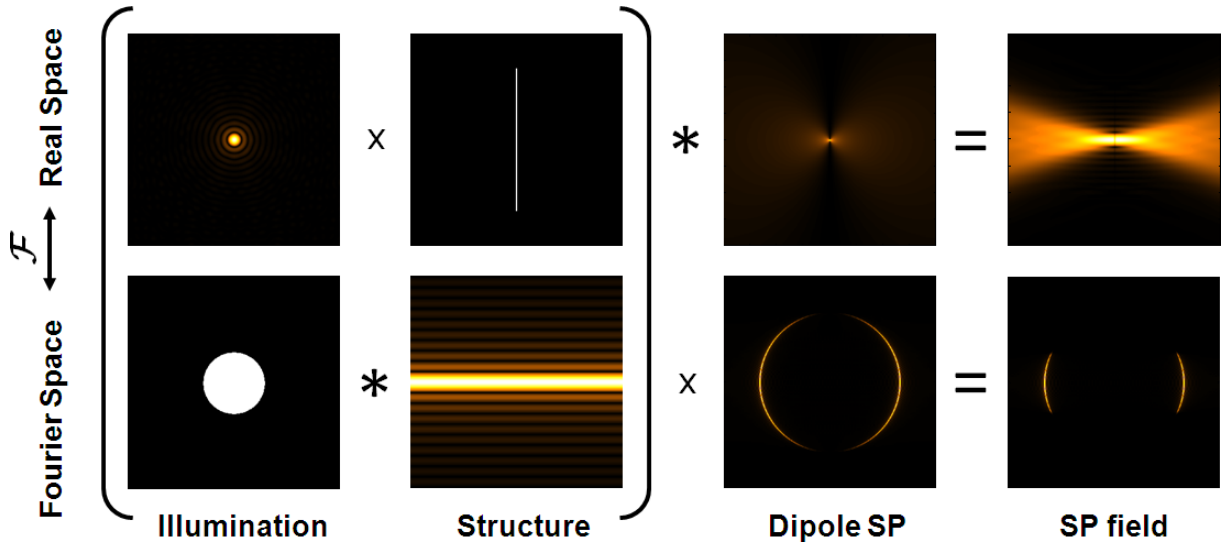

Figure 2.5.: Modeling of SP excitation: An SP field $\mathbf{E}_{\mathrm{SP}}(x,y)$ results from integration over displaced dipole sources, which are weighted by the product of a source structure function $\mathcal{A}(x,y)$ and the illumination field $E_{\mathrm{ill}}(x,y)$ (see equation 2.8). Alternatively, the field can be described in reciprocal space. According to equation 2.9, $\tilde{E}_{\mathrm{SP}}(k_x,k_y)$ results as a product of the Fourier space representation of an SP dipole field and the convolution of the Fourier transforms of the aperture function and the illumination field, $\tilde{E}_{\mathrm{ill}}(\mathbf{k}) * \tilde{\mathcal{A}}(\mathbf{k})$. The excitation process is modeled here for an Airy spot from an NA=0.45 objective illuminating a line structure at $\lambda_0 = 782$ nm.

full SP field can then be calculated as an integral over all point sources as:

$$\mathbf{E}_{\mathrm{SP}}(x,y) = \iint d\mathbf{r}'\mathbf{e}E_{\mathrm{ill}}(\mathbf{r}')\mathcal{A}(\mathbf{r}')\frac{x}{|\mathbf{r}-\mathbf{r}'|}\frac{e^{ik_{\mathrm{SP}}|\mathbf{r}-\mathbf{r}'|}}{\sqrt{k_{\mathrm{SP}}|\mathbf{r}-\mathbf{r}'|}} \tag{2.7}$$

$$= (\mathbf{e}E_{\mathrm{ill}}(\mathbf{r})\mathcal{A}(\mathbf{r})) * \left(\frac{x}{|\mathbf{r}|}\frac{e^{ik_{\mathrm{SP}}|\mathbf{r}|}}{\sqrt{k_{\mathrm{SP}}|\mathbf{r}|}}\right) \tag{2.8}$$

For most practical situations, the field component normal to the metal surface dominates, thus allowing reduction of the problem to a scalar one. Equation 2.8 is visualized for illumination of a line defect with a focused laser spot in the top part of Fig. 2.5. It can be directly applied for calculating SP propagation using numerical methods. Examples of such calculations will be discussed further down.

For the design and understanding of SP launching, it can be useful to transform the problem to reciprocal space. A simple 2D Fourier transform $\mathcal{F}$ of relation 2.8 yields

$$\tilde{E}_{\mathrm{SP}}(k_x,k_y) \propto \left(\tilde{E}_{\mathrm{ill}}(\mathbf{k}) * \tilde{\mathcal{A}}(\mathbf{k})\right)\frac{\cos\alpha}{k_{\mathrm{SP}}}\frac{|\mathbf{k}|}{|\mathbf{k}|^2-k_{\mathrm{SP}}^2}, \tag{2.9}$$

with $\mathbf{k} = (k_x, k_y)$ and the Fourier transformed functions $\tilde{E}_{\mathrm{SP}} = \mathcal{F}\{E_{\mathrm{SP}}\}$, $\tilde{E}_{\mathrm{ill}} = \mathcal{F}\{E_{\mathrm{ill}}\}$, $\tilde{\mathcal{A}} = \mathcal{F}\{\mathcal{A}\}$, and $\cos\alpha/k_{\mathrm{SP}} \cdot |\mathbf{k}|/(|\mathbf{k}|^2 - k_{\mathrm{SP}}^2) = \mathcal{F}\left\{x/|\mathbf{r}| \cdot H_1^{(1)}(k_{\mathrm{SP}}|\mathbf{r}|)\right\}$. Equation 2.9 is visualized in the bottom part of Fig. 2.5. Note that also the simple case of an infinitely sized grating, illuminated with a plane wave, which has been considered above, is covered by this model by choosing $E_{\mathrm{ill}}(\mathbf{k}) = \delta(\mathbf{k} - \mathbf{k}_{||})$ and $\mathcal{A}_{\mathrm{ill}}(\mathbf{k}) = \delta(\mathbf{k} - m\mathbf{K})$.

The model also accounts for more complex excitation geometries common in experimental situations: non-uniform illumination fields as, e.g., focused laser spots are described by E_{ill}, arbitrary launching structures as well as finite size effects of launching gratings are accounted for by $\mathcal{A}$. Understanding and control of these effects have been crucial for the experiments presented in this thesis. This is illustrated by a few representative examples, visualized by experimental and numerical results in Fig. 2.6:

(a) A 300 nm wide hole acts as a point-like scatterer and thus launches a dipole like SP pattern (Fig. 2.6(a)). The nanohole and other point-sources, such as fluorescent molecules or aperture probes, can also be understood to rely on phase-matching due to their broad spatial Fourier spectrum.

The presented images are acquired by leakage radiation (LR) microscopy, a technique which will be presented in chapter 3. LR microscopy allows real as well as reciprocal space imaging of SPs. However, if applied on SPs from nanoapertures in partly transparent films, real and reciprocal space images contain a coherent superposition of the illuminating field E_{ill}, diffracted light and the SP field. In the case of a single hole, these components correspond in reciprocal space to the central disk, the uniform background and the SP circle-like pattern, respectively, visible in the right column of Fig. 2.6(a). In the presented real-space images, the first two components could be partly suppressed by spatial filtering. A discussion of the different field components, as well as of spatial filtering techniques, will be given in chapter 3.

(b) An array of 11×11 such holes effectively acts as a 2D grating (Fig. 2.6(b)). The incident light field is polarized linearly in $\hat{\mathbf{x}}$, and launching of a narrow beam in this direction is observed. The grating launching can also be understood from Fourier space: the central circle, corresponding to the NA of the illumination objective, is replicated by multiples of the array grating vector. The overlap with the SP circle along $\hat{\mathbf{x}}$ causes the observed SP beam excitation. Finite size effects of the grating can be revealed in overexposed reciprocal space images (not shown here), containing the full diffraction pattern of the hole array, including 10 intermediate maxima between the discussed main resonances. Such effects have been exploited in the past for the

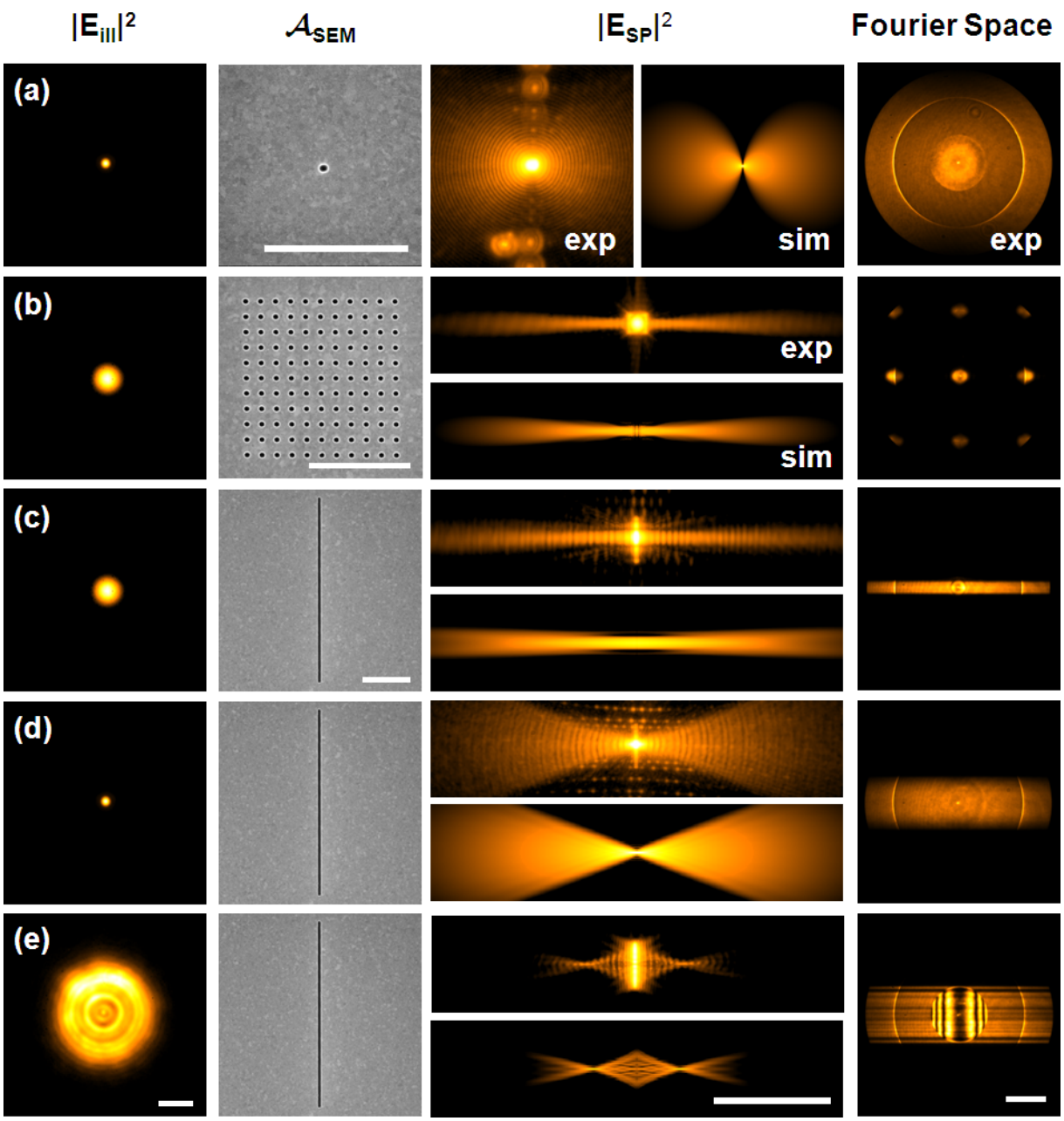

Figure 2.6.: Excitation of SPs by different nanostructures (a-c) and different illumination fields (c-e): SPs are launched by focusing a laser beam by (a) an NA=0.45 objective on a 300 nm wide nanohole, (b) an NA=0.13 objective on an array of 11×11 such holes with a period of 760 nm, and illumination of a 300 nm wide and 20 µm long nanoslit by focusing using a (c) NA=0.13 and (d) NA=0.45 objective, as well as (e) displacing the focus of the NA=0.45 objective $\delta z = 20$ µm into substrate. Experiments have been performed for SPs at $\lambda_0 = 782$ nm on 80 nm thick Au films, images have been acquired by LR microscopy. Simulated results stem from vectorial calculations according to equation 2.8. Scale bars correspond to 5 µm for excitation field and SEM images, 50 µm for experimental and simulated SPs and 5 μm^{-1} for reciprocal space micrographs.

design of optimized SP launching geometries [38].

(c) As a third nanostructure, a 300 nm wide slit is illuminated under the same conditions (Fig. 2.6(c)). The slit can be treated as an approximately one-dimensional scatterer [40, 41]. The diffraction pattern thus consists of a horizontal bar, overlapping with the SP circle, and a beam with a similar divergence as in the case of the hole array is launched.

The similarity in divergence can be understood from Fourier space: neglecting finite size effects, in both cases the width of the diffraction pattern along the reciprocal $\hat{k}_y$ direction is determined by the illumination objective as $\delta k_y = 2k_0\mathrm{NA}$. Because a section of the SP circle with the same width δk_y is excited, the divergence $\Theta = \arcsin(\delta k_y / 2k_{\mathrm{SP}})$ of the SP beam is directly related to the choice of the illumination NA.

(d) The effect of choosing an incident light field stemming from an objective with higher numerical aperture is demonstrated in Fig. 2.6(d): illuminating the same slit with NA=0.45 instead of the previously chosen NA=0.13 leads to a significant increase of beam divergence Θ.

(e) Finally, the focus of the incident light field gives an additional degree of freedom (Fig. 2.6(e)). Shifting the focus of the incident light $\delta z = 20$ µm into the substrate causes a phase shift of the incident field of $\tilde{E}_{\mathrm{ill}}^{\delta z}(k_x, k_y) = \tilde{E}_{\mathrm{ill}}^{z=0}(k_x, k_y) e^{i\sqrt{k_0^2 - k_x^2 - k_y^2}\delta z}$ [42]. The SP beam resulting from such phase shifted excitation along $\hat{\mathbf{z}}$ approximately converts the displacement of the focal plane to $\hat{\mathbf{x}}$, leading to an SP focal spot at $\delta x \approx 20$ µm away from the slit.

Various other nanostructure excitation geometries are possible, and have been reported in the literature. To name a few, dipole scatterers arranged to achieve single [43] and multiple [44] SP focal spots have been demonstrated. Moreover, nanostructures have been designed for SP Talbot carpet [45] and plasmonic Airy beam generation [46].

Also modulation of the incident light field has been considered as a powerful tool for controlling SP fields. Arbitrary wavefront modeling has therefore been implemented by the use of spatial light modulators, enabling control of the spatial properties of SPs launched by simple gratings [47–49]. Nanostructure coupling thus proved as a powerful tool for generation, shaping and, in combination with coherent modulation of the illuminating field, even active control of SP beams.

2.2.2. Controlling Surface Plasmon Propagation

In the previous section it was discussed how light can be coupled to surface plasmons. It has been shown that already a significant amount of SP propagation control can be achieved by careful choice of different nanostructures and illumination conditions.

In this section various methods for controlling already existing SP beams will be presented. Our study will focus on two-dimensional free SP beams, i.e., SP light fields which are confined normal to the interface, but which can propagate freely in the interface plane. Passive and active components for such beams will be discussed. The section will close on a brief overview of SP circuitry based on SP waveguides. Considering the amount of works published on this subject over the past decade, an overview as given here can only be far from complete. For more detailed reviews see, e.g., [50] and [51].

Refractive Components

Passive shaping of free surface plasmons has been implemented by refractive and diffractive surface optical components. Refractive components rely on the dependence of the SP wavevector $k_{\mathrm{SP}} = k_0\sqrt{\varepsilon_1\varepsilon_2/(\varepsilon_1+\varepsilon_2)}$ on the permittivity ε_2 of the dielectric half-space. At the boundary of, e.g., a metal-air and a metal-glass layer system, refraction of the SP wave can occur analogous to classic Snell refraction. Based on this effect, dielectric elements such as prisms and lenses have been developed [52, 53]. Similar homogenous elements, as well as gradient-index components have been designed as part of this thesis and will be discussed in detail in chapter 4. Recent progress in transformation optics has led to implementation of plasmonic transformation optical devices [54], also based on dielectric elements. Moreover, negative-refraction of SPs at the interface of metal-dielectric to metal-dielectric-metal sandwich layers has been reported [55].

A common drawback of most of these components is significant SP scattering loss to the light cone from the sharp element boundaries. Means developed on how to overcome this critical issue will also be addressed in chapter 4.

Diffractive Components

Diffraction and interference of surface plasmons has been studied in great detail. SP interference has been experimentally observed [28, 56], and exploited for the design of interferometric devices for SP beam steering [57, 58] and nanolithography [59]. As a

one-dimensional analogue to Fresnel zone plates, diffractive lenses have been designed [60]. A very powerful tool for SP beam control are plasmonic bandgap structures [61]. They rely on the same principles as classical photonic crystals, and will be discussed in detail in chapter 5. Applications range from simple SP Bragg mirrors [57, 62, 63] and defect waveguides [64] to more complex tasks such as wavelength multiplexing [65] and slow light SPs [66]. Parabolic Bragg mirrors have moreover led to the development of an in-plane plasmonic microscope [67].

SP demultiplexing has also been achieved by means of non-periodic gratings [68]. In addition, similar structures can be applied for the generation of plasmonic Airy beams by in-plane diffraction [69]. Moreoever, SP multiplexing has been implemented by multimode-interference couplers [70], in analogy to similar devices in dielectric slab waveguides.

All of the above mentioned structures also potentially suffer from scattering loss of SP intensity to free-space light. Strategies to suppress such scattering range from the straightforward fabrication of smooth gratings with tapered transitions to more evolved ones such as suppression of scattering to free space by grating resonance design. Such techniques have been applied for the results discussed in chapter 5.

Note, moreover, that in-plane diffraction of SPs relies essentially on the spatial Fourier spectrum of the scattering structures. This is similar to the situation discussed in the previous section, where the spatial Fourier spectrum of nanostructured SP sources, illuminated by external light fields, has been applied for SP beam shaping. A particular SP pattern can thus be achieved by the use of very similar nanostructures in both in-plane and out-of-plane illumination conditions, as, e.g., demonstrated for the case of plasmonic Airy beams in [46] and [69].

Active Components

Besides the presented passive components, much attention has been given recently to the development of active plasmonic devices. One of the primary tasks is the modulation of SP intensities. While all-optical [71] and electro-optical solutions involving plasmonic components have been applied for switching of propagating light [72, 73], switching of mere plasmonic signals has only been achieved using all-optical methods. Modulation strategies rely on modulating the absorption of SPs in the metal [74] and the dielectric, the latter using cadmium selenide [75] quantum dots and photochromic molecules [76]. Such all-optical methods provide extremely fast modulation times at the femtosecond range.

However, implementing electro-optical methods which allow simple coupling of plasmonic to electronic circuits still remains a challenge.

One of the major limitation of plasmonic systems is the limited propagation length of surface plasmons. Similar to what is state of the art for long-distance fiber connections, repetitive amplification of a plasmonic system on the chip level would be necessary to achieve considerable signal propagation distances. Amplification of free SP waves outside waveguides has therefore been implemented by different methods, including optical pumping of dye solutions [77], as well as rhodamine 6G [78] and lead sulfite [79] doped poly(methyl methacrylate) (PMMA) layers. For a broader review on recent progress on active plasmonic devices, including active plasmonics in SP waveguides, the reader is referred to [33, 80, 81].

Surface Plasmon Waveguides

So far structures for free SP beam manipulation have been presented. However, great potential for SP flow control in integrated plasmonic circuits also lies in the application of SP waveguides, confining the SP field in two dimensions.

Various strategies for SP waveguiding exist. One of these has already been mentioned above, namely defect waveguides in plasmonic bandgap structures. In addition, and similar to dielectric waveguides, high-index dielectric strips on metal substrates, so called dielectric loaded SP waveguides, have also been developed [82]. They provide sub-wavelength field confinement, but possess relatively short propagation lengths of around $\sim$ 50 µm at $\lambda_0 = 1.5$ µm. Moreover, metal strip waveguides have been designed, residing in asymmetric dielectric environments (typically in an air environment on a glass substrate) [83]. Placing such waveguides into a symmetric environment, long-range SP modes can be exploited, and significantly enhanced propagation lengths have been achieved up to the centimeter range [23, 84, 85]. However, such increase is based on spreading of the SP field into the dielectric over several wavelengths, and thus yields reduced field confinement. A combination of long-range SP waveguides with dielectric loaded waveguides has been reported recently [86], showing propagation lengths of hundreds of micrometers in the near-infrared, while maintaining reasonable mode widths. Another structure providing a good compromise between mode confinement and propagation length consists of waveguides based on, usually V-shaped, metal grooves [87, 88]. They allow concentration of the light field inside the groove, hence filling the dielectric space in the most efficient way.

For a selection of these waveguide geometries, various passive and, more recently, also some active devices have been implemented, such as bends, Y-splitters, couplers, ring-resonators, add-drop multiplexers, switches, Mach-Zehnder interferometric modulators and SP waveguide amplifiers. For a review of the latter, as well as of other SP waveguiding techniques such as metal slot waveguides, wedge waveguides or metal nanowires, the reader is referred to the comprehensive study in [51].

Prospects for Plasmonic Circuitry

Due to their high integrability, SP waveguides appear as promising candidates for SP circuitry. However, limited propagation length due to losses in the metal, and also the associated heating and energy consumption remain crucial issues compared to integrated dielectric optical components. Also recent approaches to include gain media would still suffer from increased energy consumption. Plasmonic components are thus particularly interesting for operating special tasks in optical data processing that require high integration density of optical elements, but do not rely on large propagation distances. In combination with classic integrated dielectric optics, they could pave the way towards efficient hybrid integrated optical circuits.

Two-dimensional surface optics of free SP beams is anticipated to help in solving particular tasks in such SP based data processing, as, e.g., mode matching between waveguides or multimode interference coupling. A role similar to that of classic optical components in fiber and integrated optical networks is expected.

Several approaches towards novel two-dimensional optical components will be discussed in the first part of this thesis. Full control over SP fields moreover bears great potential for a variety of other applications beyond SP circuitry. An example of such applications, consisting in controlling the movement of metal nanoparticles by means of SPs in metal gratings, will be addressed in chapter 6.

2.3. Refractive Index Sensing with Surface Plasmons

In chapters 7 and 8 of this thesis two techniques will be presented for high-resolution refractive index sensing based on propagating surface plasmons. Therefore in this section a brief introduction to the field of SP based sensing will be given. Different sensing geometries as well as optical configurations will be reviewed, and performance parameters

such as sensing sensitivity and figures of merit will be introduced.

SP based sensing is historically one of the first major applications of plasmonics [24], and up to date one of the few commercially successful ones [89]. SPs are particularly suitable for sensing purposes again due to their surface bound nature. The angle and frequency, or analogously wavevector and wavelength, at which an SP resonance occurs, are strongly dependent on the permittivity of the dielectric half-space (see equation 2.4). Thus precise measurement of the prior quantities can be used for detecting small changes of the refractive index of the dielectric.

While such changes can be quantified with high precision also by other techniques such as classic refractometers [90, 91], SP sensors are exclusively sensitive to changes within a few decay lengths of the electric field, i.e., typically within a few hundreds of nanometers. This surface sensitivity can be exploited for monitoring binding events to functionalized surfaces, hence making SP sensing a very popular tool for label-free biosensing and chemical analysis [92]. From that point of view also the first experimental observation of SPs stemming from slow oxidation of silver layers over time can be seen as a first application of SPs as means for sensing the growth of thin films [31].

Historically, mostly propagating SPs have been used for refractive index sensing, but more recently, also isolated nanostructures have been incorporated into sensing devices [93]. Metal structures such as nanoparticles or holes sustain so called localized surface plasmon resonances (LSPR). Among others, sensors based on single triangular nanoparticles [94], on nanospheres [95], nanoshells [96] and nanoholes [97] have been implemented. Due to high field concentration in the metal, such structures possess generally much broader resonances, leading to a decrease in the bulk sensing performance. They also demand more sophisticated fabrication methods. However, benefiting from small mode volumes and local field enhancement, they are promising candidates for analysis at low concentrations, and possibly single-molecule detection. Moreover, they allow using optically simple spectroscopy setups. They thus provide a complementary technology to sensors based on propagating SPs. A thorough comparison of both technologies is given in [98].

As the methods presented in chapters 7 and 8 rely solely on propagating SPs, the following analysis of SP sensing properties will be restricted to devices based on such modes.

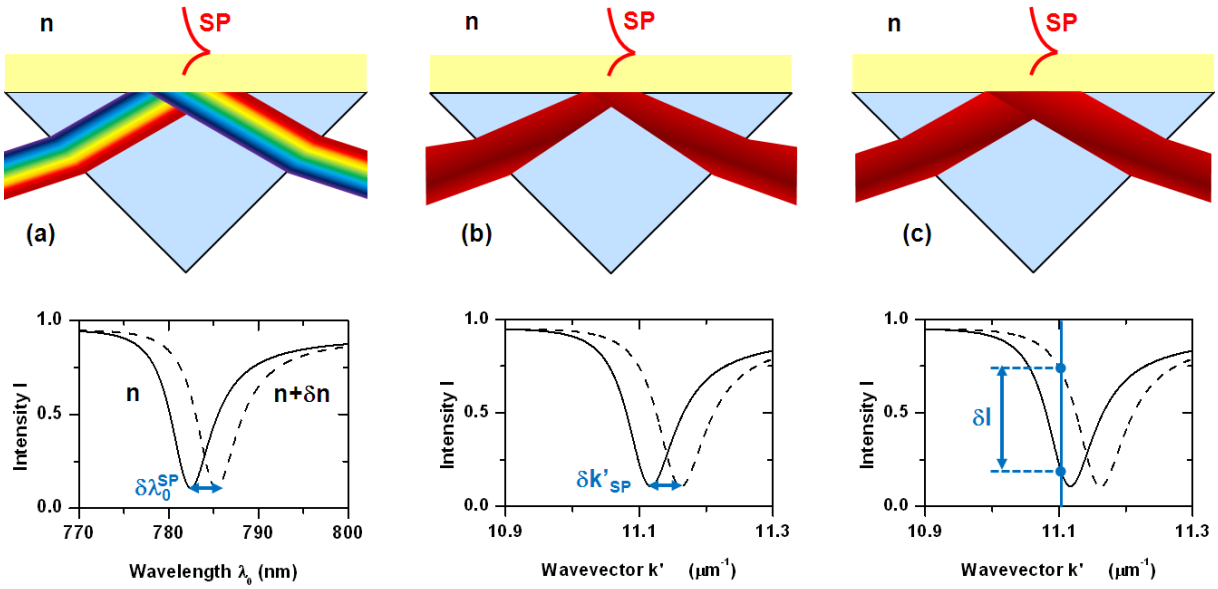

Figure 2.7.: Sensing interrogation schemes of SP sensors: (a) Wavelength interrogation: SPs are excited by a collimated, polychomatic light sources. A variation δn of the refractive index causes a shift $\delta\lambda_0^{\mathrm{SP}}$ of the resonance peak wavelength. - (b) Angle or wavevector interrogation: using a focused, monochromatic light source, shifts $\delta k'_{\mathrm{SP}}$ of the resonance wavevector are detected. - (c) Intensity or amplitude interrogation: using a collimated and monochromatic light source, one point of the SP resonance curve is probed. A change δn yields a shift of the resonance and thus a change of the reflected intensity δI.

2.3.1. Optical Instrumentation

A change δn in the refractive index $n = \sqrt{\varepsilon_2}$ influences the dispersion relation of SPs, $k_{\mathrm{SP}} = (2\pi/\lambda_0)\sqrt{\varepsilon_1\varepsilon_2/(\varepsilon_1+\varepsilon_2)}$, with ε_1 and ε_2 denoting the permittivities of metal and dielectric, respectively. Thus refractive index modulation can be detected by either tracking the resonance *wavelength* λ_0^{SP} at a fixed wavevector [99], or alternatively monitoring the resonance *wavevector* k'_{SP} using monochromatic light with fixed λ_0 [100]. In typical ATR setups, k'_{SP} is determined by the reflection angle under which the SP resonance occurs. Both of these interrogation schemes are schematically visualized in Fig. 2.7(a-b).

It is moreover possible to fix both wavelength and angle, and only track *intensity* changes at such a fixed position in parameter space, as visualized in Fig. 2.7(c). Shifts of the resonance curve induced by changes δn of the refractive index will then yield a change δI of the reflected intensity [101]. Also modulation of other quantities such as phase [102] or polarization [103] have been implemented, yielding similar performances as amplitude modulation based sensing [104].

Various optical configurations for SP sensing have been explored in the past. Devices based

on prism coupling [101], grating coupling [105], and waveguide coupling from fibers [106] or integrated dielectric waveguides [107] have been reported. Prism coupling for sensing is a technologically rather simple technique that requires a minimum amount of nanofabrication. Moreover, large sample areas can be handled easily, and it provides a well controlled environment for the integration of novel approaches for sensing performance optimization. Grating coupling, and especially the use of integrated waveguides and fibers, is technically more demanding, but allows miniaturization and monolithic integration of SP sensing devices. A few key developments will be highlighted in the following, but for a more comprehensive treatment we refer to the overview given in [92].

Different interrogation schemes have been applied for the mentioned excitation geometries. Especially for angle or wavevector interrogation, several strategies for improving refractive index resolutions have been investigated. One of such strategies are self-referenced measurements: detecting the difference signal between reflection from a sensing and a reference cell yields greatly reduced sensor noise levels [108]. Another approach consists in sensing with long-range surface plasmon polaritons in thin metal films in symmetric dielectric environments [109]. The long propagation lengths of such modes correspond to sharp resonance peaks, leading to increased figures of merit as explained in section 2.3.2. However, as discussed for SP waveguides, such long propagation lengths stem from large extension of the SP field into the dielectric. The associated increase in mode volume enables the mentioned large bulk refractive index resolutions, but the sensitivity to surface binding events is massively reduced.

Another target of complex SP instrumentation consists in increasing sensing throughput, commonly achieved by parallel read-out of multiple sensing cells. Due to the low spatial resolution of wavelength and angle interrogation setups, parallelization proved limited to only a few sensing channels [110]. To overcome these limitations, amplitude measurements have been applied for parallelization in SP imaging setups [111]. Such configurations enforce fixed wavelength and wavevector by illumination of the sample with collimated monochromatic light. Imaging the reflected light in a prism setup as depicted in Fig. 2.7(c) allows sensing with good spatial resolution, the latter being the key ingredient for large scale parallelization. Setups with arrays of 100 and more parallel sensing cells have been reported [112, 113].

Sensing with high spatial resolution can also be accomplished by back illuminating an immersion microscope objective [114]. The light is focused on a thin metal film, and SP resonance dips are detected in reciprocal space images of the reflected light. The setup thus corresponds to a classic ATR geometry, extended to two-dimensional variation of

the in-plane wavevector $\mathbf{k}_{||}$. It provides high spatial resolution, which can be exploited to address multiple sensing cells by two-dimensional scanning of the metal surface [115].

Besides the optical instrumentation, also the hardware involved in data acquisition, such as light sources, detectors and electronic data processing equipment, as well as the subsequent data processing algorithms, such as spatial and temporal averaging and methods of peak center determination, can have a tremendous impact on the sensor performance. The influence of some of these parameters on the noise properties of the instrument developed during this thesis will be discussed in chapter 7.

2.3.2. Performance Parameters

In this section, it will be addressed how to quantify the performance of different sensing geometries, especially the limit of minimum detectable index shifts. Sensor sensitivity and resolution will be introduced, and different definitions of figures of merit will be discussed. Sensing resolution is also the key feature for which strategies of improvement will be presented as part of this thesis. Depending on the application, other performance parameters such as linearity, reproducibility or dynamic range may also be of importance. However, they will not be treated in more detail here.

A sensor is based on measuring the change of an output quantity Y which is induced by an input quantity of interest, in our case the refractive index of the dielectric half-space n. The sensitivity of a refractive index sensor can then be defined as the slope of the sensor calibration curve:

$$S_Y = \frac{\partial Y}{\partial n} \tag{2.10}$$

In case of wavelength interrogation, the sensitivity is therefore defined as $S_\lambda = \partial\lambda_0^{\mathrm{SP}}/\partial n$, for wavevector interrogation as $S_k = \partial k'_{\mathrm{SP}}/\partial n$ and for amplitude interrogation as $S_I = \partial I/\partial n$.

The resolution of a sensor in terms of n is defined as the smallest detectable change σ_n of the measured quantity. Expressing this resolution in terms of the output quantity Y, which is detected with an uncertainty σ_Y, the limit of detection can be expressed as

$$\sigma_n = \frac{\sigma_Y}{S_Y}. \tag{2.11}$$

Thus the resolution of a sensor is always dependent on the noise properties of Y. For SP based sensing, such noise also includes technical components such as detector and light source properties. The definition of a figure of merit of a sensing technique should exclude

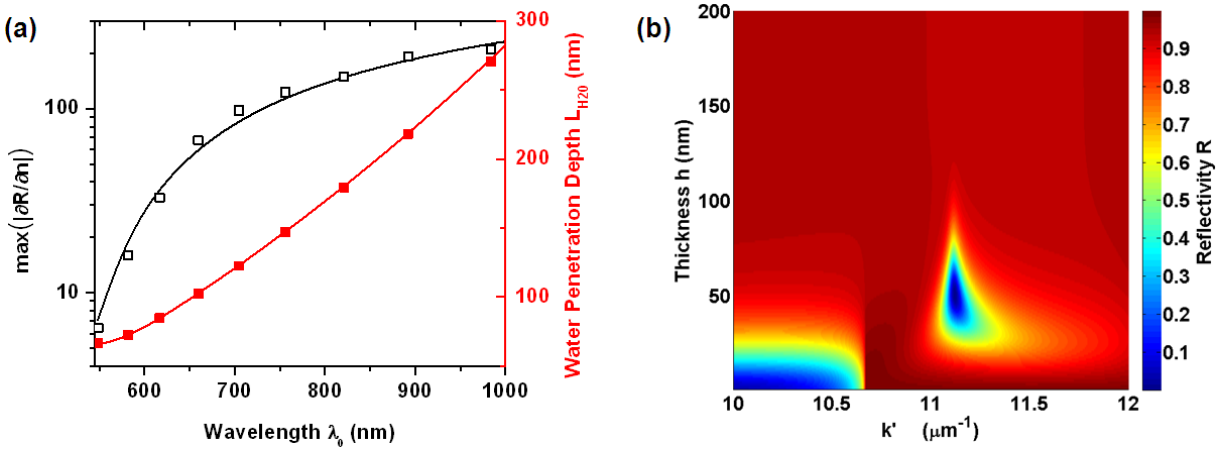

Figure 2.8.: SP sensing sensitivity: (a) Absolute sensing figure of merit $|S_I| = |\partial I/\partial n| = |\partial R/\partial n|$ and SP penetration depth $L_{\mathrm{H_2O}} = |1/2\mathrm{Im}(k_{3z})|$ in water as a function of operating wavelength λ_0. Sensitivities have been calculated numerically from Fresnel coefficients as discussed in section 2.1.2, using gold permittivity from Johnson and Christy (squares) and from Drude-Lorentz modelling according to [16] (solid lines). Water and glass have been assumed to be dispersion-free with refractive indices of $n_1 = 1.51$ and $n_3 = 1.33$, respectively, the thickness h and the operating wavevector have been chosen for each wavelength to yield maximum absolute sensitivity. - (b) Reflectivity $R = |r^{\mathrm{p}}_{123}|^2$ as a function of incident angle and film thickness, calculated from Fresnel coefficients for $\lambda_0 = 782$ nm.

such mere technical contributions, and allow a general comparison of the performance of different sensor techniques. Note that for SP based chemo- and biosensing similar definitions of sensitivity and resolution hold, phrased in terms of, e.g., molecular concentrations.

For amplitude interrogation, $\sigma_n = \sigma_I/S_I$ holds. Treating intensity noise σ_I as a merely technical contribution, the figure of merit for such sensors hence consists of the sensitivity only, $\mathrm{FOM}_I = S_I$.

For wavelength and wavevector interrogation, one finds $\sigma_n = \sigma_\lambda/S_\lambda$ and $\sigma_n = \sigma_k/S_k$, respectively. However, accuracy in determination of the peak centers λ_0^{SP} and k'_{SP} is commonly assumed to be proportional to the widths w_λ and w_k of the resonances, leading to the often used figures of merit S_λ/w_λ and S_k/w_k, respectively. As pointed out by Homola [92], however, such an assumption is only correct in few special cases. For a variety of realistic situations wider peaks can also cause reduced intensity noise levels due to larger samples sizes for spatial averaging. Thus accuracies for the peak centers may scale with the square roots of the widths, and figures of merit of $S_\lambda/\sqrt{w_\lambda}$ and $S_k/\sqrt{w_k}$ can be more applicable.

Having defined figures of merit, the question remains at which operating wavelength sensing

experiments should be carried out to achieve best performance. Calculated sensitivities, and thus figures of merit, for amplitude interrogation of SPs on a gold-water interface at wavelengths between 550 nm and 1000 nm are depicted in Fig. 2.8(a). A constant increase of the bulk sensitivity with wavelength is observed. At the same time, however, the SP penetration depth $L_{\mathrm{H20}} = |1/2\mathrm{Im}(k_{3z})|$ into the water is also increased, causing the sensitivity to binding events at the surface to drop. For the experiments presented in this thesis an intermediate wavelength regime in the near-infrared ($\lambda_0 = 782$ nm) has hence been chosen.

The variety of discussed optical setups and interrogation schemes raises the question of fundamental limits of SP based sensing resolution. A comparative study of different optical designs, interrogation schemes and operating wavelengths has been presented recently [116]. Assuming state-of-the-art source and detection equipment, it has been found that most techniques suffer from similar restrictions, yielding SP sensing resolution to approach its theoretical limits. It is these limits which we try to push a bit further by the approaches presented in chapters 7 and 8 of this thesis.

3 Leakage Radiation Microscopy

The surface bound nature of SPs requires advanced strategies to allow coupling of SPs to freely propagating light. Besides the already discussed excitation geometries, also techniques for SP imaging have been developed. Some of these will be introduced in this chapter.

Among these, leakage radiation (LR) microscopy is very convenient for imaging propagating SP waves. It is the central technique used to characterize the two-dimensional optical elements presented in the second part of this thesis, and in its third part LR microscopy will be introduced as a novel tool for nanostructure based SP sensing.

The properties of LR microscopy will be discussed in this chapter, and the optical setup used throughout this thesis will be described in detail. The chapter will close on an overview of some specific strategies implemented in the setup for improving SP imaging capacity.

3.1. Surface Plasmon Imaging

Imaging of surface plasmons can in principle be achieved by methods very similar to those used for SP excitation. Before concentrating on LR microscopy, two alternative strategies, fluorescence imaging and scanning near-field microscopy, will be discussed in the following. A short overview of other imaging techniques will be given at the end of the section.

3.1.1. Fluorescence Imaging

One approach for converting SPs to propagating light is the use of fluorescent probes. These can be excited by the SP wave, and emit light to the far field, with intensities proportional to the SP excitation intensity. The process is sketched in Fig. 3.1(a).

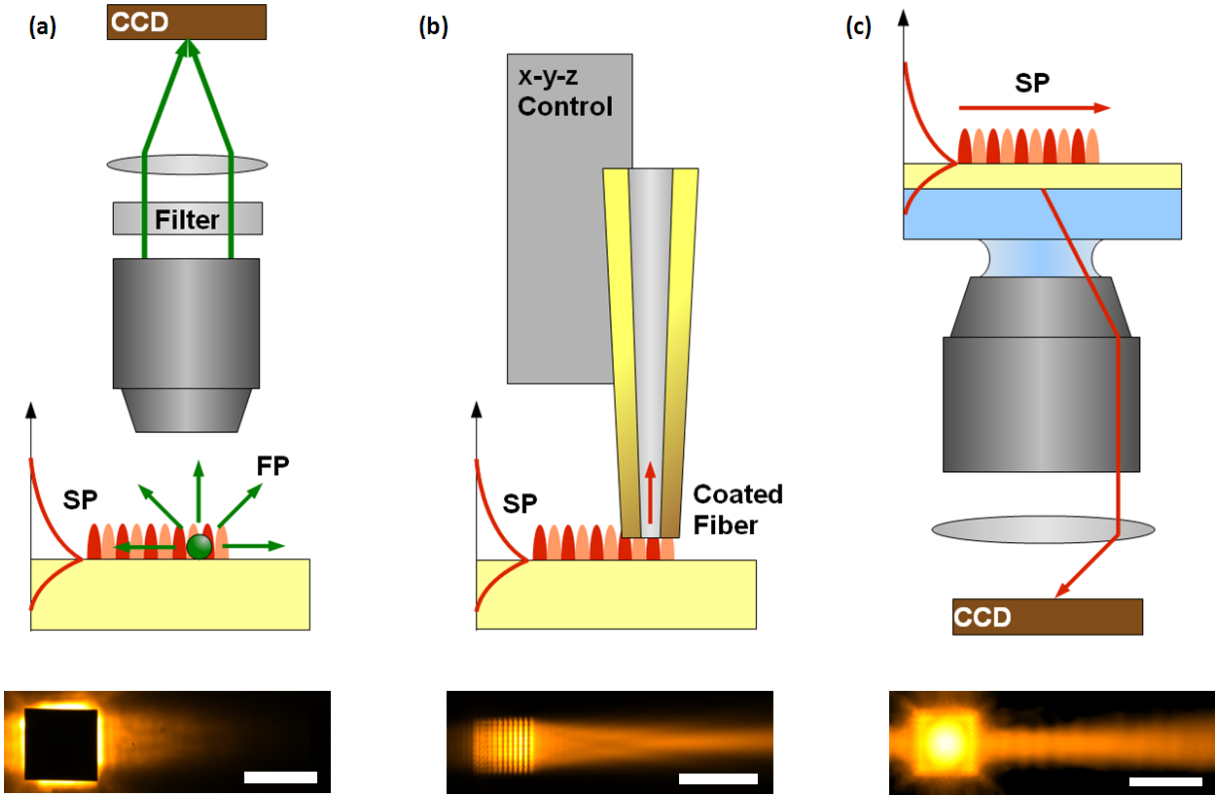

Figure 3.1.: SP imaging techniques: (a) Fluorescence Imaging - (b) Scanning Near-Field Optical Microscopy - (c) Leakage Radiation Microscopy - SPs on sample images were launched by arrays of 11×11 holes with a period of 750 nm for fluorescence microscopy and 760 nm for SNOM as well as LR microscopy at $\lambda_0 = 785,\ 800$ and 782 nm, respectively. Scale bars correspond to 10 µm. The SNOM image is reproduced from [38] (© The Optical Society).

Fluorescence imaging of SPs has first been demonstrated in 2002 [40]. SP have been monitored using Rhodamine 6G molecules. To prevent non-radiative decay of molecules close to the metal surface by quenching, a thin dielectric spacer layer between the probes and the metal surface has been introduced by the authors.

As a first project for this thesis, a fluorescence imaging setup was developed based on 1% lead sulfide quantum dots (Evident Technologies PbS Core EviDots 1100) in a 60 nm thick Poly(methyl methacrylate) (PMMA) matrix. SPs were excited by hole array sources engraved in a 150 nm thick gold film. The arrays were illuminated at $\lambda_0 = 785$ nm from the glass side with linearly polarized light along the horizontal axis. Quantum dots were excited by the plasmon field, resulting in emission around 1100 nm. Excitation light was subsequently filtered out using a longpass dielectric filter transmitting above 805 nm (Semrock 785 nm EdgeBasic) and crossed linear polarizers. The weak fluorescence signal

was imaged on a Peltier cooled back-illuminated charge-coupled device camera (Princeton Instruments PIXIS 1024x1024 EEV). To allow longer exposure times while preventing overexposure at the level of the source array, the area of direct transmission was filtered out spatially by a home-made opaque square silver mask, fabricated by an electron beam lithography lift-off process. A sample image is depicted in Fig. 3.1(a).

Special care had to be taken to choose the thickness of the polymer layer below cutoff of the lowest guided TE_0 mode (here ~ 140 nm) to allow only TM_0 modes, i.e., surface plasmons to propagate [117]. Otherwise, higher order modes guided in the PMMA layer could dominate the acquired fluorescence signal.

Being based on relatively simple optical microscopy, fluorescence imaging has thus proven to be a convenient far-field method for SP imaging. However, it suffers from weak fluorescence intensities necessitating relatively long exposure times for acceptable signal-to-noise ratios. In addition, absorption of SPs by the probes represents an additional loss channel, causing SP propagation lengths to decrease. The conversion to fluorescent light may furthermore cause loss of coherence and polarization properties of the observed plasmonic field. Therefore only direct space intensity mapping of SPs is rendered possible. Fluorescent probes may also suffer from bleaching, and the system provides at best diffraction limited resolution at the (usually red-shifted) emission wavelength of the probes.

3.1.2. Scanning Near-Field Optical Microscopy

Similar to fluorescence imaging, scanning near-field optical microscopy (SNOM) of surface plasmons is based on bringing a local light probe into the plasmonic near-field. However, differing from the two-dimensional distribution of multiple fluorescent probes seen above, a single near-field probe is used for SNOM, which can be positioned in all three spatial directions in a controlled manner. Typically aperture probes, such as metal coated fiber tips [118, 119], or aperture-less scatterers, such as sharp metal tips or nanoparticles [120, 121], are chosen. Also active tip techniques have been developed [122]. The positioning normal to the surface is achieved by feedback loop height control, often by attaching the probe to a piezoelectric tuning fork, but also to an AFM tip or by using the collected light itself as height control variable. A sketch of aperture SNOM is depicted in Fig. 3.1(b).

SNOM was developed in 1984 [118, 123], and has later been applied for imaging of localized and propagating SP fields [124–126]. It provides high resolution imaging of SP fields

below the diffraction limit, also on thick metal films. Implementation of heterodyne detection and Mach-Zehnder interferometers have furthermore enhanced the capabilities to time-resolved [127, 128] and phase measurements [129]. In addition, imaging of magnetic field components at optical frequencies has been reported by nanostructuring the metal coating of the aperture [130, 131].

As a scanning technique, however, SNOM suffers from slow image acquisition, and associated artifacts such as image drifts. The required optical setups are moreover rather complex, and require advanced electronic signal processing. Besides, with the tip entering the near-field, SNOM is a perturbative technique which may modify the local SP dispersion. Considering these drawbacks on the one hand, but its versatility on the other, SNOM is the method of choice for applications where simpler detection approaches fail, such as imaging of near-field of localized plasmon resonances, e.g., in metal nanoparticles or optical antennas [132, 133].

3.1.3. Other Techniques

A variety of other techniques has been used for SP imaging. Propagative plasmons have been visualized by detection of SP far-field scattering from random scatterers [134] or nanostructures such as gratings [36], both in analogy to the equivalent coupling processes discussed earlier. This method has been chosen in chapter 4 for evaluating the reduction of scattered SP intensity in devices featuring transition gradients to refractive surface optical components.

Also far-field methods such as standard dark-field microscopy and confocal microscopy have been applied, mostly for spectroscopy of localized surface plasmon resonances [135, 136]. Dark-field microscopy will be used in chapter 6 for the detection of propelled metal nanoparticles.

Different methods such as photochemical mapping also exist. Moreover, imaging based on localized excitation of SPs by accelerated electron beams has been implemented in multiple ways. They have found application particularly for imaging localized surface plasmon resonances. For a detailed review of these and other techniques, see [137].

3.2. Leakage Radiation Microscopy

The method of choice for most experiments carried out as part of this thesis has been leakage radiation microscopy. It is schematically visualized in Fig 3.1(c). The technique gives access to SPs on the air-metal interface of a thin gold film on top of a high-index dielectric substrate. As discussed in section 2.2.1, momentum matching of propagating light to SPs can be achieved under a specific angle inside the substrate. At the same time SPs propagating on such layer systems do continuously decouple to propagating modes in the glass. This so called leakage radiation (LR) can be collected by standard immersion microscopy. Note that a sufficiently large numerical aperture of the collection objective is required to fulfill NA $> k'_{\mathrm{SP}}/k_0$. This requirement becomes harder to fulfill when aiming at imaging SPs propagating in higher dielectric media such as water.

SPs have been imaged by LR microscopy using immersion objectives for the first time in 1996 [28]. Earlier experiments had been carried out which collected leakage radiation by hemispherical prisms for reciprocal space imaging, but did not utilize the signal for real space imaging of SPs [138]. Since then LR microscopy has been applied for a large variety of experiments due to its optical simplicity, as well as its speed and ease of use. Among others, imaging of freely propagating plasmons [28], SPs in plasmonic bandgap structures [139], in dielectric optical elements [1] and in plasmonic waveguides [140] has been reported.

In contrast to SNOM, the most powerful SP imaging technique so far, LR microscopy does not directly collect the plasmonic near-field. It thus also lacks the possibility of vectorial SP characterization, phase-mapping and imaging of localized SPs. However, it does provide access to complex field information in a fast and optically simple far-field configuration. Most important, as shown in the following, access to the reciprocal space can be conveniently achieved by optical Fourier transform, which allows simple identification and separation of plasmonic and diffracted light fields. In addition, the full toolbox of optical microscopy is at hand, rendering polarization characterization of the fields and spatial filtering in real and Fourier spaces possible.

3.2.1. Properties

In the following, some key properties of LR microscopy will be discussed. First reciprocal space imaging and the scaling of reciprocal images will be addressed. Subsequently, the different fields contributing to LR images will be identified, and resulting interference

artifacts will be presented. It will furthermore be discussed which vectorial field component is actually mimicked by LR microscopy. Finally, optimal metal film thicknesses will be analyzed as a trade-off between SP propagation length and LR signal strength.

Reciprocal Space Imaging

A great advantage of LR microscopy is that leakage radiation contains the full complex field information, and thus allows direct as well as reciprocal space imaging of SP fields. In commonly used infinity corrected microscope objectives a reciprocal space image is already formed in the back focal plane (BFP) inside the objective. Consecutive Fourier and inverse Fourier transforms can be performed by using two lenses in f-f configurations [42] as shown in Fig. 3.2(a) to reproduce this back focal plane on a camera. Alternatively, the BFP can be imaged using a single lens, e.g., in a $2f$-$2f$ configuration.

As seen from Fig. 3.2(b), the achieved reciprocal space image displays linearly scaled k-space (black), i.e., the image coordinate $\mathbf{x}_{\mathrm{FS}}$ is proportional to the in-plane wavevector $\mathbf{k}_{||}$, confirming that a genuine Fourier transform is performed. However, for a simple thin lens of focal length f in an f-f configuration, ray-optics predicts scaling of the image plane as

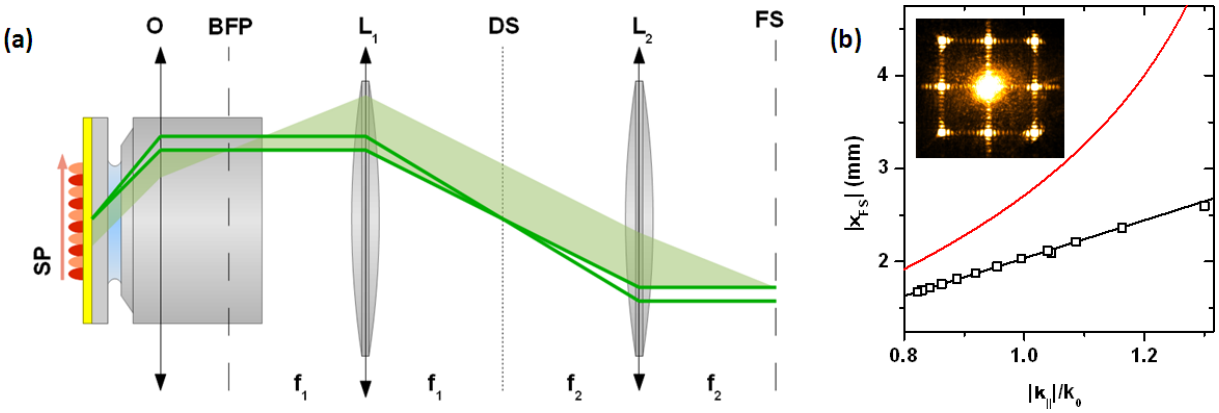

Figure 3.2.: Reciprocal space imaging: (a) Sketch of the optical beam paths in a LR microscope. A reciprocal space image is produced in the back focal plane (BFP) of the objective. The image is transformed by two lenses L_1 and L_2 to form consecutive direct space (DS) and Fourier space (FS) images, respectively. - (b) Scaling of the reciprocal space by analysis of the diffraction pattern of $\lambda_0 = 633$ nm light incident on a hole array with period $P = 760$ nm, imaged with an NA=1.3 objective. The radial coordinates $|\mathbf{x}_{\mathrm{FS}}|$ of different features of the diffraction pattern are plotted versus their theoretically expected radial in-plane wavevector $|\mathbf{k}_{||}|$ (open squares). A clear linear relationship is observed. Curves $|\mathbf{x}_{\mathrm{FS}}| = f \tan(\arcsin(|\mathbf{k}_{||}|/nk_0))$ (red line) and $|\mathbf{x}_{\mathrm{FS}}| \propto |\mathbf{k}_{||}|/k_0$ (black line) are depicted for comparison.

$|\mathbf{x}_{\mathrm{FS}}| = f \tan(\arcsin(|\mathbf{k}_{||}|/nk_0))$ (red curve). The observed linear scaling can be understood as the applied objectives are corrected to fulfill Abbe's sine-condition [9]. If subsequently only imaging in the paraxial limit is performed, $\tan(\arcsin(|\mathbf{k}_{||}|/nk_0)) \approx |\mathbf{k}_{||}|/nk_0$ holds and the linearity is preserved in all conjugate reciprocal space planes. Such linear scaling will be important for a variety of measurements presented throughout this thesis.

Collected Fields

As LR microscopy is based on far-field immersion microscopy, usually also fields other than SP leakage radiation are collected. For this thesis, SPs launched by illuminating a metal nanoaperture with dedicated incident field distributions have been investigated (see section 2.2.1). As illustrated in Fig. 3.3(a), on such structures the incident field is diffracted on the upper side of the metal, and SPs are launched. Light is also directly transmitted through the semi-transparent film and through the nanoaperture. On the lower interface, the transmitted light is again diffracted, and SPs are launched on this interface as well.

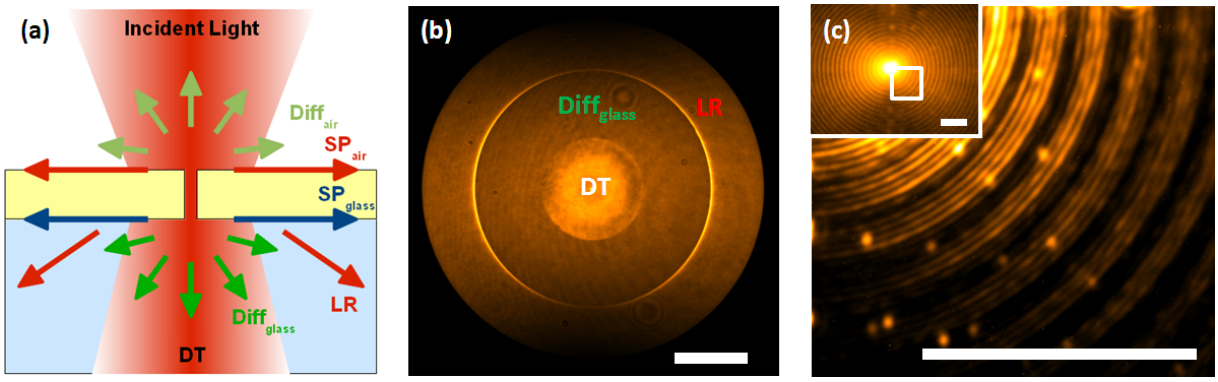

Figure 3.3.: Light components collected by a LR microscope: (a) By illuminating a nanostructure, light is diffracted to the air ($\mathrm{Diff_{air}}$) and SPs are launched on both interfaces ($\mathrm{SP_{air}}$, $\mathrm{SP_{glass}}$). Immersion microscopy collects light diffracted into the substrate ($\mathrm{Diff_{glass}}$), direct transmission (DT) and leakage radiation (LR). - (b) Reciprocal space LR microscopy image of an SP launched by a single hole (see Fig. 2.6). A circle of directly transmitted light (DT) with a diameter corresponding to the numerical aperture of the illumination objective is visible in the center. An almost constant background stems from diffraction to the glass ($\mathrm{Diff_{glass}}$), and plasmon LR is located on a circle with a radius corresponding to the SP wavevector. The scale bar corresponds to 5 $\mu\mathrm{m}^{-1}$. - (c) Real space image corresponding to the situation in (b), acquired with two different magnifications. Radial patterns with short and long periods can be identified, which are attributed to the interference of plasmon LR and diffracted light [141]. Scale bars correspond to 10 µm.

The unperturbed transmitted incident field, as well as diffraction on the substrate-metal interface and LR of SPs on the air-side contribute to the full signal detected by a LR microscope. The different components can be identified in reciprocal space LR images, as shown for a single nanohole in Fig. 3.3(b). The coherent superposition of diffracted transmission and LR also leads to a modification of the radial Lorentzian intensity distribution of the SP resonance circle to form so called Fano profiles. The asymmetry of such lineshapes will be applied at a later stage for improving SP sensing (see chapter 7).

Just as in the case of reciprocal space images, direct space images also contain information of all the collected fields. At the level of the metal back interface the propagating SP field is spatially separate from the diffracted and transmitted light fields, which are localized at the level of the nanohole. However, this interface is imaged with a diffraction limited immersion microscope, i.e., the collected angular spectrum is limited to the numerical aperture of the microscope objective. Thus an inverse Fourier transform of the discussed reciprocal space image will result in an Airy-like image of the nanohole. It has been shown in [141] that the direct space superposition of this Airy diffraction pattern and the SP wave leads to interference patterns beating at two different periodicities, $P_\mathrm{s} = 2\pi/(\mathrm{NA}k_0 + k'_\mathrm{SP})$ and $P_\mathrm{l} = 2\pi/(\mathrm{NA}k_0 - k'_\mathrm{SP})$. As shown in Fig. 3.3(c) for an SP at $\lambda_0 = 782$ nm on an 80 nm thick gold film, theoretical values $P_\mathrm{s} = 0.311$ µm and $P_\mathrm{l} = 1.67$ µm show good agreement to experimentally extracted periodicities $P_\mathrm{s} = 0.313$ µm and $P_\mathrm{l} = 1.77$ µm. Note that, while the long periodic oscillation is readily apparent as an inherent artifact in nearly every image presented in this thesis (compare, e.g., Fig. 2.6), aberration-corrected objectives have to be used to observe the subwavelength short period beating pattern.

It remains to be addressed which vectorial field component E_i of the SP field (E_x, E_y, E_z) is actually monitored by LR microscopy. From the Fresnel-coefficient based derivation of SP dispersion it follows that LR intensity is proportional to the corresponding SP intensity [21], and indeed, from comparison to SNOM images, LR microscopy has been reported to mimic the intensity profile of SPs [52, 82].

However, recent studies on the interference of SP beams propagating in orthogonal directions suggested that it is actually the in-plane field component of the SP that is imaged [142]. To understand the origin of this observation, one has to take into account the polarization characteristics of leakage radiation. Although proportional to the corresponding SP intensity, LR is transversely polarized as a propagating wave. In a paraxial imaging setup, this causes approximately radial polarization of the SP circle in reciprocal space, and predominately in-plane polarization of the superimposed leakage radiation in direct space. Due to this in-plane polarization, which is artificially enforced

by the paraxial imaging system, images are produced which *mimic* the in-plane field component of the SP.

Optimal Film Thickness

Thin films are required for LR microscopy as they allow tunnelling of SPs to propagative modes in the glass substrate. However, LR itself also represents an additional loss channel for SPs, causing broadening of SP resonances and decrease in propagation lengths with decreasing film thickness h. In choosing appropriate film thicknesses for LR, it is therefore crucial to solve this trade-off between achievable SP propagation lengths $L_{\mathrm{SP}}^{h} = 1/2k_{\mathrm{SP}}''$ and LR signal intensity I_{LR} in an optimal way.

According to the discussion presented in section 2.1.2, the LR signal intensity relative to the SP intensity can be calculated as $I_{\mathrm{LR}}/I_{\mathrm{SP}} = \exp(-2\mathrm{Im}(\sqrt{\varepsilon_{\mathrm{Au}}k_{\mathrm{SP}}^2 - k_0^2})h)$. This normalized intensity, together with the propagation length $L_{\mathrm{SP}}^{h}/L_{\mathrm{SP}}^{\infty}$ of an SP on a thin film normalized to the one at the interface of a metal half-space, is shown as a function of the thickness h in Fig. 3.4 for SPs on glass-gold-air systems. A saturation of the propagation length to its material dissipation limited value is observed for thicknesses above ~ 100 nm, while LR signal intensity linearly decreases due to the proportionality between $\ln(I_{\mathrm{LR}}/I_{\mathrm{SP}})$ and the film thickness.

Thicknesses corresponding to equal radiative and dissipative loss rates for SPs are chosen

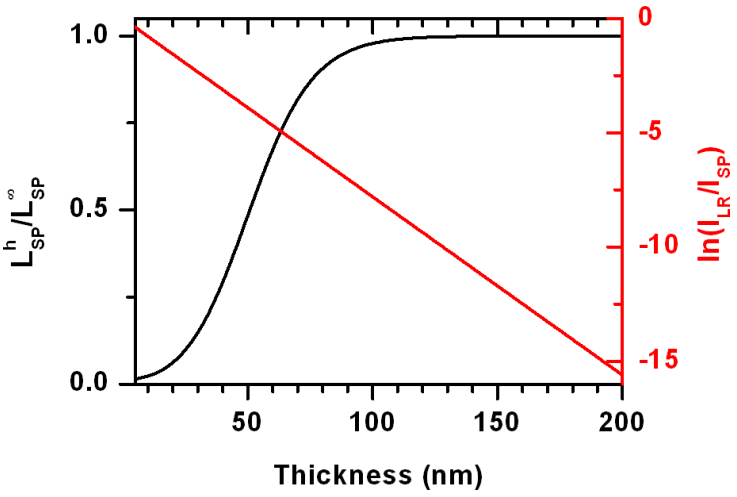

Figure 3.4.: Normalized SP propagation length $L_{\mathrm{SP}}^{h}/L_{\mathrm{SP}}^{\infty}$ (black) and LR signal intensity $I_{\mathrm{LR}}/I_{\mathrm{SP}}$ (red) as a function of the metal film thickness h, calculated for SPs on the gold-air interface of a glass-gold-air system at $\lambda_0 = 782$ nm from the poles of the Fresnel reflection coefficients.

most commonly for LR microscopy (50 nm for the shown glass-Au-air system) [54, 142, 143]. Such thicknesses cause minimum reflectivities in ATR geometries, corresponding to perfect coupling of free-space light to SPs.

However, such a thickness also leads to a reduction of the SP propagation length by 50%. As for most applications observation of SPs over the longest possible distance is the primary target, it is crucial to keep the reduction of the propagation length at a minimum. Thus the use of thicker films is to be preferred, as long as the achievable LR signal levels are at an acceptable level relative to the detection threshold given by the light sources and the detectors. For most experiments carried out during this thesis, a thickness of 80 nm was chosen. At such a thickness the propagation length of $L_{\mathrm{SP}}^{h}/L_{\mathrm{SP}}^{\infty} > 90\%$, and yet sufficiently large LR signals are detected with the optical setup presented in the following.

3.2.2. Optical Setup

The optical setup which has been developed to perform most experiments reported in this thesis is presented in Fig. 3.5. In its core, it consists of a high numerical aperture immersion objective collecting LR from the substrate side of a thin gold film. Both a Nikon Plan Fluor, NA=0.5-1.3, 100× and a Nikon Apo TIRF, NA=1.49, 60× objective are used, the latter being especially required for imaging all SP effects in high-index environments such as water. Illumination of nanostructure sources is performed by objectives of different numerical apertures in a range of NA=0.1 to NA=0.6. Illumination objective, sample and immersion objective are mounted on xyz-translation stages featuring 0.5 µm precision to allow precise alignment of the nanostructures and the illumination field.

A variety of light sources can be coupled to the system. A pigtailed transverse single mode 25 mW laser diode emitting around 785 nm (DL-4140-001S), or alternatively a replacement emitting at 782 nm, have been used for SP excitation in most experiments. For characterizing bandgap structures for particle micromanipulation as discussed in chapter 6, a more powerful 330 mW transverse and longitudinal single mode fiber Bragg-grating stabilized diode at 975 nm has been chosen (Thorlabs PL980P330J). A visible low-power helium-neon gas laser (632 nm) and a halogen lamp are also available for alignment and scaling purposes.

An important capacity of LR microscopy is polarization control. This is achieved by implementing a thin-film cleaning polarizer and broadband half-wave and quarter-wave plates. The laser beams are expanded by a Galilean telescope to provide approximately

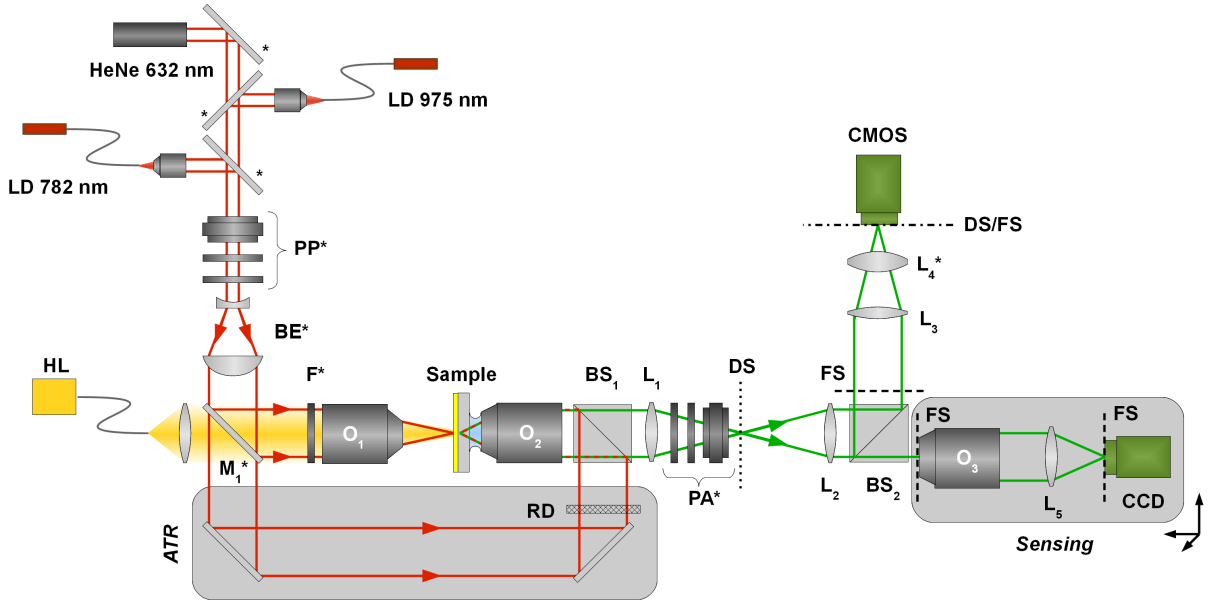

Figure 3.5.: LR microscopy setup: The illumination beam path (red) consisting of a helium-neon (HeNe) laser emitting at 633 nm, two laser diodes (LD) at 782 nm and 975 nm, a polarizer as well as half-wave and quarter-wave plates for polarization preparation (PP), a beam-expander (BE), a spatial filter (F) and an illumination objective (O_1). A halogen lamp (HL) can be used for white-light illumination of the sample. The detection path (green) comprises a high NA immersion objective (O_2), half-wave and quarter-wave plates as well as a polarizer for polarization analysis (PA), several lenses (L_1-L_4) to perform Fourier transforms and a CMOS camera. Intermediate direct space (dotted, DS) and Fourier space (dashed, FS) planes allow spatial filtering. In addition, the sample can be back illuminated in an ATR-like configuration through a rotating diffuser (RD) using a first beam-splitter (BS_1). Through a second beam splitter (BS_2) an intermediate Fourier plane is magnified by an additional microscope objective and imaged by a lens (L_5) on a CCD camera for refractive index sensing purposes. Removable components mounted on flip-mounts are marked with an asterisk.

constant illumination of the back-aperture of the illumination objective. Crucial for a variety of later experiments is the possibility of spatial filtering the incident light close to the back focal plane of the illumination objective. Variable slit and iris apertures can be applied to control the divergence of the SP launching field.

LR is projected by two consecutive f-f configurations on intermediate direct space (dotted) and reciprocal space (dashed) planes. By flipping lens L_4 in or out, reciprocal or direct space can be imaged on the CMOS array. The intermediate planes provide the possibility to perform spatial filtering in real as well as in reciprocal spaces [42]. The latter is an extremely powerful tool for a variety of tasks. Suppression of the nanoaperture by spatial filtering in the direct space allows one to observe pure LR images in reciprocal space, and

hence to collect genuine Lorentzian resonances, a technique applied in chapter 7. Spatial filtering in an intermediate reciprocal space plane, on the other hand, enables to a large extent the suppression of direct transmission to prevent overexposure of real-space images at the level of the nanoaperture. In addition, the origin of different field components can be easily identified by selective spatial filtering. In particular, plasmonic features in real space can be well distinguished from other field components by comparison to an image where the SP circle has been blocked in reciprocal space [143].

Another technique used to suppress direct transmission is polarization post-selection in the imaging beam path, polarized orthogonally to the incident polarization state. For this purpose, polarization analyzing elements are available in the imaging path of the optical system (PA). This technique has already been successfully applied for imaging SPs on hole arrays [144, 145], and is also used throughout this thesis when applicable. More sophisticated applications of polarization post-selection could reveal effects of optical angular momentum of light in plasmonic nanostructures [146, 147] or facilitate weak-measurements using SPs [148, 149].

Detection of the light field is performed by a standard CMOS sensor (Pixelink PL-B741-E). To improve noise properties of the acquired images, temporal averaging over 50 image frames is typically performed.

Besides the presented features, other non-standard techniques have been progressively implemented in the presented LR microscopy setup during this thesis, which will be presented next.

Sensing Extensions

In this thesis, LR microscopy reciprocal space imaging will be introduced as a tool for refractive index sensing. To allow sufficient magnification of reciprocal space with respect to detector pixel sizes, an intermediate reciprocal plane is magnified by a 60× objective (O_3) and an equivalent tube lens (L_5). The magnified image is collected by a CCD sensor (AVT Guppy Pro F-125B) with a 14bit A/D converter. The detector has been chosen in favor of an available scientific grade back-illuminated alternative CCD (Princeton Instruments PIXIS 1024x1024 EEV) due to its superior fixed pattern noise characteristics in the near-infrared [150]. Mounting of all components of this magnification path on a single xyz-translation stage facilitates simple scanning of the full reciprocal space. The beam-splitter BS_2 permits simultaneous imaging of real or reciprocal space plane while

performing sensing experiments.

To compare LR microscopy sensing performance to classic attenuated total reflection (ATR) geometries, an additional beam path is introduced by removal of mirror M_1, allowing back-side illumination of the sample, similar to a technique which has been demonstrated earlier [114]. For such experiments, speckle patterns of collected reflected intensity are a primary source of spatial signal fluctuations. A rotating diffuser (RD) has been introduced to reduce spatial coherence of the incident light and hence the visibility of such interference patterns. The sensing as well as the ATR path of the setup have been used for sensing experiments which will be presented in chapters 7 and 8.

High Dynamic-Range Imaging

A common problem in imaging SP fields over several propagation distances is the linear response of CCD or CMOS detectors. Due to the exponential decay of SPs, the LR signal can easily span several order of magnitude, which cannot be resolved by the limited dynamic range of common array sensors. Dynamic range (DR) shall be defined here as the ratio of the signal saturation level $I_{\max}$ to the minimum detectable level σ_I, measured in decibel: $\mathrm{DR/dB} = 20\log_{10}(I_{\max}/\sigma_I)$. For consumer grade CCD and CMOS sensors, dynamic ranges around 60 dB are typically achieved [151].

A variety of techniques have been developed to overcome this limitation for standard photography [151]. Among the most simple ones are multi-exposure techniques, relying on multiple captures of the same object at different exposure times of the detector array. The samples are subsequently merged to form one high dynamic-range image.

We implemented such a technique for LR microscopy by software-based post-processing

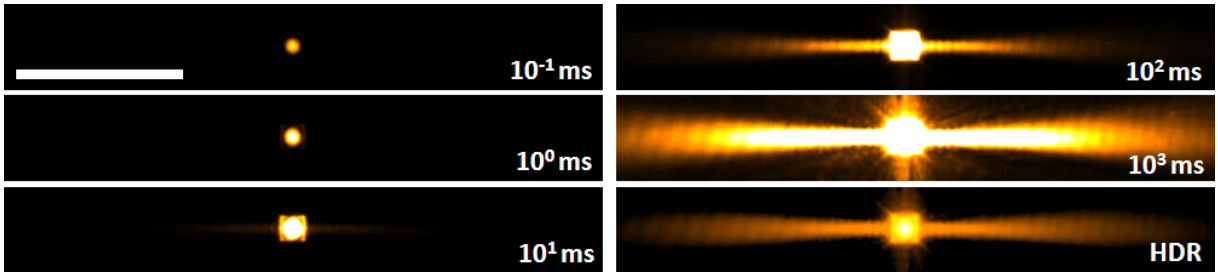

Figure 3.6.: High dynamic-range imaging: SPs launched by an array of 11×11 holes at $\lambda_0 = 782$ nm are imaged by LR microscopy choosing different exposure times. A high dynamic-range (HDR) image can be reconstructed as illustrated in the text and is depicted here in logarithmic scale. The scale bar corresponds to 50 µm

of the acquired frames. Images are taken for different exposure times t_i. For every pixel, the sample i taken at the highest possible exposure time is chosen at which the pixel is not yet saturated, a so called last-sample before saturation algorithm [151]. The pixels are background corrected and, assuming a linear response of the applied detector, each pixel intensity is weighted by the inverse of the exposure time. An example of an SP launched by a nanohole array is depicted in Fig. 3.6 for exposure times in a range of 10^{-1} ms to 10^{3} ms. The resulting high-dynamic range image is presented in logarithmic scale, displaying quantitative intensity information over a range of 108 dB.

Part II.

Surface Optical Elements

4 Refractive Optical Elements for Surface Plasmons

Various methods of molding the flow of SPs have already been discussed in chapter 2.2.2. One particular method to control the propagation of SPs is the use of refractive optical elements, which is illustrated in Fig. 4.1. The effective index of a SP on a metal surface with the dielectric constant ϵ_m depends on its dielectric environment ϵ_d:

$$k_\mathrm{SP} = k_0 \sqrt{\frac{\epsilon_\mathrm{m}\epsilon_\mathrm{d}}{\epsilon_\mathrm{m}+\epsilon_\mathrm{d}}} =: k_0 \left(n_\mathrm{SP}^\mathrm{eff} + i\gamma_\mathrm{SP}^\mathrm{eff}\right) \tag{4.1}$$

Similar to classic refractive optics, varying ϵ_d and thus the effective index $n_\mathrm{SP}^\mathrm{eff}$ has been reported to allow the design of refractive optical elements such as prisms and lenses [52, 152].

In this chapter, the study of refractive plasmonic components will be extended. First, homogeneous dielectric elements will be discussed. Subsequently, a metamaterial approach will be presented which allows to locally vary the refractive index in such elements. It

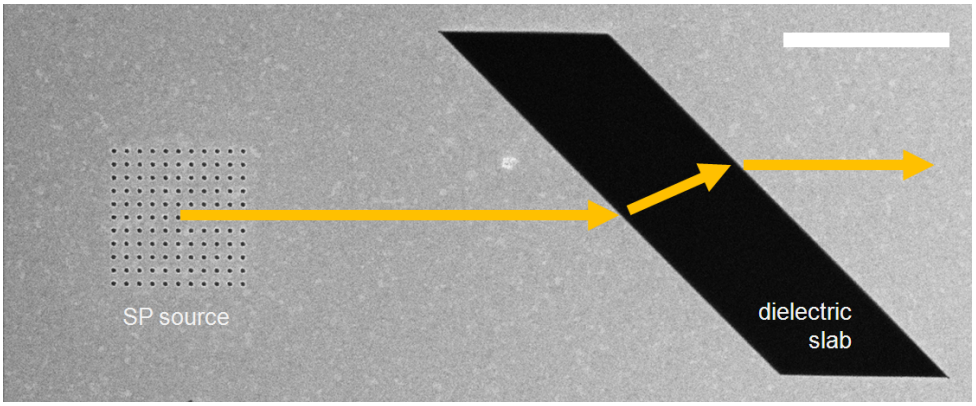

Figure 4.1.: Refractive Optical Elements for SPs - SPs are launched, e.g., by a nanohole grating, with an effective index $n_{\mathrm{SP,\ air}}^\mathrm{eff}$. At the interfaces of a dielectric element characterized by an effective index $n_{\mathrm{SP,\ diel}}^\mathrm{eff}$ they are refracted according to the Snell-Descartes law.

will then be shown how this is applied to the fabrication of gradient-index prisms and lenses. Parts of the results presented in this chapter have been published in 2010 in Optics Express [1] (© 2010 The Optical Society).

4.1. Basic Optical Components

Before turning to more sophisticated geometries, we studied the manipulation of SP beams by homogeneous dielectric optical elements, similar to those already presented in [52, 152].

First Au films of 50 nm thickness were deposited on glass coverslips by electron-beam evaporation. Dielectric elements were fabricated from poly(methyl methacrylate) (PMMA). Besides its well understood lithographic processability, PMMA also offers possible applications in active plasmonics through doping with, e.g., molecules or semiconductor nanocrystals [71, 78, 153, 154].

A 119 ± 4 nm thick PMMA film (3% weight per weight (w/w) solution of Sigma-Aldrich PMMA with a molecular weight $M_{\mathrm{W}} = 9.96 \times 10^5$ in anisole) was deposited on the substrates by spin-coating for 2 min at 2000 rpm. Structures were written in the films by electron-beam lithography using the SEM column of an FEI Strata Dual Beam 235. PMMA is commonly used as a positive resist. However, by overexposure PMMA chains can be cross-linked and the material acts as a negative resist with around 50 nm lateral resolution [155]. Subsequent development for 3×30 s in trichloroethylene at 70°C yielded structures such as the ones appearing in black in Figs. 4.2(a) and (c).

Standard SP sources consisting of arrays of nanoholes (see discussion in chapter 2.2.1) were milled close to the dielectric elements by focused ion-beam lithography using the ion-beam column of the FEI Dual Beam.

The structures were analyzed in the standard LR microscopy configuration discussed in chapter 3.2.2: SPs were excited by focusing an expanded $\lambda = 785$ nm laser beam by a Nikon Plan Fluor NA = 0.13 objective on the source grating. Images were acquired using a Nikon Plan Fluor NA = 1.3 oil immersion objective. Far-field scattering analysis and SNOM studies were also performed on similar structures [1], but are not discussed further here.

A resulting LR micrograph of a fabricated prism is presented in Fig. 4.2(b). Assuming the Snell-Descartes law to hold, the effective refractive index of the PMMA structure was deduced to be $n_{\mathrm{SP}}^{\mathrm{eff}} = 1.37$ from the SP beam displacement. Comparing this to calculations

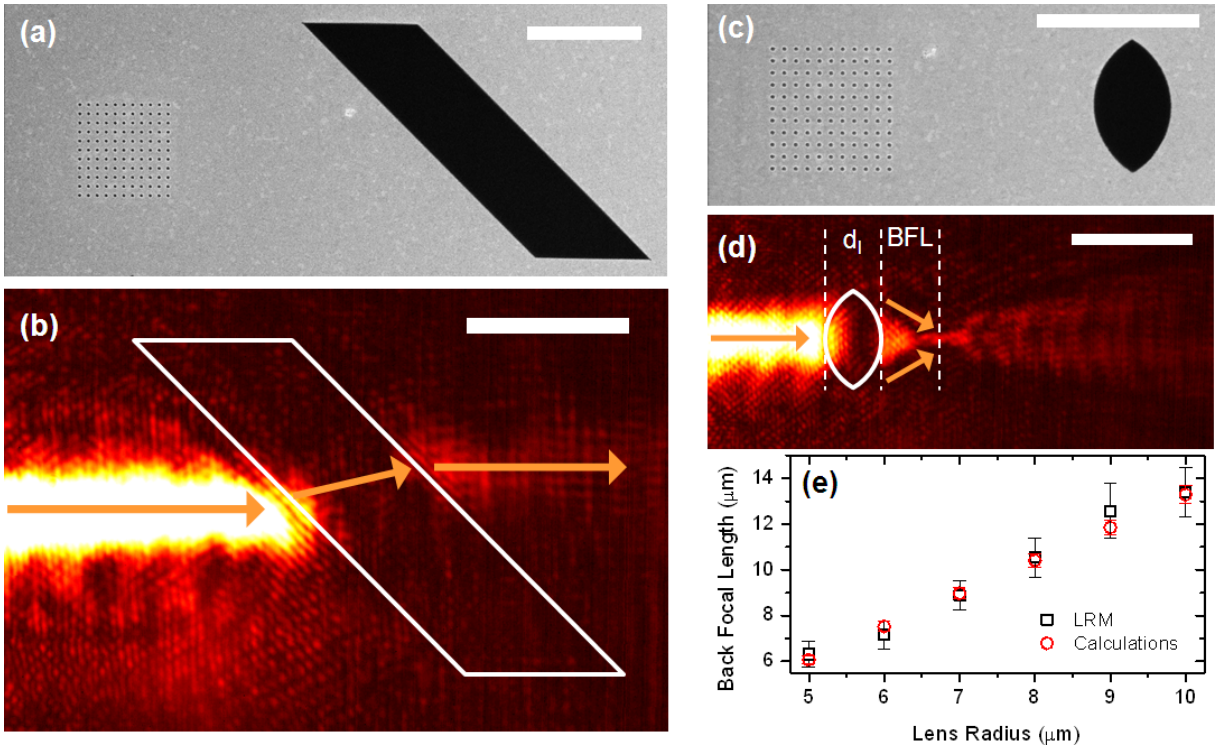

Figure 4.2.: Refractive prisms and lenses - (a)+(c) SEM images of a plane parallel slab (a) and a lens of width $d_l = 5$ µm and radius $R = 5$ µm (c), respectively, both consisting of 119 ± 4 nm PMMA on a 50 nm thick Au film. Nanohole arrays (11×11 holes, diameter $D = 220$ nm, periodicity $P = 770$ nm) are used as SP sources. - (b)+(d) LR microscopy images of SPs manipulated with the depicted refractive structures. All scale bars corresponds to 10 µm. - (e) Dependence of the back focal length of dielectric lenses on the lens radius R. Experimental LR microscopy data (black squares) are compared to values predicted by the classic lens makers formula (4.2) (red circles). Errors have been estimated by Gaussian propagation of uncertainty in determinating the focal and lens positions from images for experimental values (black), and propagation of uncertainty of the film height for calculations (red), respectively.

for the poles of the Fresnel-coefficients of a 119 nm thin PMMA film between infinite Au (refractive index data from [6]) and air half spaces, an effective index of $n_{\mathrm{SP}}^{\mathrm{eff}} = 1.38$ was found, which compares well to the experimental result. Note that SPs are not visible in the LR microscopy images when propagating inside the PMMA structures, as they leak outside of the light-cone of the chosen collection objective ($n_{\mathrm{SP}}^{\mathrm{eff}} > \mathrm{NA} = 1.3$). An objective with a higher NA could be used to overcome this problem.

Dielectric lenses with varying radii of curvature R were also prepared. An example is shown in Fig. 4.2(c). The back focal lengths (BFL) of the lenses were determined experimentally by LR microscopy. The results are given in Figs. 4.2(d-e). Assuming $n_{\mathrm{SP}}^{\mathrm{eff}} = 1.38$, they

compare well with calculated BFLs according to the classic lens-maker formula [156]

$$\mathrm{BFL} = f\left(1 - \frac{(n_{\mathrm{SP}}^{\mathrm{eff}} - 1)d_l}{n_{\mathrm{SP}}^{\mathrm{eff}} R}\right) \text{ with } \frac{1}{f} = (n_{\mathrm{SP}}^{\mathrm{eff}} - 1)\left(\frac{2}{R} - \frac{(n_{\mathrm{SP}}^{\mathrm{eff}} - 1)d_{\mathrm{l}}}{n_{\mathrm{SP}}^{\mathrm{eff}} R^2}\right). \tag{4.2}$$

Note that the incident SP beam excited by an NA = 0.13 illumination objective is only weakly diverging, and can be treated as a collimated beam for the presented focusing experiments. For experiments in plasmonic crystal gratings which will be presented in subsequent chapters, however, implementing higher degrees of collimation will become crucial.

The discussed results show that refractive optical elements operate and can be modelled analogously to free-space refractive optics. However, refractive plasmonic devices have one major disadvantage, which is visible from the damping of the SP beams in LR microscopy pictures: at the structure interfaces, SPs are not only refracted, but also scattered out of plane to propagating light. Sharp edges therefore always represent a loss channel for SPs. In fact, such scattering losses turn out detrimental in implementing more complex geometries. This is why overcoming this problem is important, and possible solution will be presented at the end of this chapter.

4.2. Refractive Metamaterial Structures

Above it was discussed how the geometrical shape of refractive elements could be exploited for SP beam control. A higher degree of freedom could be achieved by the ability to precisely control the effective index $n_{\mathrm{SP}}^{\mathrm{eff}}$ for SPs. One straightforward approach, but complicated to implement, would be to tune the PMMA film thickness, e.g., by grayscale electron-beam lithography [54].

We decided to implement a metamaterial consisting of equally spaced dielectric rods. In a similar fashion, a metamaterial of metal nanoparticles with subwavelength spacing has been designed recently [159]. Calculations using the differential method [157, 158] suggested that the effective index of such a medium of dielectric rods can be finely tuned by varying the lateral filling factor (FF) describing the ratio of the surface filled with dielectric material (Fig. 4.3(b)).

Samples were fabricated by deposition of a PMMA film on top of a thin gold layer according to the procedure presented above. Again by using electron-beam lithography with PMMA as a negative resist, rectangular slabs consisting of dielectric rods with varying spacings

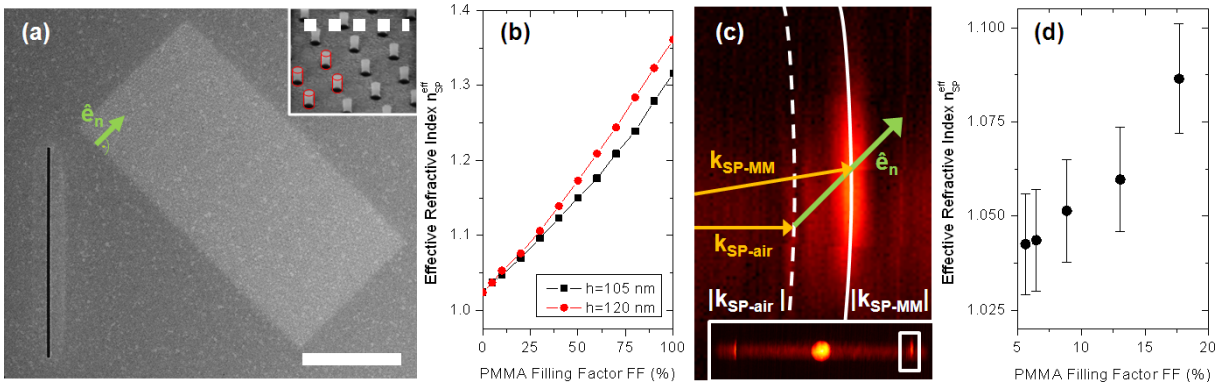

Figure 4.3.: (a) SEM image of a rectangular slab (15×30 µm^2) made of PMMA rods of 91 ± 5 nm diameter and a height of $h_{\mathrm{PMMA}} = 106$ nm. A nanoslit (250 nm wide, 20 µm long) is used as an SP source. An SEM zoom of the rods taken at 52° is shown in the inset. The interface normal $\hat{\mathbf{e}}_\mathbf{n}$ is marked by the green arrow, scale bars correspond to 10 µm (continuous) and 1 µm (dashed), respectively. - (b) Dependence of the SP refractive index $n_{\mathrm{SP}}^{\mathrm{eff}}$ on the lateral PMMA filling factor (FF), determined from calculations using the differential method [157, 158]. - (c) LR microscopy image in reciprocal space of SPs in an effective index medium (FF=0.18). The inset shows the full reciprocal space. The magnified area (white box) demonstrates the shift of the SP resonance from $\mathbf{k}_{\mathrm{SP\text{-}air}}$ along the interface normal $\hat{\mathbf{e}}_\mathbf{n}$ to the SP wavevector in the metamaterial $\mathbf{k}_{\mathrm{SP\text{-}MM}}$. - (d) $n_{\mathrm{SP}}^{\mathrm{eff}}$ variation with FF, controlled by varying the rod spacings from 220 nm to 360 nm, determined from measurements of the direction $\hat{\mathbf{k}}_{\mathrm{SP}}$ of the SP wavevector in LR microscopy reciprocal space images. Errors have been estimated by Gaussian propagation of the uncertainty in $\hat{\mathbf{k}}_{\mathrm{SP}}$ measurement.

smaller than $\lambda_{\mathrm{SP}}/2$ were prepared. A typical structure is depicted in Fig. 4.3(a).

To experimentally characterize the effective index of the slabs, slits were milled in the gold films by FIB lithography. LR microscopy experiments were performed with similar excitation and detection conditions as discussed above. LR micrographs of the reciprocal space have been acquired and an example is shown in Fig. 4.3(c). The illustration recalls that Snell's law corresponds in reciprocal space to a change of the wavevector along the interface normal by conservation of wavevector components along the interface plane:

$$|(\mathbf{k}_{\mathrm{SP\text{-}MM}} - \mathbf{k}_{\mathrm{SP\text{-}air}}) \times \hat{\mathbf{e}}_n| = 0 \tag{4.3}$$

Angular fits of the SP resonances inside the slabs were used for calculating equivalent effective indices which are presented in Fig. 4.3(d). A good agreement between the measured $n_{\mathrm{SP}}^{\mathrm{eff}}$ and the ones calculated with the differential method was observed. Note that the range of achieved $n_{\mathrm{SP}}^{\mathrm{eff}}$ is still rather limited. A larger range could potentially be explored by changing the index of the polymer or by using PMMA as a positive resist,

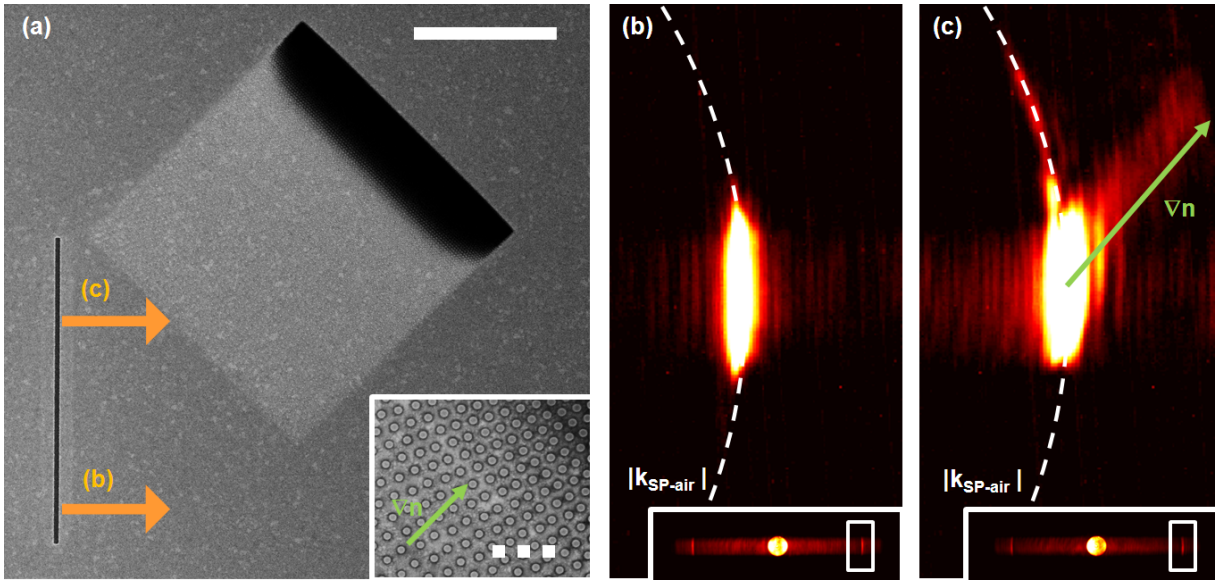

Figure 4.4.: GRIN slab - (a) SEM image of a GRIN slab (20×20 µm^2) and a nanoslit source (250 nm wide, 20 µm long). The direction of increase in rod spacing defining the index gradient ∇n is shown in the inset. The scale bars correspond to 10 µm (continuous) and 1 µm (dashed). - (b)+(c) LR micrographs in reciprocal space of SPs propagating outside (b) and inside (c) the GRIN structure, respectively. While in (b) just the mere SP resonance is visible, (c) demonstrates modulation of $\mathbf{k}_{\mathrm{SP}}$ along the direction of the index gradient ∇n.

providing resolution below 10 nm [155], but requiring a more complex fabrication process to allow implementing free-standing devices.

4.3. Gradient-Index Optics

Modulation of the effective refractive index for SPs by control of the density of dieletric rods has been demonstrated. Spatially varying the spacing of these rods would thus allows the fabrication of structures with spatially varying refractive indices, analogous to free-space gradient-index (GRIN) structures. Similar approaches have more recently also found application in the field of transformation optics [53, 54].

To investigate plasmonic GRIN effects, a plane parallel slab with a gradient in index due to a spatially varying filling factor was fabricated and is depicted in Fig. 4.4. Again a nanoslit was chosen as SP source. The structure was analyzed in a similar LR microscopy configuration as above. Illuminating the lower part of the slit launched SPs propagating outside the GRIN structure, corresponding to a simple SP resonance in reciprocal space

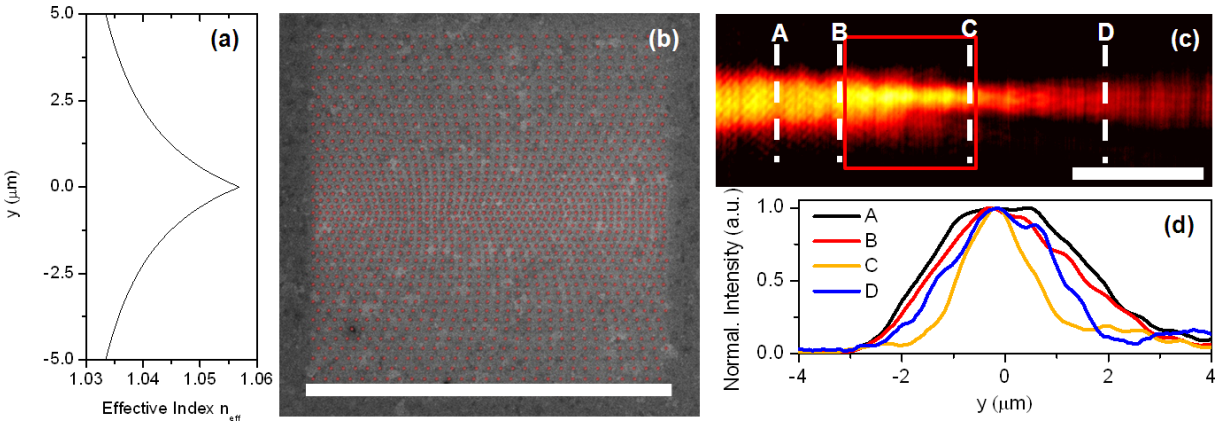

Figure 4.5.: GRIN lens - (a) Variation of the effective index of the GRIN lens shown in (b) - (b) SEM image of a GRIN lens (10×10 µm^2) made of PMMA rods (diameter 65 nm, height 120 nm, colored in red for clarity) - (c) LR micrograph of SPs launched by a hole array (11×11 holes, diameter $D = 250$ nm, periodicity $P = 760$ nm, not shown here) propagating though the lens (red square). The scales bars correspond to 10 µm. - (d) Beam profiles along the planes marked in (c) demonstrating the focusing effect.

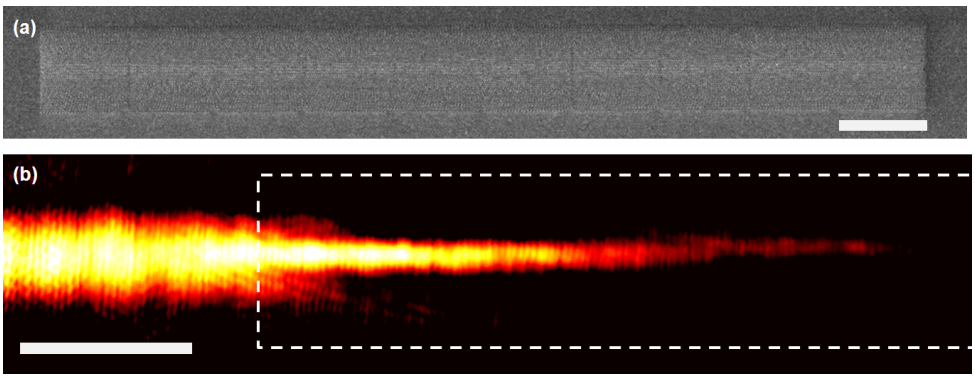

Figure 4.6.: GRIN waveguide - (a) SEM image of GRIN waveguide consisting of 10 stitched GRIN lenses. - (b) LR micrograph of SPs launched by a nanohole array (11×21 holes, $D = 250$ nm, $P = 760$ nm) propagating inside the waveguide (dashed box). Scale bars correspond to 10 µm.

as visualized in Fig. 4.4(b). However, SPs launched to propagate inside the GRIN slab (Fig. 4.4 (c)) change their wavevector $\mathbf{k}_{\mathrm{SP}}$ along the direction of the index gradient $\boldsymbol{\nabla} n$ up to k_{SP} values outside of the NA of the applied objective. This corresponds to continuous steering of the SP beam inside the GRIN slab due to a variation of the effective index from $n_{\mathrm{SP}}^{\mathrm{eff}} = 1$ up to values $n_{\mathrm{SP}}^{\mathrm{eff}} > \mathrm{NA}$.

An application of this effect is demonstrated in Fig. 4.5. GRIN lenses with index gradients pointing from the horizontal edges to the device axis as shown in Fig. 4.5(a) were fabricated. SPs were launched by arrays of nanoholes similar to the ones shown in Fig. 4.2. LR

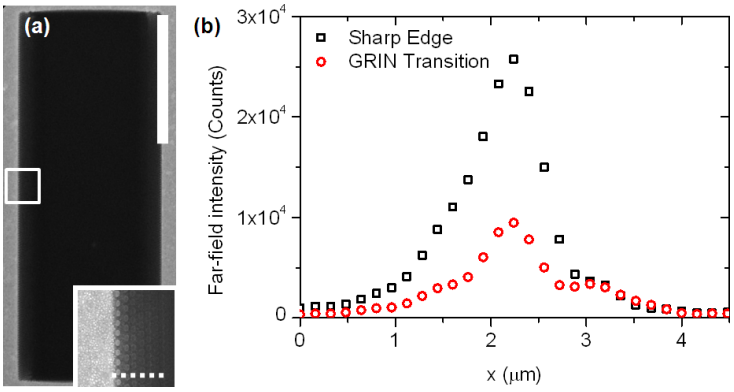

Figure 4.7.: (a) SEM image of a PMMA slab (10×30 µm^2, 120 nm thick) with a 2 µm wide GRIN transition region. Scale bars corresponds to 10 µm (continuous) and 1 µm (dashed), respectively. - (b) Cross-sections of the scattered intensity across the input edge of the PMMA slabs. Scattering with GRIN transition (red) is reduced 2.4-fold compared to a homogeneous slab of same dimensions (black).

micrographs of the SP propagating inside the GRIN lens, as well as corresponding cross-sections are depicted in Figs. 4.5(c) and (d), respectively. The SP beam width was reduced by a factor of 2.3 when exiting the device, demonstrating focusing by the GRIN lens without significant scattering loss at the flat lens interface. Tailoring of the index gradient to, e.g., commonly used parabolic profiles [160] is expected to yield further improvement of the lens characteristics, such as aberration correction.

Apart from their application as lenses, GRIN profiles are commonly also used in multimode fibers to achieve reduced intermodal dispersion. In a preliminary study we thus tried to explore the applicability of plasmonic GRIN structures for SP waveguiding.

Multiple GRIN lenses similar to the ones presented above were prepared and stitched to form a waveguide. SEM and LR microscopy images are shown in 4.6. Although the stitching was performed by FIB stage movements and hence was not very accurate, a localization of light at the waveguide core is clearly visible. The structure could thus be a promising approach to improve dielectric loaded SP waveguiding. Its waveguiding properties, however, were not studied further as part of the present work.

Another interesting application of GRIN structures lies in overcoming the scattering losses which were observed in homogeneous refractive elements. Homogeneous rectangular PMMA slabs were prepared, once with and once without a GRIN transition region. An SEM micrograph is shown in Fig. 4.7(a). Nanohole arrays similar to the ones discussed above were prepared to launch SPs incident normal to the structure interface.

Scattering losses were analyzed in a far-field configuration by replacing the collection immersion objective of the LR microscopy setup with a Nikon S Plan Fluor ELWD 40x NA=0.60 microscope objective. The nanoslit was illuminated from the sample substrate side, scattered light was collected from the Au interface. Cross-sections along the device interface are depicted in Fig. 4.7 and suggest a decrease of already a factor 2.4 of the scattered intensity, integrated over the devices interface. Thus tapering refractive SP optics by index gradients appears as a very promising means to overcome scattering losses as the ones observed in the first part of this chapter.

4.4. Conclusions

In this chapter refractive micro-optical devices for the manipulation of propagating surface plasmons were presented. Homogenous slabs and lenses were fabricated, and the classic lens-maker formula was shown to hold for such elements. The effective refractive index of SPs was rendered tunable by a metamaterial made of dielectric rods. Lateral spatial variation of the index using such a material system led to the development of gradient index structures. Such gradients could furthermore be applied to reduce scattering loss from device interfaces. We thus hope that the presented approach finds further application for optimization of the loss properties of homogenous dielectric plasmonic components, as well as for the design of other gradient index or also transformation optical devices.

5 Surface Plasmon Beams in Metal Gratings

Dielectric materials of periodically varied refractive indices in one, two or three dimensions have been studied for more than two decades as one of the most promising candidates for integrated dielectric optics [161]. These so called photonic crystals can possess a full bandgap for photons of specific energy. This property has been widely exploited to fabricate defect waveguides, high-quality photonic cavities or photonic-crystal fibers, just to name a few (for a comprehensive review see, e.g., [162]).

More recently, the design principles for photonic bandgap materials have been applied in the field of surface plasmon optics. By periodic arrangement of metallic or dielectric features plasmonic crystals with a full bandgap for SPs have been implemented [61]. A multitude of integrated components has been demonstrated, such as, e.g., SP waveguides [64], SP Bragg mirrors [57, 62, 63], and devices for SP wavelength multiplexing and dispersion [65, 163] and for slow light SPs [66].

In this chapter first a brief introduction on Bloch modes in photonic crystals will be given. Effects of the grating amplitude on propagation losses and bandgap widths in plasmonic crystals will be discussed, and a demonstration of simple SP Bragg mirrors will be presented. Inspired by the pioneering work of Zengerle and Russell on dielectric waveguides [164–166], it will further be shown how the bandstructure of one-dimensional plasmonic crystals can be exploited for SP beam steering. By probing the fine structure of bands it was possible to implement a plasmonic analogue of the classic superprism effect [167]. Diffraction in such gratings was also observed to lead to negative refraction without the need of a negative index material [168], which thus experimentally verified recent theoretical proposals [169–171]. Extension of these conditions to two-dimensional gratings will be shown to lead to so called "all-angle" negative refraction. The chapter will be concluded by a discussion of self-collimating SP beams in such 2D gratings, leading to weakly diffracting SP beam propagation over several hundreds of microns. Parts of

the results presented in this chapter have been published in Physical Review Letters in 2010 [2] (© 2010 American Physical Society) and Optics Letters in 2012 [3] (© 2012 The Optical Society).

5.1. Plasmon Modes in Sinusoidal Metal Gratings

As already mentioned above, light in materials with a periodically modulated refractive index possesses a particular mode structure. Assuming infinite size of the grating, the behavior of a photon in such a material can be understood with the help of Bloch's theorem, in analogy to electrons in periodic potentials. A one-dimensional modulation with a period P in direction $\hat{\boldsymbol{\xi}}$ can be described by a reciprocal lattice vector $\mathbf{K} = 2\pi/P\hat{\boldsymbol{\xi}}$. The axes $\boldsymbol{\xi}$ and $\boldsymbol{\zeta}$ will be used as the local coordinate system of the grating, opposed to the global coordinates $\mathbf{x}$ and $\mathbf{y}$ of the experiment. Different diffraction orders in such a grating, i.e., modes shifted by multiples of $\mathbf{K}$, can intersect and couple to each other to form new bands. This coupling can open gaps in the dispersion relation $\omega(\mathbf{k})$. For monochromatic experiments like the ones which were performed for the work presented

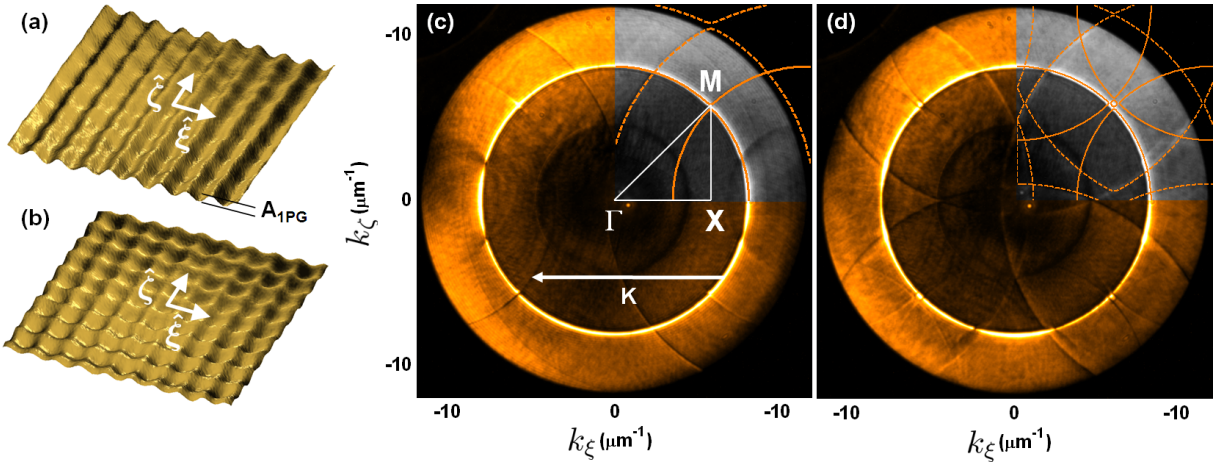

Figure 5.1.: (a)+(b) Atomic Force Microscopy images (5×5 µm^2) of 1PG and 2PG with a modulation amplitude of 25 nm and periods of $760/\sqrt{2}$ nm and $750/\sqrt{2}$ nm, respectively. The gratings were fabricated by FIB lithography on indium-titanium oxide (ITO) coated glass coverslips and subsequent deposition of a 50 nm Au layer by electron-beam evaporation. - (c)+(d) LR Fourier space micrographs, acquired with the setup presented in chapter 3.2.2. Calculated band structures were superimposed in the first quadrants for the Au-air (solid line) and Au-ITO interfaces (dashed line), using fitted modulation depth of $\gamma_{1\mathrm{PG}} = 0.055$ and $\gamma_{2\mathrm{PG}} = 0.020$ for the 1PG and 2PG, respectively. A representation of the grating vector $\mathbf{K}$ for the 1D grating is depicted as a white arrow.

here, the dispersion relation $\omega(\mathbf{k})$ can be visualized by so called isofrequency surfaces, plotting the Bloch modes for all $\mathbf{k}$ at a fixed ω_0. Each mode has a particular propagation direction, which is defined by its group velocity $\mathbf{v}_\mathrm{g}(\mathbf{k}) = \partial_\mathbf{k}\omega(\mathbf{k})$. It thus follows that $\mathbf{v}_\mathrm{g}$ is always perpendicular to the isofrequency surfaces, and oriented towards the direction of isofrequency surface evolution for increasing frequency [162, 172].

We analyzed SP Bloch modes in 1D and 2D gratings like the ones depicted in Fig. 5.1(a+b). To facilitate structuring of smooth gratings in thin metal films, a modified FIB lithography process had to be implemented: sinusoidal profiles were engraved by FIB in indium-tin oxide (ITO) films on glass cover slips (SPI 6468AB). As large gratings had to be produced, beam currents of 5 nA with ion beam spot sizes of around 100 nm were necessary to reduce spatial discretization errors during fabrication. Au films of 50 nm thickness were subsequently deposited on top of the structured ITO by electron-beam evaporation.

For 2D surface waves in such gratings, like SPs, the isofrequency surfaces of Bloch modes reduce to so called isofrequency contour diagrams (IFD). Experimental and calculated IFDs of the singly (1PG) and doubly periodic gratings (2PG) were acquired. The period was chosen close to $P_\mathrm{Bragg} = \lambda_\mathrm{SP}/\sqrt{2}$. This corresponds to Bragg reflection at 45° incidence, derived from the Bragg condition $2\mathbf{K} \cdot \mathbf{k}_\mathrm{SP,\,in} = |\mathbf{K}|^2$ for an incident in-plane wavevector $\mathbf{k}_\mathrm{SP,\,in}$. Experimental IFDs were acquired by illuminating a central nanohole defect in extended 1PG and 2PG gratings with a focused $\lambda = 785$ nm laser spot to launch all possible Bloch modes in the grating, and subsequent LR imaging of these modes in reciprocal space. To suppress direct transmission by the defect and to excite modes in all directions, crossed circular polarizers have been placed in the illumination and imaging beam paths.

Theoretical modeling of IFDs was performed by solving a planar wave equation [173] as

$$\det\left(\nabla_\mathbf{r}^2 - \epsilon_\mathrm{1PG}(\mathbf{r},\omega)\omega^2/c^2\right) = 0, \tag{5.1}$$

with the SP permittivity modeled as

$$\frac{\epsilon_\mathrm{1PG}(\mathbf{r},\omega)}{\epsilon_\mathrm{SP}} = 1 + \gamma\cos\left(\frac{2\pi}{P}\xi\right). \tag{5.2}$$

The modulation amplitude parameter γ is extracted from least-square fitting of the plasmonic bandgap width K_gap to experimental IFDs. For two-dimensional gratings the SP permittivity was analogously modeled as

$$\frac{\epsilon_\mathrm{2PG}(\mathbf{r},\omega)}{\epsilon_\mathrm{SP}} = \left(1 + \gamma\cos\left(\frac{2\pi}{P}\xi\right)\right)\left(1 + \gamma\cos\left(\frac{2\pi}{P}\zeta\right)\right). \tag{5.3}$$

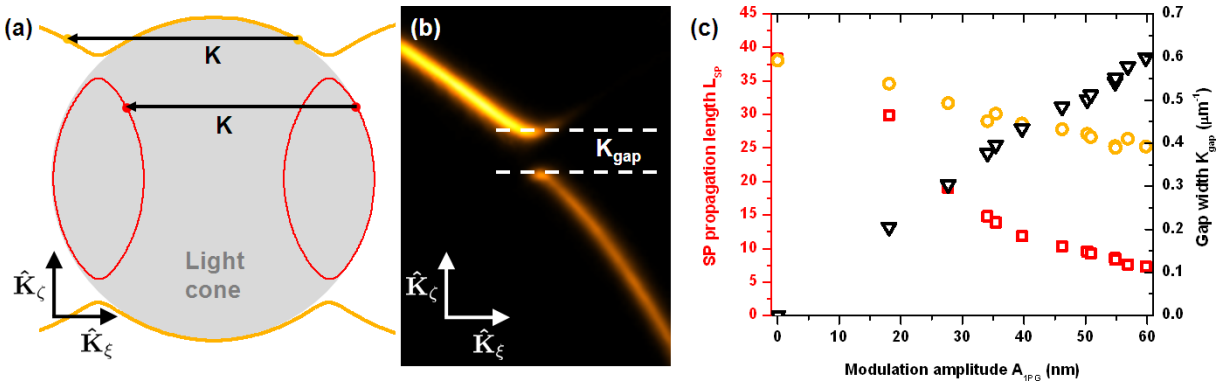

Figure 5.2.: Bandgap widths and SP decay lengths in plasmonic gratings - (a) Sketch of the IFD of a plasmonic crystal. Modes for which $|\mathbf{k}_O + n\mathbf{K}| > k_0$ does not hold for all n (red) can couple to modes inside the light cone (gray). - (b) Experimental LR reciprocal space image around the M point on a 75×75 µm sized grating of period $P_{1PG} = 760/\sqrt{2}$ nm and a modulation amplitude $A_{1PG} = 40$ nm in an 80 nm gold film. - (c) Plasmonic bandgap widths K_{gap} (black triangles) and SP propagation lengths L_{SP} on the inner (red squares) and outer (orange circles) branches as a function of the grating modulation amplitude A_{1PG}. Modulation amplitudes have been extracted from sinusoidal fitting of profiles extracted by atomic forces microscopy.

Results of experimental and theoretical IFD determination are shown in Fig. 5.1(c) and (d). Bands on the front Au-air (solid lines) as well as on the back Au-ITO interface (dashed) are visible. In the following exclusively modes on the metal-air interface will be considered. For the choice of $P = P_{Bragg}$, band gaps open up around the M point. The influence of these gaps on SP propagation will be the core of the work presented hereinafter.

Note that by introducing only λ_{SP}, γ and P as parameters, already a quite accurate theoretical modeling of the Bloch mode locations could be achieved. However, the model does not take into account dissipation, and thus lacks to determine Bloch mode loss characteristics.

Analyzing the modes in one-dimensional gratings in more detail, two regimes can be identified (Fig. 5.2(a)): For modes with a wavevector $\mathbf{k}_O$ on the outer (orange) branch, the condition

$$|\mathbf{k}_O + n\mathbf{K}| > k_0 \tag{5.4}$$

is fulfilled for all $n \in \mathbb{Z}$. Thus these modes are located outside the lightcone in air. For modes on the inner (red) branch, however, this condition is not fulfilled for all n. They are therefore expected to show significantly reduced propagation lengths, as the grating serves as an efficient decoupler to free space modes in the dielectric halfspace.

In the following the influence of the grating amplitude A_{1PG} on the propagation length

in these two regimes, as well as on the width of the bandgap K_{gap} will be discussed. Extended gratings were fabricated with modulation amplitudes A_{1PG} up to 60 nm. To access the bandgap region of the bandstructure, 300 nm wide nanogroove sources were milled inside the grating orthogonal to the M direction. By focusing a $\lambda_0 = 782$ nm laser beam on the slit, SPs in the M direction were launched. A sample Fourier space image is depicted in Fig. 5.2(b). Bandgap widths were extracted from these reciprocal space LR images by Gaussian fitting of the resonance curves and determination of $K_{\mathrm{gap}} = \min(\mathbf{k}_{\mathrm{O}} \cdot \hat{\mathbf{K}}_{\zeta}) - \max(\mathbf{k}_{\mathrm{I}} \cdot \hat{\mathbf{K}}_{\zeta})$.

SP propagation lengths for modes on the inner and outer mode branch were determined subsequently. To launch beams consisting exclusively of one or the other type of modes, slit sources tilted at $+25°$ and $-20°$ were fabricated. The tilted slits were illuminated as above, and real space high dynamic range LR images were acquired. The slope $-2k''_{\mathrm{1PG}}$ of linear fits of logarithmic SP intensity, integrated over the beam width, yielded the SP propagation lengths as $L_{\mathrm{SP}} = 1/2k''_{\mathrm{1PG}}$.

Results for K_{gap} and L_{SP} as a function of A_{1PG} are shown in Fig. 5.2(c). A general reduction of the SP propagation length with grating amplitude is observed. While this reduction is below 35% for SP modes on the outer branch, a reduction up to 80% was observed on the inner branch. This agrees qualitatively well with our expectations of additional loss induced by coupling to the light cone of modes on the inner branch.

The bandgap width is a genuine grating effect, and is thus expected to increase with the modulation amplitude. The experimental results confirm this, and reveal an approximately linear relation. Similar results have been reported for dielectric and plasmonic Bragg mirrors [174].

Subsequently presented experiments demonstrating the effect of anisotropic band-structures on SP beams propagating inside metal gratings will, on the one hand, depend on the strength of such anisotropy, but, on the other hand, require reasonable SP propagation lengths to be practically interesting. This trade-off has to be accounted for by choosing moderate modulation amplitudes. Moreover, it will be crucial to work with modes on the low-loss, outer IFD branch.

5.2. Surface Plasmon Bragg Mirrors

Before concentrating on propagating modes inside plasmonic crystal gratings and the effect of local anisotropies of the IFD around the bandgap on these modes, we first studied one of the best known effects associated with bandgap structures: Bragg reflection. This will also allow a practical estimate on the functionality of the fabricated sinusoidal metal gratings for plasmonic beam manipulation.

SP Bragg mirrors based on dielectric structures have first been presented by Ditlbacher an coworkers [57], and have been studied in further detail recently [174]. Effects of grating amplitudes on the reflectivity have been analyzed in studies focusing on Bragg mirrors made from metal grooves and ridges [62, 63, 175]. The variation of reflectivity and transmission for 45° incidence has been measured as a function of the number and height of metal ridges and grooves. A change of the angular acceptance of such mirrors with incident angle was

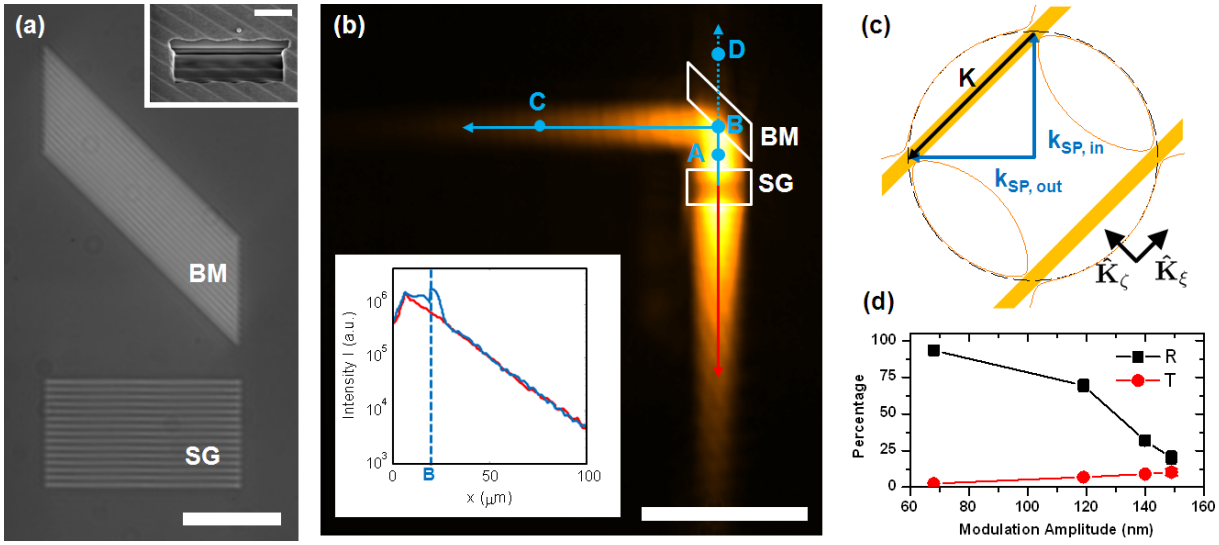

Figure 5.3.: SP Bragg mirrors - (a) Optical micrograph of a Bragg mirror (BM, $P_{\mathrm{BM}} = 760/\sqrt{2}$ nm, amplitude 68 nm) and a source grating (SG, $P_{\mathrm{SG}} = 760$ nm) fabricated in a $h = 45$ nm thick Au film. Inset: SEM cross-section of the metallic mirror geometry, showing substrate, ITO and metal layers. The scale bars correspond to 10 µm (main) and 1 µm (inset). - (b) LR micrograph of SPs launched by focusing a $\lambda_0 = 785$ nm laser diode on the SG. The upwards propagating SP beam is reflected by the BM. The scale bar corresponds to 50 µm. Inset: Exponential decay of SP intensity, integrated over the beam width. - (c) Fourier space operating scheme of the BM. SPs incident with $\mathbf{k}_{\mathrm{SP,in}}$ cannot couple to modes inside the grating along the interface normal. Thus SPs with $\mathbf{k}_{\mathrm{SP,out}}$ are excited, differing by one grating vector $\mathbf{K}$. For the chosen interface, the SP bandgap is shaded orange. - (d) Reflectivity R and transmittance T extracted from LR images as a function of the grating modulation amplitude.

also observed. Both effect could be attributed to changes of the width of the plasmonic bandgap.

The principle of such Bragg mirrors with an interface along $\hat{\boldsymbol{\zeta}}$, i.e., normal to the reciprocal X direction, can be visualized in a Fourier space picture as illustrated in Fig. 5.3(c). Inside the grating a bandgap for SPs opens up, as discussed in the previous section. SPs incident on the mirror can couple along the interface normal to modes on the grating or on the flat film. If $\mathbf{k}_{\mathrm{SP,in}}$ lying inside the gap region are chosen, coupling to modes in the grating is forbidden. Therefore coupling along one grating vector $\mathbf{K}$ to $\mathbf{k}_{\mathrm{SP,out}}$ occurs, corresponding to reflection at 90°. Modes outside of the gap region can propagate through the grating practically unperturbed.

We carried out experiments as a preliminary study for the following steering analysis, proving the basic functionality of sinusoidal thin films gratings. An example is depicted in Fig. 5.3(a-b). SPs are launched by focusing a $\lambda_0 = 785$ nm laser diode on a source grating (SG) of period $P_{\mathrm{SG}} = 760$ nm. The numerical aperture of the focusing lens was reduced to NA = 0.045 by placing a variable iris in front of the illumination objective. This allowed launching SP beams with a divergence δk_x smaller than the gap-width, thus yielding very high reflectivities. The Bragg mirror (BM) was designed for 45° incidence with 15 grooves of a period of $P_{\mathrm{BM}} = 760/\sqrt{2}$ nm. Reflectivity and transmittance were determined for mirrors of varying modulation amplitude as

$$R = \frac{I_{\mathrm{C}}}{I_{\mathrm{A}}} e^{k''_{\mathrm{SP}}\overline{ABC}} \text{ and } T = \frac{I_{\mathrm{D}}}{I_{\mathrm{A}}} e^{k''_{\mathrm{SP}}\overline{AD}}, \tag{5.5}$$

respectively. Intensities I_{x} were taken from lateral signal integration over the beam width. The exponential term corrects the intensity ratio for the exponential decay of the SP, which was extracted as $k''_{\mathrm{SP}} = 0.0317$ µm^{-1} by linear regression of the intensity decay measurements shown in Fig. 5.3(b). The calculation was averaged over 10, 300 and 200 choices of the planes A, C, and D, respectively. Results are plotted in Fig. 5.3(d).

A maximum reflectivity of $R = 93 \pm 1\%$ was obtained for a modulation amplitude of 68 nm. For larger amplitudes the reflectivity begins to decrease, at only minimal increase of the transmittance. The associated increase in loss $1 - R - T$ can be attributed to increased out-of-plane scattering at modulation amplitudes above ~ 100 nm. This is in good agreement with the results observed in [62]. It could thus be confirmed that sinusoidal metal gratings could serve as highly efficient Bragg mirrors.

5.3. Steering of Surface Plasmons in 1D Gratings

For the use of plasmonic crystals as Bragg mirrors, it was possible to limit the discussion to two regions of k_{in}: modes in the bandgap on the one hand, leading to Bragg reflected beams, and modes outside the gap, which can propagate practically unperturbed inside the grating. In the following the transition region between these two regimes will be discussed. The bending of the bandstructure in this region bears strong similarity to these observed in classic dielectric photonic crystal slabs [164]. It is thus expected to provide similar beam steering capacities, which was experimentally verified by the work presented in this section.

The nanostructure setup is depicted in Fig. 5.4(a). SPs are launched by illuminating a sinusoidal source grating (SG) with a $\lambda = 785$ nm pigtailed laser diode polarized parallel to the source grating vector $\mathbf{K}_{\mathrm{s}}$. Excited SPs are incident on a 1PG with $P \approx P_{\mathrm{Bragg}}$, having $\mathbf{K}$ oriented at 45° with respect to the structure interface. At this interface the grating is tapered over a 2 µm long transition region to reduce typical SP scattering losses (see chapter 4). A moderate modulation amplitude of 25 nm was chosen to ensure significant grating effects at reasonable SP propagation lengths inside the grating. SP beam propagation is monitored with the standard LR microscopy configuration discussed in section 3.2.2, using an NA = 1.49 immersion objective.

To probe the fine structure of the SP dispersion and thus to observe SP beam steering, specific modes inside the grating, defined by their in-plane wavevector $\mathbf{k}$, have to be excited

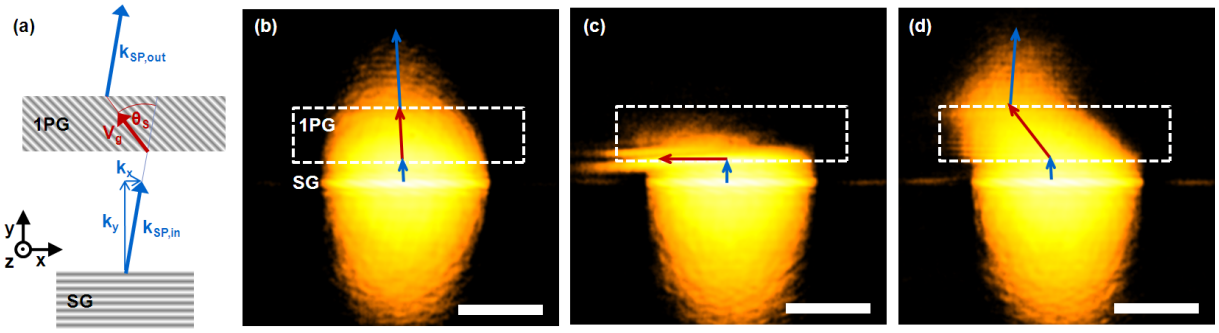

Figure 5.4.: Real space experiments - (a) Sketch of the experimental setup with source grating SG (100×10.6 µm^2, $P = 760$ nm) separated ~ 3.7 µm from a 1PG (150×32 µm^2, $P = 760/\sqrt{2}$ nm). The incident SP wavevector $\mathbf{k}_{\mathrm{SP,\,in}}$ as well as the group velocity $\mathbf{v}_{\mathrm{g}}$ and the steering angle of SPs θ_{S} inside the grating are shown. - (b-d) LR real space images of SPs launched by the SG with varying in-plane component $k_x = -0.53, +0.05, +0.19$ µm^{-1} of $\mathbf{k}_{\mathrm{SP}}$. Scale bars correspond to 50 µm.

in a controllable way. As the component $k_x = \mathbf{k}_{\mathrm{SP,\,in}} \cdot \hat{\mathbf{x}}$ is conserved at the 1PG interface (see chapter 4.2), precise excitation of $\mathbf{k}$ is equivalent to a low transverse divergence δk_x of the incident SP beam.

Exciting SPs with a standard NA = 0.13 objective leads to an already small angular spread of $\delta k_x = 2.1\ \mu\mathrm{m}^{-1}$ (see chapter 2.2.1), which is, however, large compared to typically observed SP bandgap widths. The divergence was reduced by limiting the effective NA of this objective with a 600 µm wide translatable slit placed in front of the objective's rear aperture (see Fig. 3.5). According to space-momentum uncertainty, this leads to an excitation spot with a wide sinc profile in $\hat{\mathbf{x}}$ (see Fig. 5.4(b-d)), and therefore also requires the use of equivalently large SGs. An SG size of $100 \times 10.6\ \mu\mathrm{m}^2$ was chosen, the SP divergence could hence be reduced to $\delta k_x = 0.1\ \mu\mathrm{m}^{-1}$. In addition, simple translation of the slit also facilitated convenient scanning of different k_x values.

Using this capability to excite SPs with different k_x, three typical regimes were observed (Fig. 5.4(b-d)): Far off normal incidence and thus also off the Bragg condition ($k_x = -0.53\ \mu\mathrm{m}^{-1}$), SPs can propagate through the grating almost unperturbed. At normal incidence ($k_x = 0.05\ \mu\mathrm{m}^{-1}$), the structure acts just like a 90° Bragg mirror. Particularly interesting, however, is the behavior between these two regimes (e.g. $k_x = 0.05\ \mu\mathrm{m}^{-1}$), where anomalous refraction was observed. It will be shown later that this corresponds to negative refraction of SP beams.

The wavevector component k_x was systematically varied in a range of $\pm 0.8\ \mu\mathrm{m}^{-1}$, corresponding to incident angles of ±5.6°. SP beam deflection angles $\theta_{\mathrm{S}}^{\mathrm{exp}}$ were extracted by Gaussian fitting of the beam waist exiting the 1PG. Results are depicted in Fig. 5.5(a) (filled squares). As expected, SPs at off-resonance angles remain unperturbed. Around the Bragg condition, however, SPs can be steered to a range of angles of more than 40° solely by varying the incident angle in a range of less than 2.5°. This corresponds to a direct observation of a plasmonic superprism effect.

The results are in good agreement with theoretical and experimental predictions from IFD analysis. Recalling that the SP group velocity is always directed orthogonal to the IFD, which is schematically shown in Fig. 5.5(b), the SP steering angle could be calculated as

$$\theta_{\mathrm{S}} = \arcsin\left(\hat{\mathbf{z}} \cdot \frac{\mathbf{v}_{\mathrm{g}} \times \mathbf{k}_{\mathrm{SP,in}}}{|\mathbf{v}_{\mathrm{g}}||\mathbf{k}_{\mathrm{SP,in}}|}\right). \tag{5.6}$$

The resulting steering angles are depicted in Fig. 5.5(a) (black curves) and are in good agreement with the results from real space experiments.

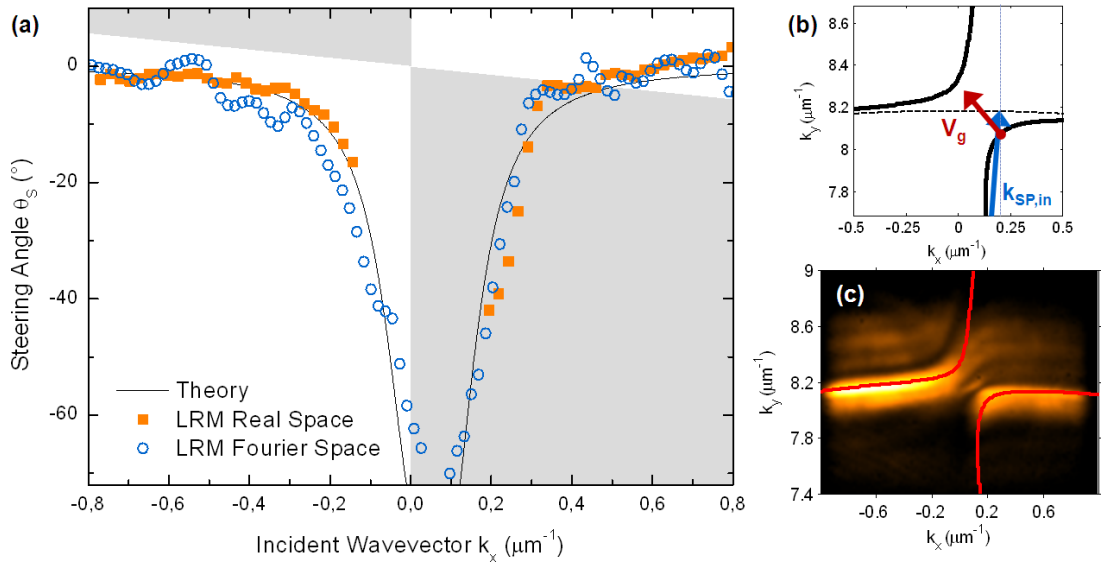

Figure 5.5.: (a) Dependence of the SP steering angle θ_S on the incident SP wavevector component k_x, determined from LR real space (orange squares) and Fourier space (blue circles) measurements. Values extracted from calculated IFDs are given by the black line. - (b) Calculated IFD (detail of Fig. 5.1(c), white box). Steering results from coupling of incident SPs to Bloch modes under conservation of k_x, i.e., along the direction of the dashed line. The group velocity $\mathbf{v}_g = \boldsymbol{\nabla}\omega(\mathbf{k})$ of the Bloch mode is directed normal to the IFD. - (c) Experimental IFD detail around the bandgap region from illumination of the SG with a focused beam by removing the slit. Calculated bands are superimposed as red lines.

Steering angles were also extracted from experimentally acquired reciprocal space LR images. An example IFD is shown in Fig. 5.5(c). The group velocity direction is evaluated by Gaussian fitting along k_y for each pixel column corresponding to a k_x, and subsequent local linear regression of the peak centers to extract normals to the local slope of the curve. The results (open circles) compare again well to the calculated results, as well as to the results from real space experiments.

Besides this amplified SP steering, it is moreover observed that some points on the right side of the resonance in Fig. 5.5(a) lie in the gray shaded region. This region, however, correspond to opposite signs of k_x and $v_{g,x} = \mathbf{v}_g \cdot \hat{\mathbf{x}}$, and thus to genuine negative refraction of SP beams. This anomalous refraction is a solely diffractive process relying on only positive permittivities. It therefore contrasts with negative refraction based on negative indices [55, 176–178].

5.4. Steering in 2D Gratings

So far only steering in singly periodic structures was studied. In the following this will be extended to two-dimensional gratings, characterized by a reciprocal lattice with the basis $\mathbf{K}_\xi = 2\pi/P\hat{\boldsymbol{\xi}}$ and $\mathbf{K}_\zeta = 2\pi/P\hat{\boldsymbol{\zeta}}$. The IFD of such a structure is depicted in Fig. 5.1(d).

Gratings with periods slightly above ($P = 790/\sqrt{2}$ nm $> P_{\mathrm{Bragg}}$) and below ($P = 750/\sqrt{2}$ nm $< P_{\mathrm{Bragg}}$) the Bragg period were fabricated, with the interface oriented again in the M direction, and with dimensions and source gratings identical to the ones discussed for 1PGs. Interesting features are observed for SP beams incident with $k_x \approx 0$. This region is magnified in Fig. 5.6(a+b): for both periods an isolated feature appears in the bandstructure, however the curvatures of both features are inverted.

To reveal the consequences of this inversion, similar real space and Fourier space steering experiments as for 1PGs were performed on both gratings. The results are depicted in Fig. 5.6. For both periods and in contrast to the results for 1PGs, steering to positive as well as to negative θ_{S} was observed. For $P > P_{\mathrm{Bragg}}$ this always corresponds to positive refraction. However, for $P < P_{\mathrm{Bragg}}$ continuous negative refraction in a range of

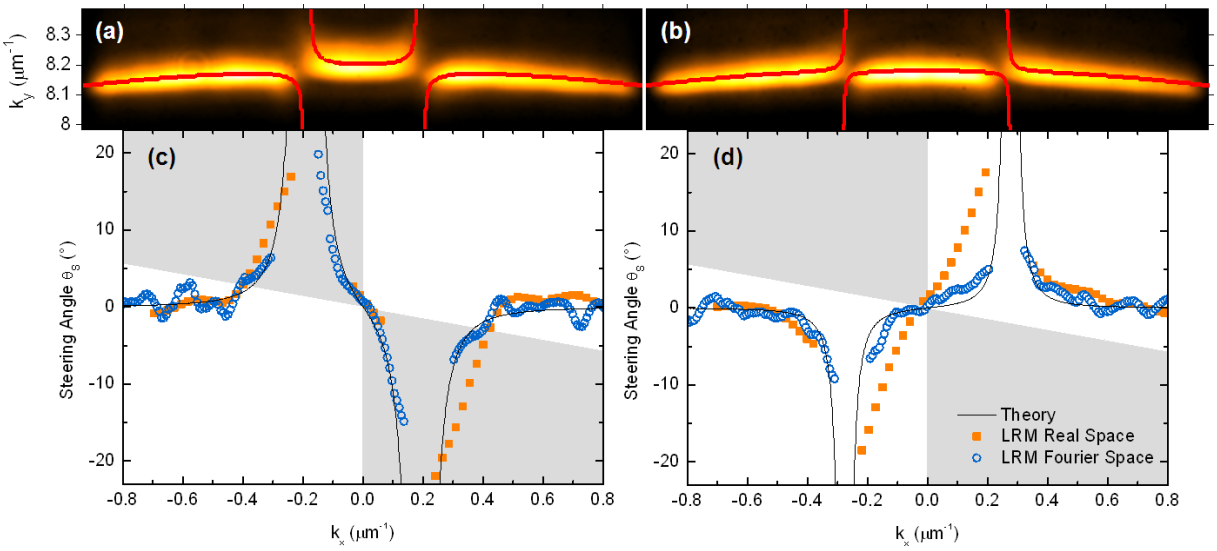

Figure 5.6.: 2PGs with periods $P = 750/\sqrt{2}$ nm $< P_{\mathrm{Bragg}}$ (left) and $P = 790/\sqrt{2}$ nm $> P_{\mathrm{Bragg}}$ (right) - (a+b) Detail of the IFD of 2PGs around the bandgap region from LR images. Calculated IFDs are superimposed with modulation depths $\gamma = 0.020$ and $\gamma = 0.010$, respectively. - (c+d) Steering angle θ_{S} as a function of k_x, extracted from real and reciprocal space LR images as well as calculations. Especially for $P = 790/\sqrt{2}$ nm a deviation of real space and Fourier space results is observed, which can be explained by the inherent convolution of the real space SPs with the still finite $\delta k_x = 0.1$ µm^{-1}

$k_x = \pm 0.4$ µm^{-1} to positive and negative angles θ_S was achieved, an effect know from dielectric photonic crystals as "all-angle" negative refraction [168]. These modes also fulfill the condition $|\mathbf{k} + n\mathbf{K}_\xi + m\mathbf{K}_\zeta| > k_0$ for all $n, m \in \mathbb{Z}$, i.e., they cannot couple to free-space modes and thus suffer low propagation loss. Similar to their applications in dielectric waveguides, these gratings are expected to have further impact also on SP focusing or imaging [166, 169].

5.5. Self-Collimation of Plasmon Beams

It has been discussed how the anisotropy of IFDs in plasmonic crystals can lead to SP beam steering and negative refraction. Similar bandstructure anisotropy has also been exploited to achieve self-collimation of beams propagating in two-dimensional dielectric photonic crystals [179–181]. It will be shown in the following how such effects can be implemented in the field of plasmonics to generate weakly diffracting SP beams.

Just like optical beams in free-space, SP beams of finite width experience diffraction, as observed from the spreading of beam profiles with propagation distance, e.g., in Fig. 2.6. This spreading is inversely proportional to the minimum beam width, and can be attributed

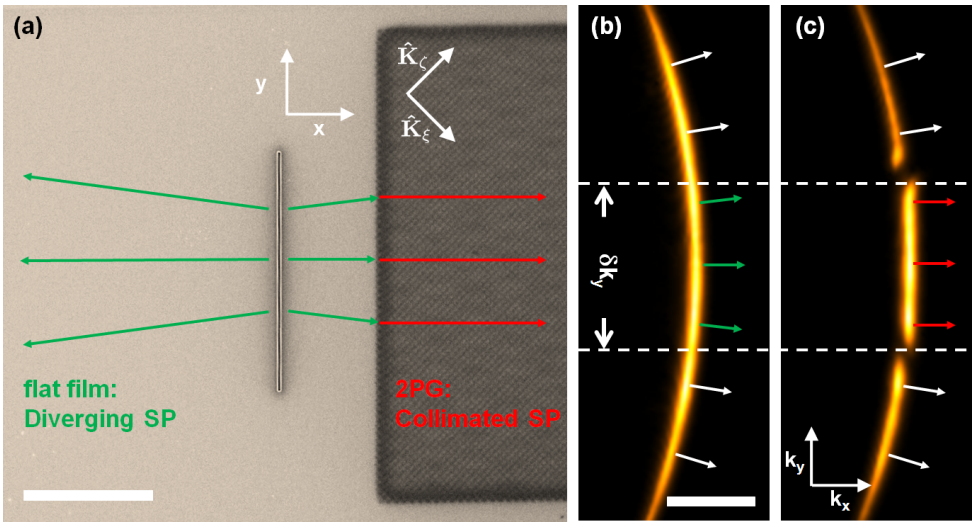

Figure 5.7.: Self-collimation in plasmonic crystals: (a) SEM image of the groove source and the 2PG structure. The scale bar corresponds to 10 µm. - (b-c) IFDs on a flat film and inside the 2PG, respectively. Directions of the local group velocity $\mathbf{v}_g$ for SPs are shown as small arrows. While on a flat film $\mathbf{v}_g$ is diverging for different k_y, in the 2PG a flat region appears around the M point leading to parallel group velocities. The scale bar corresponds to 1 µm^{-1}.

to the involved distribution of transverse wavevector components. It is problematic in particular for optical interconnecting applications, in which an increase in beam width can lead to detrimental signal loss if device dimensions are not matched accordingly. Several solutions for non-diffracting beams in three-dimensional space, such as Bessel [182], Mathieu [183] and Airy beams [184] are known, all requiring ideally infinite energy content. A similar solution has also been derived for the planar case of SPs, showing self-healing properties on curved trajectories [185]. Recently, such SP Airy beams have also been implemented experimentally [46, 48, 69].

We here want to resort to a different approach, relying on flattening of IFDs inside plasmonic crystals. As discussed in section 5.4, the IFDs of 2PGs show inverted positive curvature around the M point for periods just below the Bragg condition. For even smaller periods $P \ll P_{\mathrm{Bragg}}$, however, the bandgap regions are located far off this point, yielding nearly unaffected IFDs around M with the original curvature of the SP circle. It therefore appears possible to find an intermediate regime where an approximately flat IFD is achieved.

Gratings were designed for such a purpose by careful choice of the period $P = 680/\sqrt{2}$ nm and for an appropriate modulation amplitude $A_{\mathrm{2PG}} = 22$ nm in an 80 nm thick gold film. Compared to SPs on the flat film with a circular IFD and thus diverging group velocities (Fig. 5.7(b)), a flat IFD region appears inside the 2PG around the M-point, $\Delta k_y \approx 1.9$ µm^{-1} wide (Fig. 5.7(c)). SP were excited by focusing a $\lambda_0 = 782$ nm laser diode on a nanogroove source in front of the 2PG. SPs were launched with a divergence δk_y corresponding to the numerical aperture of the incident objective. To excite only SPs inside the flattened region, this δk_y of the launched SP beam had to be carefully adjusted. An iris aperture was used for this purpose in front of the illumination objective, similar to the method discussed for steering of SPs in section 5.3.

Resulting SPs in the flat region and on the 2PG were imaged by LR microscopy and are depicted in Fig. 5.8(a-b). To again prevent additional scattering loss inside the grating, smooth gratings with tapered transitions were designed as discussed above. Moreover, as $P < P_{\mathrm{Bragg}}$ was chosen, all modes inside the flat region fulfill the condition $|\mathbf{k} + n\mathbf{K}_\xi + m\mathbf{K}_\zeta| > k_0$, forbidding resonant scattering loss to the air light-cone. Propagation lengths of SPs on flat films and inside the 2PG were evaluated by linear fitting of logarithmic intensities in Fig. 5.8(c). Only weakly decreased propagation lengths inside the grating of $L_{\mathrm{2PG}} = 32.2$ µm were revealed compared to measured $L_{\mathrm{SP}} = 38.4$ µm on the flat film, the latter value comparing well to the theoretically expected $L_{\mathrm{SP}} = 38.5$ µm.

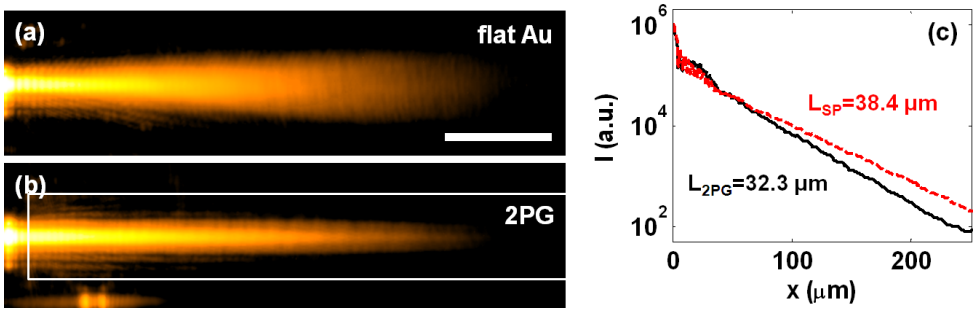

Figure 5.8.: (a-b) Real space high dynamic-range LR images of SPs on a flat film and inside the 2PG, respectively. The 2PG is marked by the white box, the scale bar corresponds to 50 µm. - (c) SP intensity on a flat film (black) and on a 2PG (red) in logarithmic scale as a function of propagation distance, integrated at each x along the $\hat{\mathbf{y}}$-direction.

In order to evaluate the improvement in divergence, acquired LR images were normalized to the local maximum intensity at every x, and the evolution of the SP beam width $w(x)$ with propagation distance was extracted. Results are depicted in Fig. 5.9, together with transverse beams profiles taken every 50 µm. The use of high dynamic-range imaging as discussed in section 3.2.2 turned out crucial here for the observation of SPs over multiple decay lengths, as required for evaluating the spreading of the excited beam. In addition, Huygens-Fresnel simulations of the in-plane SP intensity $I_{||} \propto |\mathbf{E}_{\mathrm{SP}} \cdot \hat{\mathbf{x}}|^2 + |\mathbf{E}_{\mathrm{SP}} \cdot \hat{\mathbf{y}}|^2$ have been carried out according to the model presented in section 2.2.1.

For beams propagating on a flat interface, a divergence of $\Theta_{\mathrm{flat}} = 6.31°$ was observed, evaluated as $\Theta = \arctan(w(x)/2x)$ for large x. Note that the evolution of this beam actually deviates slightly from that of a mere Gaussian beam, which is explained by the fact that an Airy-like excitation profile had been chosen. For beams inside the 2PG, however, the k_x component is assumed to equal a constant β. Hence using $\mathbf{E}_{\mathrm{SP}}(k_x, k_y) = \mathbf{E}_{\mathrm{SP}}(k_y)\delta(k_x - \beta)$, Fourier decomposition $\mathbf{E}_{\mathrm{SP}}(x, y) = \iint dk_x dk_y \mathbf{E}_{\mathrm{SP}}(k_x, k_y) e^{i(k_x x + k_y y)}$ of the SP field leads to a predicted field distribution of $\mathbf{E}_{\mathrm{SP}}(x, y) = e^{i\beta x} \int dk_y \mathbf{E}_{\mathrm{SP}}(k_y) e^{ik_y y} = e^{i\beta x}\mathbf{E}_{\mathrm{SP}}(0, y)$ [37]. In other words, the beam profile is expected to be conserved for propagation along $\hat{\mathbf{x}}$. Experimentally, a divergence of $\Theta_{\mathrm{2PG}} = 2.85°$ is measured from the presented images, corresponding to a 55% improvement over flat films. The residual non-zero divergence of the beam is attributed to imperfect flattening of the SP bands, which could potentially be corrected by further optimization of the 2PG bandstructure.

It was discussed in section 2.2.1 that the phase of different plane wave components can be modulated by a shift of the focal plane of the incident objective. Such a shift δz was observed to lead to equivalent in-plane shifts δx of the SP focal distance from a slit source, as shown in Fig. 2.6(e). The effect is again visualized in Fig. 5.9(c) for a defocused

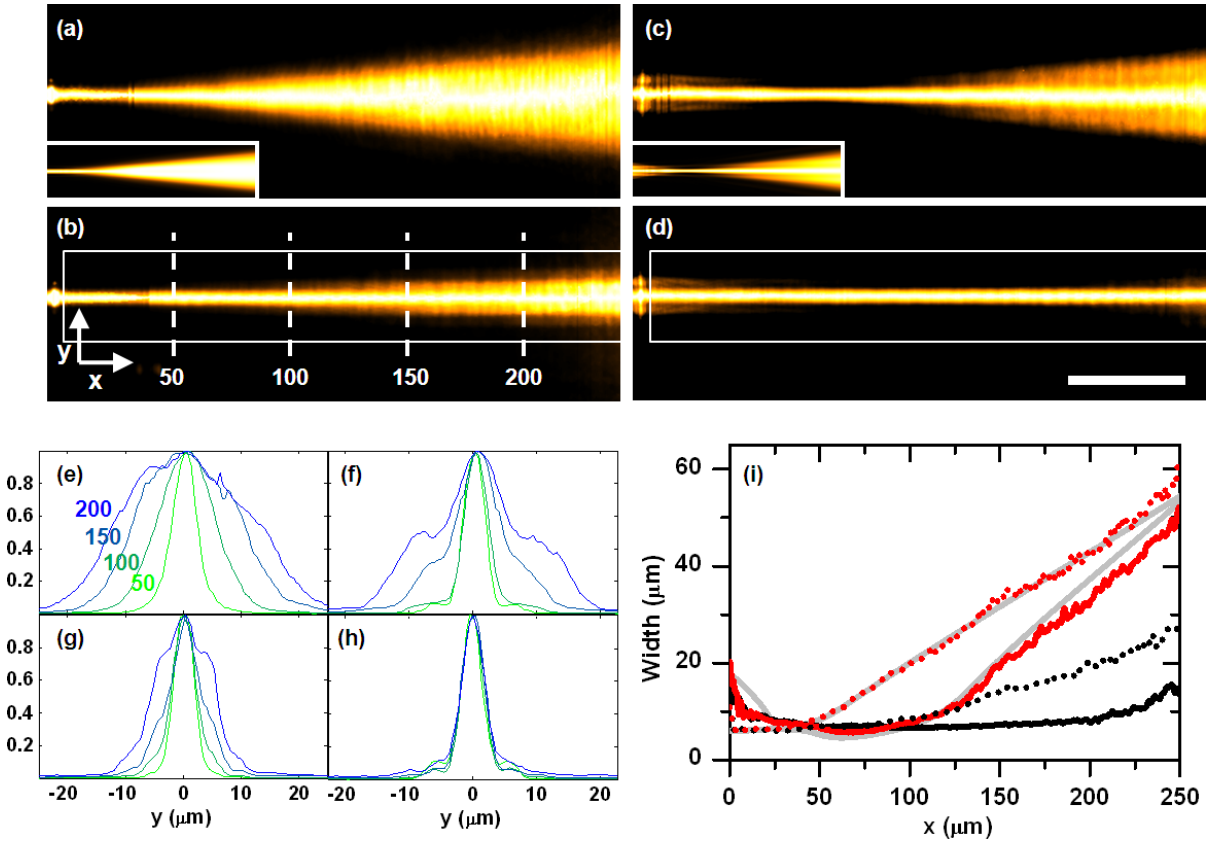

Figure 5.9.: (a-d) LR micrographs, from excitation by a focused (a,b) and slightly out-of-focus (c,d) laser spot on a flat film (a,c) and on a 2PG (b,d). Results from Huygens-Fresnel simulations are shown in the insets. The images are normalized to the local maximum intensity for every x, and the scale bar corresponds to 50 µm. (e-h) Cross sections along $\hat{\mathbf{y}}$ of the beams in (a-d), respectively, at 50 to 200 µm distance from the source. (i) Evolution of the SP beam width with propagation distance x for focused (dotted) and defocused (solid lines) excitation on flat films (red) and inside the 2PG (black). Results from Huygens-Fresnel simulations are shown as gray lines. The widths $w(x)$ were extracted from Gaussian fitting of the normalized images along $\hat{\mathbf{y}}$.

excitation spot from the numerical aperture chosen here, illuminating a nanogroove. Using the same illumination conditions, a significant enhancement of the distance of confined beam propagation was found inside the 2PG (Fig. 5.9(d)). Self-collimated propagation over 200 µm distance was observed, i.e., over six SP decay lengths.

To summarize, self-collimating SP beams can be generated in 2PGs. The self-collimation effect has been shown to rely on flat IFDs achieved in such structures for appropriate grating parameters. Diffraction-free propagation has been observed over several SP propagation lengths, with only small increases in SP scattering loss. Moreover, in 2PGs, arbitrary transverse position as well as profiles can be imprinted on the SP beam, which is

different from plasmonic waveguides. For these reasons, such structures appear promising as candidates for reconfigurable plasmonic optical interconnects.

5.6. Conclusions

In this chapter the propagation of SP beams in 1D and 2D plasmonic crystals has been discussed. Bragg reflection as well as large beam steering in singly periodic gratings has been observed including negative refraction without the need of a negative refractive index. Both effects could be explained by careful analysis of IFDs for Bloch modes in the structures. The study has been extended to doubly periodic gratings, revealing all-angle negative refraction of SP beams. By variation of the grating period, flat IFDs in such two-dimensional plasmonic crystals have been designed leading to self-collimating SP beams.

It will be shown in chapter 6 how the steering capabilities of plasmonic gratings can be applied for optical manipulation of metallic nanoparticles. The observed anisotropy of the bandstructure has also great potential for refractive index sensing, promising large sensitivity improvements over conventional geometries. A plasmonic refractive index sensor based on this effect will be discussed in detail in chapter 8.

6 Routing Metal Nanoparticles by Negative Refraction

In the previous chapter the anisotropy of plasmonic bandstructures in metal gratings was observed to lead to steering, negative refraction and self collimation of surface plasmon beams. This novel degree of freedom will be applied in the following to achieve all-optical control over metal nanoparticle motion on such gratings, as visualized in Fig. 6.1.

First a discussion of the optical forces on metal nanoparticles will be given. Then experiments on routing these particles by negative refraction of SPs will be presented. A prism coupling setup will be introduced which had to be developed for the purpose of this study. The chapter will close with a statistical analysis of the acquired data, demonstrating nanoparticle routing based on a plasmonic superprism effect. The results of this chapter have been published in Nano Letters in 2012 [4] (© 2012 American Chemical Society).

6.1. Forces on Metal Nanoparticles

Since the first demonstration of optical trapping [186], micromanipulation of particles and atoms by light induced forces has found widespread application from fundamental physics to chemistry and life sciences. One of the most used techniques are three-dimensional optical tweezers based on gradient forces in a tightly focused single optical beam [187]. However, trapping of particles with subwavelength size is difficult to achieve using such methods.

Surface plasmon based techniques have, among others [188], contributed to overcoming this limitation. On the one hand, localized surface plasmon resonances have proven to provide well "parallelizable" optical trapping in the plasmonic near-field at subwavelength lengthscales [189, 190]. On the other hand, it has also been demonstrated recently how delocalized plasmon waves in metal gratings can improve stiffnesses in conventional trapping

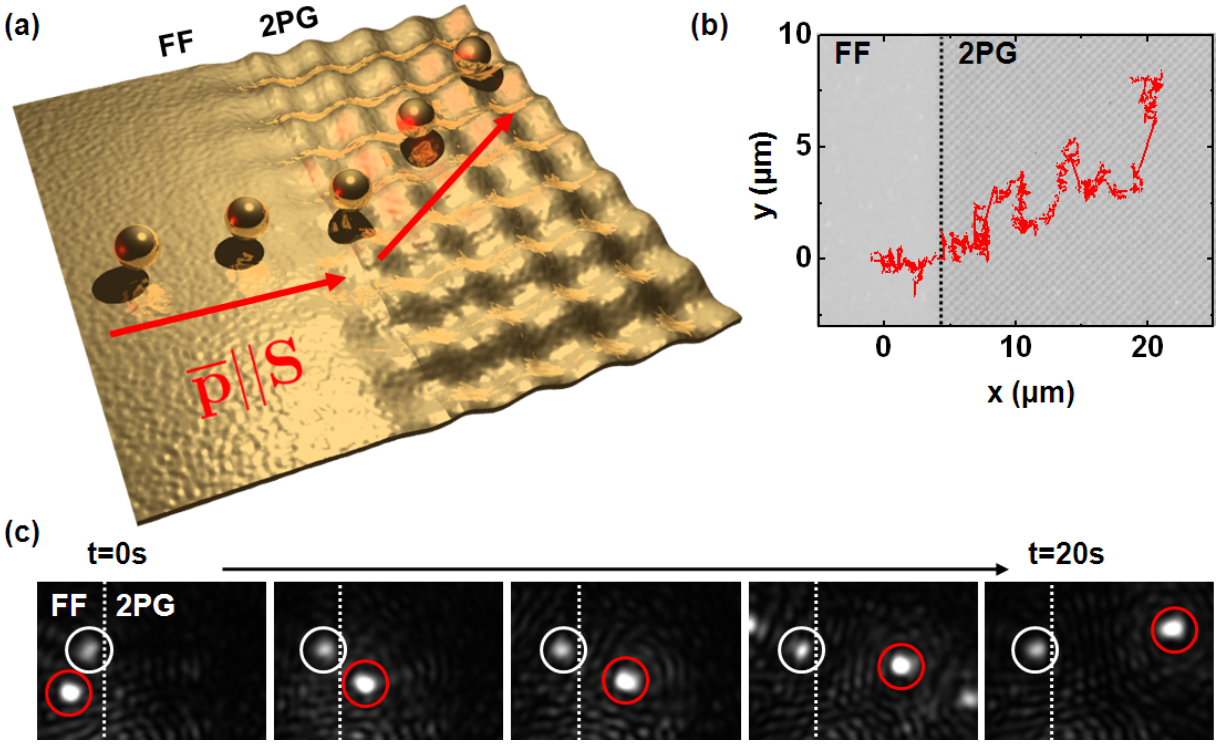

Figure 6.1.: Controlling particle motion by negative refraction of SPs: (a) Visualization of the motion of a gold nanoparticle over different timesteps. The particle momentum **p** is routed by the negatively refracted SP Poynting vector **S** while crossing the interface from the flat region (FF) to the plasmonic grating (2PG). - (b) Experimental sample trajectory of a nanoparticle across the interface - (c) Dark field images of a nanoparticle corresponding to the trajectory in (b), taken every 5 s. The motion of the free particle (red) across the interface (dashed) with respect to a particle stuck on the surface (white) is clearly visible.

configurations [191].

Following a different approach to achieve dynamic control, evanescent light fields have been used to unidirectionally propel metal nanoparticles [192–195]. Extending this idea to using the evanescent field of propagating surface plasmon modes, increased forces could be observed due to near-field coupling of particles and a gold film [25]. It will be shown in the next section how doubly periodic gratings in a similar material system can provide two-dimensional control of particle motion.

Propulsion of particles in such evanescent fields is possible due to the involved optical forces. Using the dipole approximation, and averaging forces over one optical cycle, two force components can be identified which influence the particle motion [196]: on the one

hand, a gradient force $\mathbf{F}_{\mathrm{grad}} = (1/2)\alpha_0 \nabla \mathbf{E}^2$, and on the other hand an extinction force

$$\mathbf{F}_{\mathrm{ext}} = \underbrace{\frac{2}{3}\left(\frac{\omega}{c_0}\right)^3 |\alpha_0|^2 \mathbf{S}}_{\mathbf{F}_{\mathrm{scat}}} + \underbrace{\omega \mathrm{Im}[\alpha_0]\mathbf{S}}_{\mathbf{F}_{\mathrm{abs}}}, \tag{6.1}$$

both depending on the Clausius-Mosotti polarizability of the metal sphere α_0.

For a metal particle in the field of a propagating SP, the gradient force is mainly directed normal to the surface. The extinction contribution, however, combines scattering and absorption components $\mathbf{F}_{\mathrm{scat}}$ and $\mathbf{F}_{\mathrm{abs}}$, respectively, both proportional to the plasmon Poynting vector $\mathbf{S}$. The resulting force is thus oriented along the energy flow of the SP. On flat films, this corresponds to the direction of the real part of the SP wavevector $\mathbf{k}'_{\mathrm{SP}}$, resulting in the particle propulsion observed in [25]. It will be shown in this study how this force component can be modulated at will by controlling the SP Poynting vector in metal gratings.

To analyze the effect of such forces on particle momenta, an equation of motion has to be solved taking all involved forces into account. The friction of spherical particles with small radii can be described by a drag force $\mathbf{F}_{\mathrm{d}} = -(\beta/m)\mathbf{p}$. Here β denotes the friction coefficient, which according to Stoke's law equals $\beta = 6\pi\eta R_{\mathrm{p}}$ for a particle of radius R_{p} in a fluid of viscosity η and in sufficient distance to the surface. Thermal effects, leading to Brownian motion of free particles, are described by a normally distributed force $\mathbf{F}_{\mathrm{th}}$. The resulting equation of motion hence reads as

$$\dot{\mathbf{p}} = -\frac{\beta}{m}\mathbf{p} + \mathbf{F}_{\mathrm{th}} + \mathbf{F}_{\mathrm{ext}}. \tag{6.2}$$

For large friction coefficients, as observed in the studies carried out here ($\beta/m \sim 10^7$ s^{-1}), inertial effects can be neglected. As $\mathbf{F}_{\mathrm{th}}$ possesses random orientation, an average particle momentum of

$$\overline{\mathbf{p}} = \frac{m}{\beta}\mathbf{F}_{\mathrm{ext}} \propto \mathbf{S} \tag{6.3}$$

is expected, which accordingly can be redirected by controlling the energy flow $\mathbf{S}$ of the electromagnetic field.

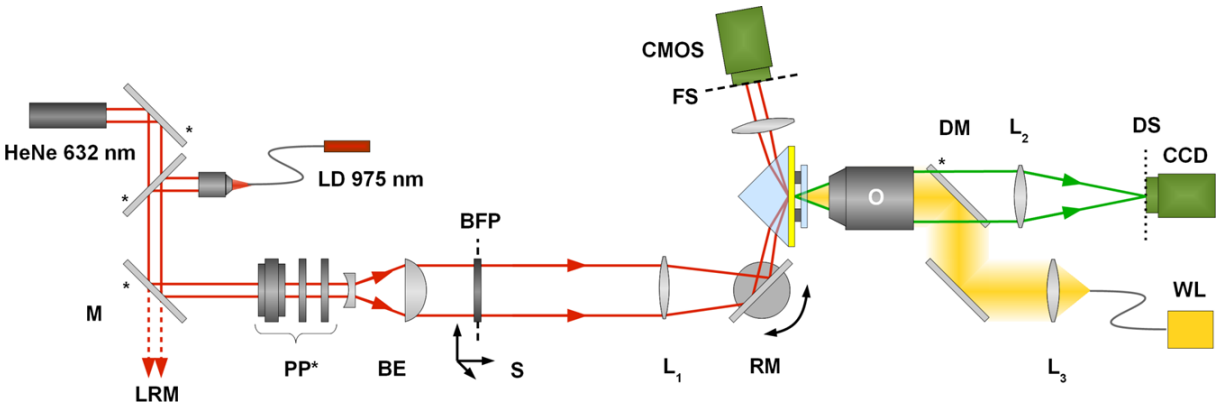

Figure 6.2.: Optical setup, composed of an ATR path for SP excitation (red) and a dark-field imaging path (green) for observation of particle motion. After polarization preparation (PP) and beam expansion (BE), light of a 300 mW laser diode emitting at $\lambda_0 = 975$ nm is weakly focused by lens L_1 with a focal length of 200 mm. The focal spot is directed through a prism to the backside of the gold film with an incident angle which is selected for resonant SP excitation by a rotatable mirror (RM). A variable and translatable slit (S) in the back focal plane (BFP) of the illumination lens is used to control the k_y component of the excited SP. The position of the slit can be controlled by imaging the reciprocal space (FS) of the reflected signal with a CMOS detector (AVT Guppy PRO F-503). The plasmon near-field is scattered by the metal nanoparticles to the far-field. It is collected in a dark-field configuration by a Nikon S Plan Fluor ELWD 20x NA=0.45 objective (O) and imaged (DS) on a high-speed CCD camera (AVT Pike F-032). A helium-neon laser (HeNe) and a white light source (WL), coupled by a dichroic mirror (DM), are available for alignment purposes. The laser sources can be coupled to the LR imaging setup discussed in chapter 3 by removal of mirror (M).

6.2. Dynamical Effects of Negative Refraction

An experiment aiming at routing metal nanoparticles by plasmonic Bloch modes on the surface of gold gratings was designed. A colloidal suspension of 250 nm diameter gold nanoparticles in water was chosen as a force probe. The suspension was encapsulated in a 70 µm high microfluidic cell. The lateral dimensions of the cell were reduced to 0.5×1 mm^2 to prevent the build-up of convection currents. A laser wavelength of $\lambda_0 = 975$ nm was chosen for SP excitation, which is slightly blue-shifted with respect to the particle resonance, causing the particles to be trapped to the surface in $-\hat{\mathbf{z}}$-direction due to gradient forces [25, 196, 197].

Doubly periodic gratings of 400×100 µm^2 dimensions in 50 nm thick gold films were fabricated, with the interface oriented, as in the previous chapter, at 45° to the grating period. A 5 nm thick protection layer of SiO_2 was evaporated on top of the gold film to prevent adhesion of nanoparticles by negative surface charges [25, 198]. A period

$P_{2PG} = 685/\sqrt{2}$ nm slightly below the Bragg condition $P_{Bragg} = \lambda_{SP}/\sqrt{2}$ was chosen ($\lambda_{SP} = 721$ nm at λ_0 on a gold-water interface). This led to IFD shapes similar to those observed in Fig. 5.6(a), resulting in all-angle negative refraction around the M point in reciprocal space. The IFD is shown in Fig. 6.3(b) and will be discussed in the next section. It shall be recalled that such a period also causes the condition $|\mathbf{k} + n\mathbf{K}_\xi + m\mathbf{K}_\zeta| > k_0$ to be fulfilled for all $n, m \in \mathbb{Z}$. Hence coupling of SPs to propagating modes in the water light cone is prohibited, and mechanical effects of such modes on particles could be excluded.

Light is also partly diffracted to modes inside the light cone in most SP nanostructure coupling configurations, as discussed in section 3.2.1. To prevent this and ensure genuine plasmonic manipulation of particles, prism coupling to SPs had to be implemented. For this purpose, a separate optical setup was designed, a sketch of which is depicted in Fig. 6.2.

SPs were excited by weakly focused TM polarized light from the sample substrate side. The incident angle could be selected with the help of a rotatable mirror (RM), allowing resonant coupling to SPs. To probe the fine-structure of the IFD, as in section 5.3, precise control over the $k_y = \mathbf{k}_{||} \cdot \hat{\mathbf{y}}$ component of the incident light was required. By placing a 3.25 mm wide translatable slit (S) in the back focal plane of the focusing lens L_1, excitation of SP with a divergence of $\delta k_y \sim 0.13$ µm^{-1} could be achieved. Fourier imaging of the light reflected from the surface on a CMOS detector was used to monitor the alignment of the slit to desired positions of the SP bandstructure. For improved contrast, these ATR reciprocal space images had to be normalized to reference images acquired under TE polarized illumination.

Nanoparticles in the SP near-field were traced by imaging scattered light in a dark-field configuration. For this purpose a microscope objective (O) was mounted on the fluid side of the sample. Images were acquired using a high-speed CCD camera to achieve sufficient temporal resolution. Sample dark-field images are shown in Fig. 6.1(c).

Particle positions were identified and traced by a dedicated tracking algorithm [199, 200]. The program is based on finding high intensity features on single image frames, after prior bandpass-filtering for noise suppression. To distinguish between image artifacts and actual particles, detected features were selected according to their eccentricities and radii of gyration. The result was a list of particle positions for every image frame.

Subsequently, positions from successive frames were linked to form a single trajectory if the distance from one frame to the next did not exceed 2.5 µm. Features were also allowed to disappear for a maximum time of 1 s to be still considered part of one trajectory. To

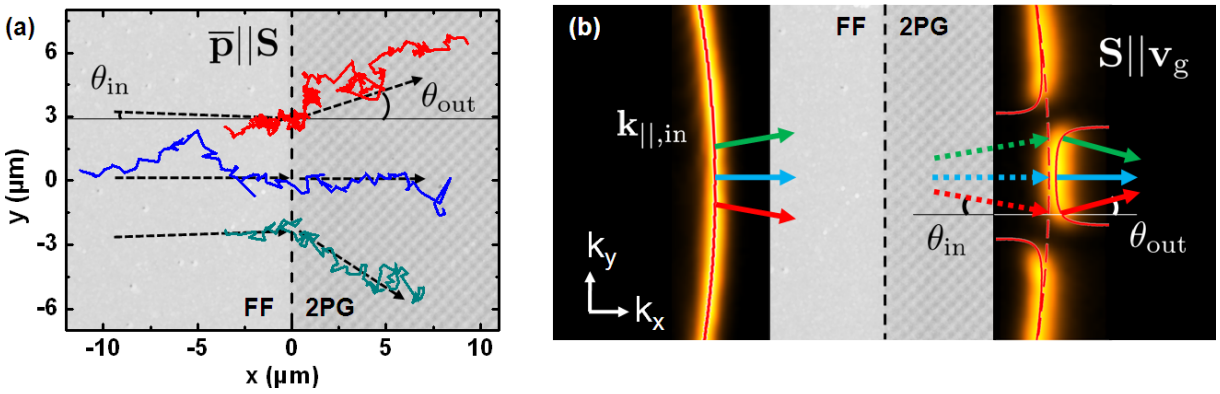

Figure 6.3.: (a) Particle trajectories at the 2PG interface for three choice of k_y. Particles impinging under normal incidence cross the interface practically unperturbed (blue), while a small change of the incident angle θ_{in} yields a large steering of the angle θ_{out} of the output trajectory. This corresponds to a mechanical equivalent of the previously discussed plasmonic superprism effect. - (b) IFD of a flat film (left) and on the applied gratings (right), acquired by reciprocal space imaging of SP leakage radiation. The group velocity, and thus also the Poynting vector $\mathbf{S}$ is oriented orthogonal to the grating according to $\nabla_{\mathbf{k}}\omega(\mathbf{k})$. Particle trajectories are dominated by optical extinction force, resulting in averaged particle momenta $\overline{\mathbf{p}}||\mathbf{S}$.

exclude stuck particles from the analysis, trajectories below a total distance from the first to the last frame of 5 µm were sorted out. Also trajectories covering less than 10 frames were not taken into account.

Examples of resulting particle trajectories at the grating interface are shown for three different choices of k_y in Fig. 6.3(a). While for $k_y \approx 0$ particles cross the interface practically unperturbed ($\theta_{out} = +3.5°$), for $k_y = -0.16$ µm^{-1} and $k_y = +0.26$ µm^{-1} routing of the particles was observed towards positive ($\theta_{out} = +14°$) and negative angles ($\theta_{out} = -16°$), respectively. In analogy to equation 5.6 for the steering of SP beams, a particle steering angle can thus be defined as

$$\sin\theta_S = \left(\hat{\overline{\mathbf{p}}}_{in} \times \hat{\overline{\mathbf{p}}}_{out}\right) \cdot \hat{\mathbf{z}} \tag{6.4}$$

Here the unit vectors of averaged particle momenta were used, $\hat{\overline{\mathbf{p}}}_{in}$ and $\hat{\overline{\mathbf{p}}}_{out}$, on the flat film and inside the 2PG, respectively.

Comparing the particle trajectories to the IFD given in Fig. 6.3(b), the averaged directions of motion indeed resemble those expected from steering of surface plasmon beams. Recalling the expected proportionality of averaged particle momentum and Poynting vector from equation 6.3, the observed steering at the interface can be phrased as $\hat{\overline{\mathbf{p}}}_{out} - \hat{\overline{\mathbf{p}}}_{in} = \hat{\mathbf{S}}^{2PG} - \hat{\mathbf{S}}^{FF}$.

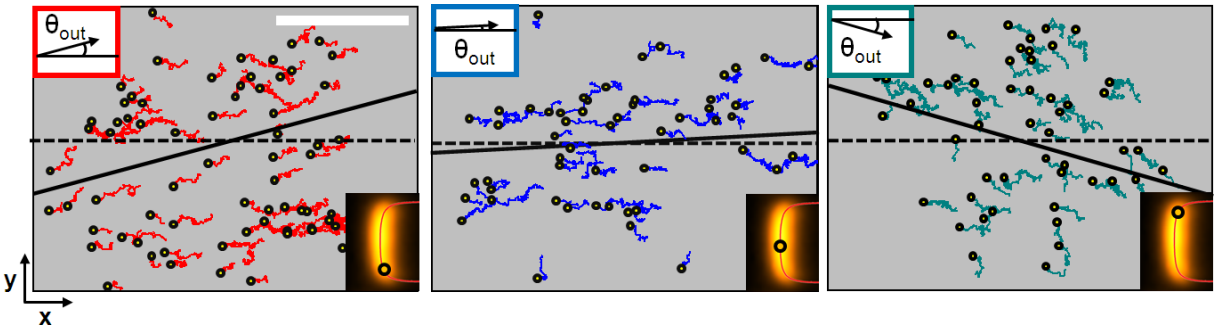

Figure 6.4.: Ensembles of particle trajectories for $k_y = -0.16\ \mu\text{m}^{-1}$ (red), $k_y = +0.06\ \mu\text{m}^{-1}$ (blue), and $k_y = +0.26\ \mu\text{m}^{-1}$ (green), resulting in propagation angles of $\theta_{\text{out}} = +14°$, $+3.5°$ and $-16°$, respectively. The scale bar corresponds to 50 µm, k_y-positions in reciprocal space are visualized in the insets.

With $\hat{\mathbf{S}}^{\text{FF}}||\hat{\mathbf{k}}_{\text{in}}^{\text{SP}}$ and $\hat{\mathbf{S}}^{\text{2PG}}||\hat{\mathbf{v}}_{\text{g}}^{\text{2PG}}$, one finds

$$\hat{\bar{\mathbf{p}}}_{\text{out}} - \hat{\bar{\mathbf{p}}}_{\text{in}} = \hat{\mathbf{v}}_{\text{g}}^{\text{2PG}} - \hat{\mathbf{k}}_{\text{in},||}^{\text{SP}}. \tag{6.5}$$

The optical effect of refraction of SP beams at the grating interface is hence transformed to a mechanical effect, resulting in a dynamic law of refraction.

6.3. Quantitative Analysis of Particle Routing

For a quantitative analysis of the achieved particle steering angles, ensembles of particle trajectories inside the 2PG were analyzed. Ensembles acquired for three choices of k_y are shown in Fig. 6.4.

For each value of k_y, incremental particle displacements $\Delta\mathbf{r} = \mathbf{r}(t+\Delta t) - \mathbf{r}(t)$ over timesteps Δt were analyzed, taking into account data from multiple trajectories j. Without an external force, resulting two-dimensional histograms of the frequency of displacements $(\Delta x, \Delta y)$ would be expected to follow the normal distribution of Brownian motion, with a variance $\sigma^2 = 4k_{\text{B}}T\Delta t/\beta$.

It can be shown that in a field of constant force, this distribution remains normal but is translated in the $(\Delta x, \Delta y)$-plane with a shift $\langle\Delta\mathbf{r}\rangle = \mathbf{F}_{\text{ext}}\Delta t/\beta$, while the variance of the distribution remains unchanged. Hence particle steering angles were estimated from such shifts as $\tan(\theta_{\text{out}}) = \langle\Delta y\rangle/\langle\Delta x\rangle$.

Resulting steering angles are plotted as a function of k_y in Fig. 6.5(a). In a range of incident

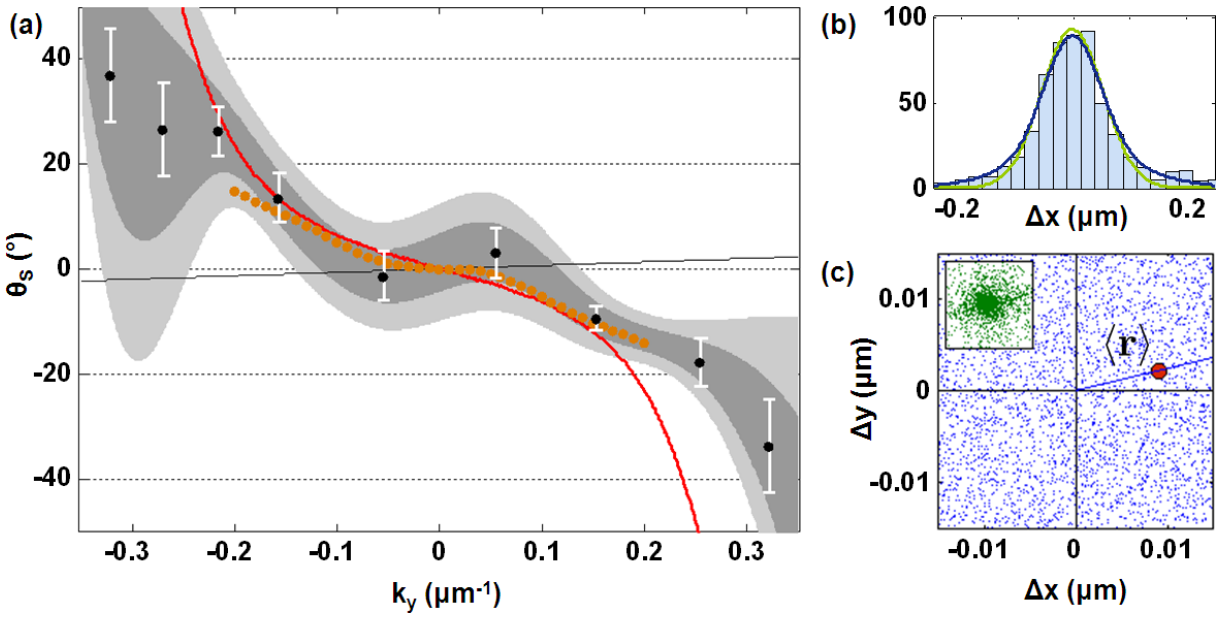

Figure 6.5.: (a) Experimentally acquired particle steering angles θ_S (black dots) as a function of the incident k_y component. Predictions from experimental (orange) and calculated (red) IFDs are shown for comparison. Uncertainty determined from experimental reproducibility is shown as white bars and compares well to statistically predicted confidence intervals σ_{θ_S} (dark gray) and $2\sigma_{\theta_S}$ (light gray). Comparison with θ_{in} (black line) reveals the dynamic superprism effect. - (b) Frequency of particle displacement in $\hat{\mathbf{x}}$-direction. While mere Gaussian fitting (green) results in deviations of experimental data from the fit at large Δx, a multi-Gaussian fit (dark blue) reproduces the experimental result well. - (c) Scheme of determination of the particle propagation angle from the center of a shifted normal distribution as $\tan\theta_{out} = \langle\Delta y\rangle/\langle\Delta x\rangle$. The full distribution is shown in the inset.

$k_y = \pm 0.32\ \mu m^{-1}$ steering of particles to more than $\mp 30°$ is observed. Moreover, the experimental results agree well with predictions from fitting of plasmonic bandstructures acquired by LR microscopy given in the graph.

While propagation angles θ_{out} can be well detected by our experimental configuration, in principle also an estimation of the mean force $|\mathbf{F}_{ext}|$ should be possible by analysis of the amplitude $|\langle\Delta\mathbf{r}\rangle|$. However, it has to be taken into account that particles also are subject to Brownian motion in the direction normal to the surface. At varying distance from the metal they thus experience different evanescent field amplitudes, and only effective force amplitudes can be probed experimentally.

The unknown z-position of particles also influenced the statistical precision with which the steering angle θ_S could be determined. Taking into account the mean displacement per timestep $|\langle\Delta\mathbf{r}\rangle|$ and the size of the statistical ensemble N, confidence intervals $\sigma_{\theta_S} = \sigma/(\sqrt{N}|\langle\Delta\mathbf{r}\rangle|)$ could be calculated. These are shown in Fig. 6.5(a) (gray areas), and

reproduce the observed experimental fluctuations well (white bars).

Variations in z also led to weak modifications of the shape of the $(\Delta x, \Delta y)$-distribution as shown in Fig. 6.5(b). While particles far from the surface experience unperturbed Brownian motion, particles in the vicinity of the metal surface are expected to possess modified diffusion coefficients $D(z)$ due to variations, resulting in a change of displacement variances $\sigma^2(z) = 2D(z)\Delta t$ [201, 202]. As the statistical ensembles collected for each k_y contained information for a multitude of heights z, a distribution corresponding to a sum of Gaussians with varying variance was observed. It shall be stressed, however, that this modification did not change the expectation value of the measured steering angle θ_S.

6.4. Conclusions

It has been demonstrated in this chapter that metal nanoparticles can be manipulated by negative refraction of surface plasmons. SPs on metal gratings have been shown to imprint the plasmonic superprism effect demonstrated in the previous chapter on particle motion. Routing of large particle ensembles has been achieved, making it particularly interesting for microfluidic applications requiring high-throughput particle flow control.

Part III.

Plasmonic Sensing by Leakage Radiation Microscopy

7 Fano Resonance Enhanced Plasmonic Sensing

So far this thesis focused on plasmonic circuitry, demonstrating dielectric lenses, GRIN structures, and plasmonic crystal effects such as beam steering, negative refraction and self-collimation. The application of such molded SPs for optical micromanipulation has also been discussed. For the analysis of those optical elements, LR microscopy has proven to be a powerful tool, allowing SP imaging in real as well as in reciprocal space.

One of the most important applications of plasmonics, however, is SP resonance (SPR) based refractive index sensing. A short overview of the subject has been given in section 2.3. Various methods have been introduced for sensing with localized and with propagating surface plasmons. Especially the latter, mostly excited in attenuated total reflection (ATR) geometry, have brought SPR sensing resolution close to its theoretical limits [116].

It will be presented in the following how the asymmetry of Fano profiles observed in reciprocal space LR micrographs of SPs launched from nano-apertures can be exploited for improving sensing figures of merit (FOM). For this purpose, the Fourier-space imaging capability of LR microscopy has been applied for SPR sensing. The results of this chapter have been published in the Journal of Physical Chemistry C in 2012 [5] ().

A second technique combining the benefits of LR microscopy and plasmonic crystals will be presented in chapter 8.

7.1. Fano Resonances

Fano resonances were first observed in atomic and molecular physics [203], and were studied in many other systems since, ranging from quantum electronics to SP photonics [204], in particular the extraordinary transmission in nanohole arrays [205, 206]. Fano resonances

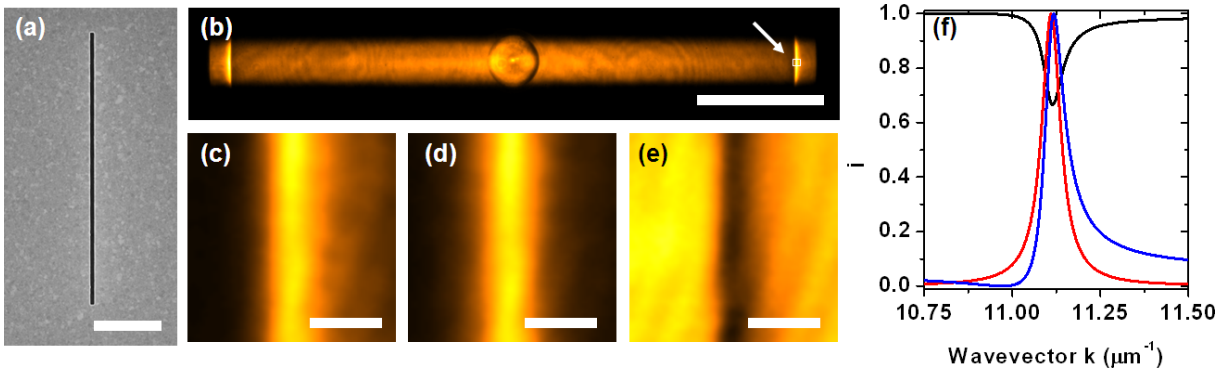

Figure 7.1.: (a) Scanning electron micrograph of a 20 µm long and 300 nm wide slit in an 80 nm thick Au film. The scale bar corresponds to 5 µm. - (b) Reciprocal space LR micrograph of SPs launched by focusing a $\lambda_0 = 782$ nm laser diode on this nanoslit. SPs are propagating on a water/Au interface. The scale bar corresponds to 5 µm^{-1}. - (c-e) Magnified part of the Fourier space, marked by the white box in (b): different optical configurations allow observation of Fano (c), Lorentzian (d) and ATR (e) profiles on the same structure. Scale bars correspond to 0.1 µm^{-1} - (f) Analytically calculated ATR (black), Lorentz (red) and Fano (blue) profiles of normalized intensity i for an 80 nm thick Au film.

arise when a scattering process takes places either directly to a continuum of states, or via a resonant state which is then coupled to the continuum. The interference of these two channels causes asymmetric lineshapes, the so called Fano profiles.

Fano resonances were suggested for sensing with LSPR sensors ([207], for a review, see [208]). However, it was also pointed out that their increased linewidths might derogate the performance of plasmonic sensors, leading to proposals of how to actually avoid natural Fano lineshapes in sensing on nanohole arrays by polarization control [209].

In the work presented here, Fano resonances in LR microscopy reciprocal space were investigated stemming from the interference of SP leakage radiation and direct transmission diffracting through a nanoslit. The source geometry has already been addressed in section 2.2.1, and the different light fields involved in LR microscopy, responsible for the Fano interference, in section 3.2.1. The SP source, as well as a typically achieved Fano profile, are depicted in Fig. 7.1(a-c). For a subwavelength slit the resulting resonance can be modeled in k-space as a coherent superposition of a Lorentzian SP contribution and an approximately wavevector independent diffraction amplitude t_{slit} [41]:

$$I(k) = \left| t_{\mathrm{slit}} + \alpha e^{i\phi} \cdot \frac{i k''_{\mathrm{SP}}}{(k - k'_{\mathrm{SP}}) + i k''_{\mathrm{SP}}} \right|^2 \tag{7.1}$$

Here α denotes the complex SP amplitude and ϕ the relative phase between diffracted and SP leakage components. It will be shown in the following that such a superposition can yield high contrast peaks with increased maximum slopes, and how such peaks can be utilized for increasing sensing sensitivities.

7.2. Sensitivity Optimization

As detailed in section 2.3, the effect of refractive index changes on plasmonic resonances can be monitored in intensity, angle or wavelength interrogation schemes. Here an intensity measurement scheme as visualized in Fig. 7.2(a) was chosen: a change in refractive index δn yields a change of normalized intensity $i(k_0) = I/\max(I)$ at a fixed operating point k_0 in reciprocal space. It will be shown in the following that this scheme allows to benefit from the increase in maximum slope of asymmetric Fano profiles.

Using the same convention as for conventional ATR systems [92], the sensitivity of such a

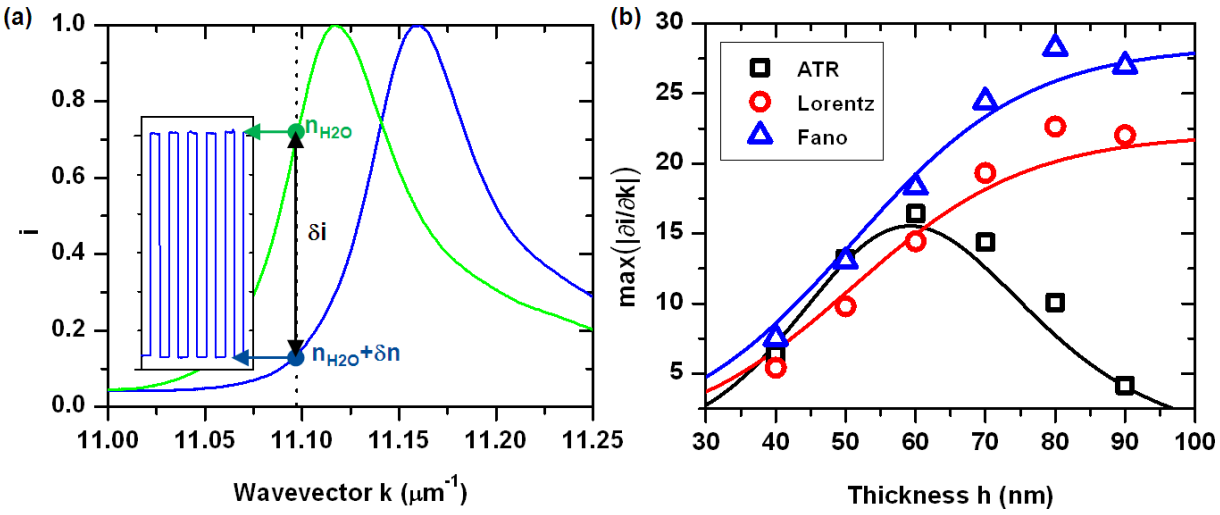

Figure 7.2.: (a) Implemented intensity measurement scheme: A change in refractive index δn leads to a shift of the peak in k-space. When probing the intensity at the point k_0 of highest slope $\partial i/\partial k$, a change in normalized intensity i results. Here the shift of a Fano peak on an $h = 80$ nm Au film for $\delta n = 4.3 \times 10^{-3}$ RIU is depicted. In the inset the variation of local intensity i over multiple liquid exchanges is shown. - (b) Dependence of the maximum slope $\max(|\partial i/\partial k|)$ on the film thickness h for ATR (black), Lorentz (red) and Fano (blue) profiles. Experimental results are plotted as open markers, slopes from calculations as solid curves.

sensor is defined as

$$S = \left| \frac{\partial i(k - k'_{\mathrm{SP}})}{\partial n} \right| = \left| \frac{\partial i(k)}{\partial k} \right| \left| \frac{\partial k'_{\mathrm{SP}}}{\partial n} \right|, \tag{7.2}$$

It should be stressed that for intensity measurement schemes, S is equivalent to the FOM of the sensor: while the second factor $\partial k'_{\mathrm{SP}}/\partial n$ is constant and determined by the dispersion of a propagating SP on a thin planar film (thus corresponding to the sensitivity of an angle measurement scheme), the first factor $\partial i/\partial k$ describes the slope of the SP resonance in reciprocal space. For a normalized Lorentzian, $\partial i_{\mathrm{L}}/\partial k$ is solely determined by the width of the peak.

Typical sensing experiments would be performed around an operating point k_0 where $|\partial i/\partial k|$ is maximized. To evaluate the maximum slopes of Fano profiles $i_{\mathrm{F}}(k)$, LR microscopy measurements on gold films of different thickness were performed using the optical setup discussed in section 3.2.2. To guarantee well comparable experimental conditions for varying film heights, stripes of different metal film thickness had been evaporated on on single sample by consecutive steps of shadow-mask evaporation. SPs were launched from 300 nm wide nanoslits fabricated by focused ion-beam lithography (see Fig. 7.1(a)). As discussed in section 2.3.2, a wavelength in the near-infrared allowed achieving good bulk sensitivity, while still maintaining tight confinement of the SP field to the metal surface. Operation in a water environment ($n_{\mathrm{H2O}}(782\ \mathrm{nm}) = 1.328$) was chosen as required for potential future biosensing applications. The reciprocal space was further magnified with the help of a Nikon Plan Fluor S 40x NA=0.60 microscope objective and a 200 mm tube lens as depicted in Fig. 3.5 to reach sufficient sampling of the resonance profiles.

Comparison of Fano profiles with conventional ATR resonances $i_{\mathrm{ATR}}(k)$ was achieved by also acquiring ATR profiles on the same substrates using the alternative ATR beam path provided by the LR microscopy setup (see Fig. 3.5). Note that this ATR-like configuration is equivalent to these used by Kano and Knoll [114]. As a control experiment, Lorentzian profiles $i_{\mathrm{L}}(k)$ were extracted by spatially filtering the light diffracted from the slit in an intermediate real space plane. The Fano interference is thus canceled, leaving a mere SP Lorentz profile. LR microscopy images and cross-sections of all three profiles are shown in Figs. 7.1(b-f).

The extracted maximal slopes $\max(|\partial i/\partial k|)$ for all three profiles and film thicknesses of 40 nm to 90 nm are depicted in Fig 7.2(b). Numerically calculated values are also shown (solid lines). Values for the reflection coefficient in ATR configuration as well as the complex wavevectors $k_{\mathrm{SP}} = k'_{\mathrm{SP}} + ik''_{\mathrm{SP}}$ were extracted from calculation of complex Fresnel coefficients for different film thickness (see section 2.1.2 for details). Fano profiles

were modeled according to equation 7.1 for the same k_{SP} values, and parameters t_{slit}, α and ϕ extracted from fits to experimental data. The resulting curves agree well with experimental data.

For ATR profiles of varying thickness (black), a clear optimum of the slope $\max(|\partial i/\partial k|)$ was observed around $h = 60$ nm. This is a result of competing coupling and decoupling processes for the reflection geometry: while for thick films light cannot couple to SPs through the film and thus the peak depth is reduced, for very thin films this coupling is very efficient, but the peak width broadens due to decoupling loss associated with leakage radiation.

Peaks observed in LR microscopy geometry do not suffer this trade-off. The slope of Lorentz profiles (red) is steadily increasing with film thickness, and is saturating above $h \approx 80$ nm. This corresponds to a region where the decoupling loss due to leakage radiation becomes negligible relative to the intrinsic material loss of propagating SPs:

$$\frac{k''_{\mathrm{SP}}\left(h = 80\ \mathrm{nm}\right) - k''_{\mathrm{SP}}\left(\infty\right)}{k''_{\mathrm{SP}}\left(\infty\right)} < 0.1 \tag{7.3}$$

Therefore operation at higher maximum figures of merit is rendered possible with Lorentz profiles in comparison to ATR.

The same saturation was observed for Fano profiles (blue), however yielding generally higher slopes than mere Lorentzian peaks. A $\sim 70\%$ improvement in slopes was reported for a Fano profile on an $h = 80$ nm thick film over the best achievable ATR data. Thus similarly strong improvements are expected for sensing sensitivities based on such peaks.

7.3. High-Resolution Sensing Experiment

In order to confirm the sensitivity improvement predicted by analysis of the resonance profiles, a high-resolution sensing experiment using the leakage radiation microscope presented in chapter 3 was performed to probe refractive index changes below 10^{-5} RIU. Aqueous solutions of ethanol (Carlo Erba absolute anhydrous ethanol) were prepared as a refractive index reference, corresponding to differences in index of refraction $\delta n = n_{\mathrm{sol}} - n_{\mathrm{H_2O}}$ ranging from $\delta n_{\max} = 5.4 \times 10^{-3}$ RIU (at a concentration of 8.3×10^{-2} w/w of dissolved ethanol) to $\delta n_{\min} = 3.4 \times 10^{-6}$ RIU (5.2×10^{-5} w/w ethanol).

To allow simple exchange of the sample liquids without perturbing the system, the SP

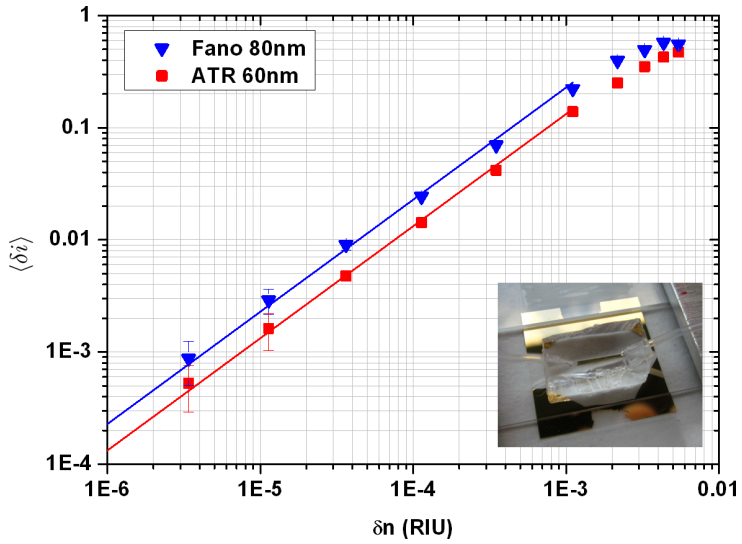

Figure 7.3.: Double logarithmic plot of the normalized intensity change $\langle \delta i \rangle$ as a function of the refractive index variation δn. Data was acquired from aqueous ethanol solutions with known refractive index on optimal Fano (blue triangles) and ATR profiles (red squares). Fits from linear regression on results with $\delta n \leq 10^{-3}$ RIU are plotted as solid lines. The corresponding slopes yield sensitivities of $S_{\mathrm{F}} = \partial i_{\mathrm{F}}/\partial n = 234 \pm 1$ RIU^{-1} for Fano and $S_{\mathrm{ATR}} = \partial i_{\mathrm{ATR}}/\partial n = 134 \pm 1$ RIU^{-1} for ATR profiles. A picture of the used PDMS sensing cell is shown in the inset.

source was encapsulated in a microfluidic cell. The latter was prepared by soft-lithography in Polydimethylsiloxane (PDMS) after prior photo-lithographic preparation of a mold in Microchem SU-8 resist. Covalent bonding of the PDMS cells to glass could be achieved by prior activation of both surfaces in oxygen plasma. The lateral size of the gold films had to be limited to dimensions which could fit the micofluidic channel. This was achieved by evaporating Au through a 0.5 mm rectangular aperture of an aluminum shadow mask placed on the glass substrate. A resulting sensing cell is shown in Fig. 7.3.

Reciprocal space images were acquired in optimized ATR ($h = 60$ nm) and Fano ($h = 80$ nm) configurations. Profiles were extracted by vertical spatial averaging over 960 rows of CCD pixels. Variations in normalized intensity δi were traced at the point k_0 of highest slope. An example was already discussed in Fig. 7.2(a).

Each of these measurements i_j was temporally averaged over $N = 100$ ($N = 10$ for ATR) consecutive frames to yield $\bar{i}_l = \frac{1}{N} \sum_{j=(l-1)\cdot N+1}^{l \cdot N} i_j$. To calibrate the sensor, each solution was referenced against a measurement with pure water. Iterating such pairs of measurements over six cycles yielded periodic curves as depicted in the inset of Fig. 7.2(a). To compensate for linear signal drift, a measurement for the index difference was extracted

from three consecutive datapoints as

$$\delta i_j = \frac{(-1)^j}{2}\left(\bar{i}_j - 2\bar{i}_{j+1} + \bar{i}_{j+2}\right). \tag{7.4}$$

This generated a dataset of $M = 10$ values δi_j. To increase sensing precision, these M values were subsequently averaged yielding one datapoint $\langle \delta i \rangle$.

Performing such data treatment for each concentration of ethanol in water yielded datapoints $\langle \delta i \rangle$ as a function of δn which are presented in Fig. 7.3. Linear regression on these points revealed sensitivities of $S_{\mathrm{ATR}} = (\partial i/\partial n)_{\mathrm{ATR}} = 134 \pm 1$ RIU^{-1} for ATR and $S_{\mathrm{F}} = (\partial i/\partial n)_{\mathrm{F}} = 234 \pm 1$ RIU^{-1} for Fano resonances. This corresponds to a 75% increase of the sensitivity, and thus the FOM of the introduced Fano sensor compared to the best achievable ATR configurations. This result is in good agreement with the predictions by analysis of single profiles presented above.

The improvement of the FOM is of fundamental nature, relying on the interference induced asymmetry of Fano resonances. Such interferences are natural to leakage radiation micrographs of SPs launched from nanoapertures. However, they could potentially also be observed on optical setups based on standard prism decoupling, provided that a similar launching geometries is used. In such a way the observed FOM improvement could also be made available for prism based sensing.

7.4. Noise and Resolution

As described in section 2.3.2, the FOM, which here is given by the sensitivity S, is a measure of the performance which could potentially be achieved by the described optical configuration. To additionally estimate the current practical sensing resolution $\sigma_{\delta n}$ of our system as implemented in the laboratory, technical noise characteristics of the applied components such as sources and detectors needed to be characterized.

For this purpose a baseline curve over 5×10^4 image frames was acquired, and subsequent numeric noise analysis was performed for the Fano geometry. The standard deviation $\sigma_{\delta i_j}$ of a single δi_j measurement was determined as a function of the number of averaged frames N. The result is depicted in Fig. 7.4(a) (back curve). For small N, the deviation $\sigma_{\delta i_j}$ scales as $1/\sqrt{N}$, suggesting a shot noise limited signal. For large averaging ranges ($N > 20$), non-linear low-frequency drifts start to dominate, leading to an increase in $\sigma_{\delta i_j}$.

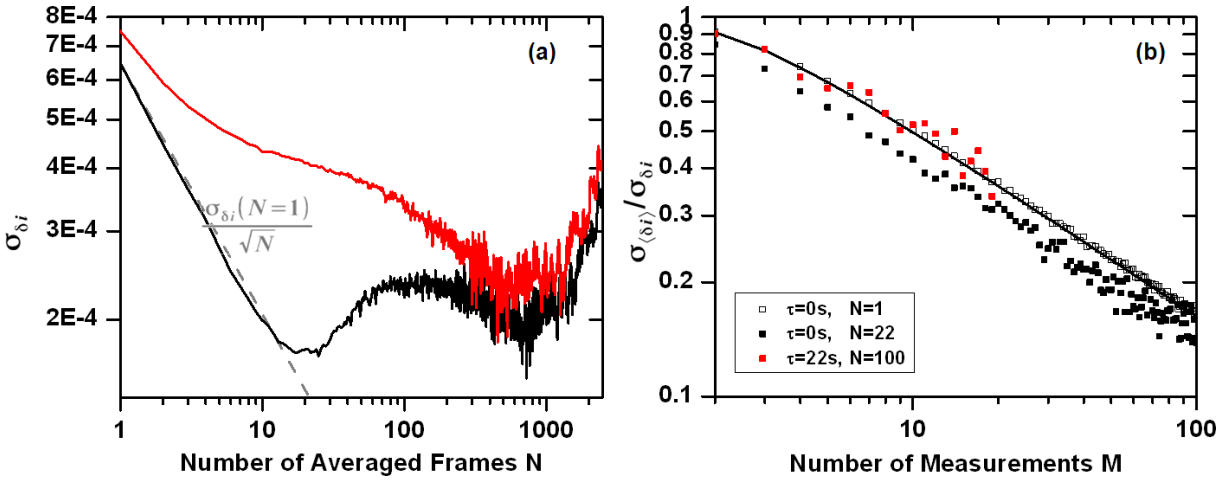

Figure 7.4.: (a) Standard deviation $\sigma_{\delta i}$ of the averaged normalized intensity as a function of the number of averaged frames N. Liquid exchange between two measurements add a delay time to the averaging process. $\sigma_{\delta i}$ is depicted for a negligible delay ($\tau = 0$, black) as well as for the applied $\tau = 22$ s (red). A $1/\sqrt{N}$ curve is shown for comparison. - (b) Decrease of the standard deviation with number of averaged measurements M. From Gaussian uncertainty propagation calculations the ratio $\sigma_{\langle\delta i\rangle}/\sigma_{\delta i}$ is expected to scale as $\sqrt{(8M-6)/3M^2}$. This is observed for short ($\tau = 0$ s, $N = 1$) as well as long averaging ranges ($\tau = 22$ s, $N = 100$). The intermediate regime ($\tau = 0$ s, $N = 22$) shows a slightly different scaling, which can be attributed to systematic noise effects.

The above values were calculated for a negligible liquid exchange time τ. For the implemented microfluidic system the change was yet performed manually by two syringes, so a practical delay of $\tau = 22$ s had to be accounted for. This delay led to an increase in $\sigma_{\delta i_j}$ (red curve), especially for small N. For large N the exchange time τ becomes negligible compared to the averaging time $\tau_{\mathrm{AVG}} = Nt_{\mathrm{s}}$ (with the exposure time for one frame $t_{\mathrm{s}} = 80$ ms), yielding a minimum $\sigma_{\delta i_j}$ for $N \approx 500$.

Besides varying the number of averaged frames N, it is also possible to increase the number M of averaged measurements δi_j. Assuming uncorrelated measurements $\bar{i}_j$, Gaussian uncertainty propagation predicts scaling of the ratio $\sigma_{\langle\delta i_j\rangle}/\sigma_{\delta i_j}$ as $\sqrt{(8M-6)/3M^2}$. This relation is plotted in Fig. 7.4(b) (black curve). Measured data extracted from baseline analysis agrees well with this prediction, yielding a standard deviation of $\sigma_{\langle\delta i_j\rangle} = 1.7 \times 10^{-4}$ for the conditions used in Fig. 7.3 ($\tau = 22$ s, $N = 100$, $M = 10$). This results in a practical resolution of our laboratory system of $\sigma_{\delta n} = \sigma_{\langle\delta i_j\rangle}/S_{\mathrm{F}} = 7.4 \times 10^{-7}$ RIU.

Our system leaves room for optical, electronic and mechanical improvements. Implementation of standard electronic micofluidic controls would, e.g., lead to negligible liquid exchange times τ. Assuming optimized $N = 22$ and reasonable $M = 50$, this would already yield a

standard deviation of $\sigma_{\langle \delta i_j \rangle} = 3.3 \times 10^{-5}$, promising a resolution of $\sigma_{\delta n} = 1.4 \times 10^{-7}$ RIU. Such a value is comparable to the best reported systems up-to-date (compare section 2.3), and higher resolutions can be expected upon further technical optimization of the setup.

7.5. Conclusions

It was demonstrated in this chapter how the asymmetry of Fano resonances can improve the slope $\partial i/\partial k$ of SP resonance profiles, leading to an increase of the FOM of plasmonic refractive index sensors of 75% over optimal ATR geometries. This improvement could contribute to efforts aiming at extending the theoretical limits of SPR sensing resolution. A detailed noise analysis of the system has been presented, and resolutions on the order of 10^{-7} were achieved.

The results required introducing standard LR microscopy as a tool for refractive index sensing. Based on a simple and compact imaging setup, LR microscopy allows simultaneous imaging of real and Fourier spaces. This could potentially lead to direct imaging of, e.g., biological binding events while simultaneously monitoring refractive index evolution. In contrast to ATR microscopy, LR microscopy permits independent control of the excitation conditions, and polarization sensitive techniques could be easily integrated. LR microscopy moreover provides high spatial resolution. Thus multiple sensing channels, densely integrated on a single substrate, could be serially addressed by mechanical scanning. In addition, access to the full reciprocal space is provided, which could possibly be exploited for multi-directional SP sensing.

Such full monitoring of the reciprocal space proved useful also in the field of SP circuitry, especially for interrogating the effect of plasmonic gratings on isofrequency surfaces. It will be shown in the following chapter how LR microscopy of the anisotropic bandstructure in such gratings provides another promising means for SP based sensing.

8 Plasmonic Crystal Enhanced Refractive Index Sensing

It was demonstrated in the previous chapter that the shape of the SP resonance can affect the achievable sensing figures of merit. While the first factor $\partial i/\partial k$ of the sensor sensitivity $S_i = \partial i/\partial n$ (equation 7.2) in an intensity interrogation scheme could by optimized in such a fashion, the second factor $\partial k'_{\mathrm{SP}}/\partial n$ turned out constant, given by the isotropic dispersion relation $\omega(k_{\mathrm{SP}})$ of SPs on a planar interface. In chapters 5 and 6, however, anisotropic dispersion relations $\omega(\mathbf{k}_{\mathrm{SP}})$ were observed in plasmonic gratings.

It will be presented in the following how such anisotropy can be exploited for high-resolution refractive index sensing. Defocused SP imaging by LR microscopy was used to additionally enhance SP sensing figures of merit. The idea for this technique was developed

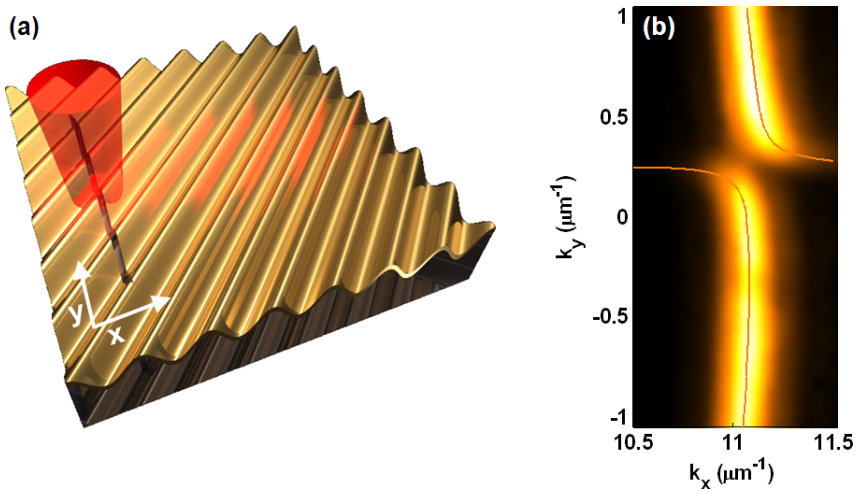

Figure 8.1.: (a) Plasmonic crystal sensing scheme. SPs are launched by monochromatic illumination of a nanogroove source oriented 45° to a sinusoidal metal grating. - (b) IFD around the M-point of a $P = 580/\sqrt{2}$ nm gold grating in a water environment, illuminated at $\lambda_0 = 782$ nm. The image was acquired by LR microscopy of the reciprocal space, theoretical modeling (solid line) was preformed as discussed in chapter 5 for a modulation amplitude $\gamma = 3.7 \times 10^{-2}$.

as part of the work on SP steering and negative refraction presented in chapter 5, and was published alongside these results in [2]. A similar proposal has also been reported for ATR configurations in [210]. A journal publication of the experimental implementation described in this chapter is in preparation.

8.1. Bandgap Enhanced Sensing Principle

The proposed sensor geometry is visualized in Fig. 8.1 (a). A nanogroove source is illuminated by a laser spot to launch SPs propagating inside a sinusoidal metal grating (1PG). For a grating period chosen close to the Bragg condition, bandgaps similar to those discussed in chapter 5 around the M-point of the grating appear, as seen from the corresponding isofrequency contour diagram (IFD) shown in Fig. 8.1(b).

For sensing applications, the effect of a refractive index change in such gratings was analyzed. An example is visualized in Fig. 8.2(a), and compared to the response on a flat metal film. For the presented study, a wavevector interrogation scheme was chosen (see section 2.3.2) using the k_x-coordinate of the real part of the SP resonance wavevector,

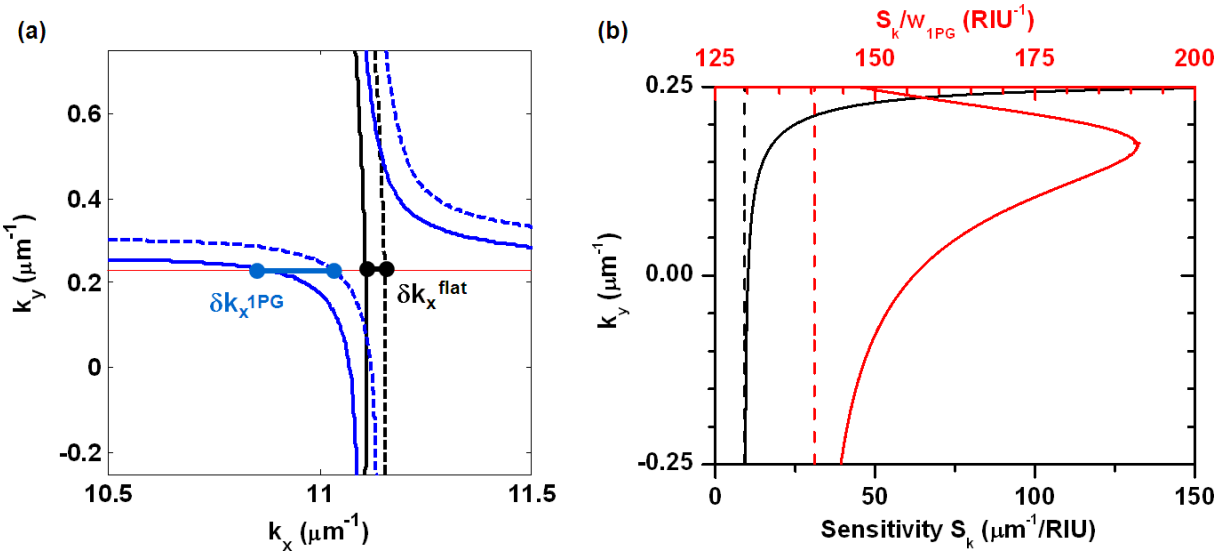

Figure 8.2.: Sensing sensitivity on plasmonic gratings: (a) On a flat gold film, SP modes are located on a circle in the IFD (black solid curve). A small change of the refractive index leads to an equivalent increase of the circle radius (dashed), given by the SP dispersion relation. Plasmon modes inside a 1PG possess an anisotropic IFD (blue). The same change δn in such a grating results in an equivalent increase in the detected change $\delta k_x^{\mathrm{1PG}}$. - (b) Calculation of the sensing sensitivity $S_k = \partial k_x^{\mathrm{SP}}/\partial n$ and the sensor figure of merit S_k/w for SPs in a $P = 580/\sqrt{2}$ nm grating

determined here as k_x^{SP}, as a sensing meter at a fixed k_y position. In the case of the flat film, a small change of the refractive index δn yields a shift $\delta k_x^{\mathrm{flat}}$ of k_x^{SP} as given by the SP dispersion relation (black). Inside the 1PG, however, the anisotropic bandstructure acts as a lever on the detected wavevector change, and increased changes $\delta k_x^{\mathrm{1PG}}$ are observed (blue).

Such levering results in an equivalent increase of the sensor sensitivity, defined as $S_k = \partial k_x^{\mathrm{SP}}/\partial n$ for wavevector interrogation. The evolution of S_k with the choice of k_y is depicted in Fig. 8.2(b) for the inner branch of the IFD. Close to the Bragg condition around $k_y = 0.25\ \mu\mathrm{m}^{-1}$, a large increase of the sensitivity (black) is observed, stemming from the diverging slope of the SP band at this point.

The performance of the sensor can be evaluated by choosing the standard definition of the figure of merit discussed in chapter 2.3.2, FOM $= S_k/w$, with the full width at half maximum of the peak w. At a flat interface, the width is given by the SP loss as $w_{\mathrm{flat}} = 1/2k''_{\mathrm{SP}}$. Assuming the same loss on a grating, the width at an arbitrary point of the IFD of a grating would broaden due to a geometric increase of the cross-section as $w_{\mathrm{1PG}} = w_{\mathrm{flat}}/\cos(\arctan(\partial k_x^{\mathrm{SP}}/\partial k_y))$. For such a situation, from Fig. 8.2(b) still an improvement of the FOM (red curve) of 36% for an optimal choice of k_y is expected.

8.2. High-Resolution Sensing Experiment

To verify the expected sensitivity enhancement, a high-resolution sensing experiment was designed. Smooth metal gratings were fabricated in indium-tin oxide as discussed in chapter 5, and an 80 nm thick gold layer was deposited on top. A period of $P = 580\ \mathrm{nm}/\sqrt{2}$ was chosen, close to the Bragg period of SPs at a gold-water interface, $\lambda_{\mathrm{SP}} = 2\pi/k'_{\mathrm{SP}} = 566$ nm for a laser wavelength $\lambda_0 = 782$ nm.

To allow controlled exchange of the dielectric environment of the sensor, again the device had to be encapsulated in a PDMS microfluidic cell. However, as the grating fabrication was based on ITO coated substrates, bonding of PDMS to glass by simple oxygen plasma activation as performed in chapter 7 could not be used. To achieve covalent bonding between PDMS and the gold surface, (3-Mercaptopropyl)trimethoxysilane (Sigma-Aldrich) was applied from a 2% solution in methanol. The molecule provides a silane endgroup for binding to the PDMS mesh, as well as an opposing thiol group for bonding to the gold substrate [211]. A sketch of the bound compound, together with a picture of the fabricated cell, is shown in Fig. 8.3(a).

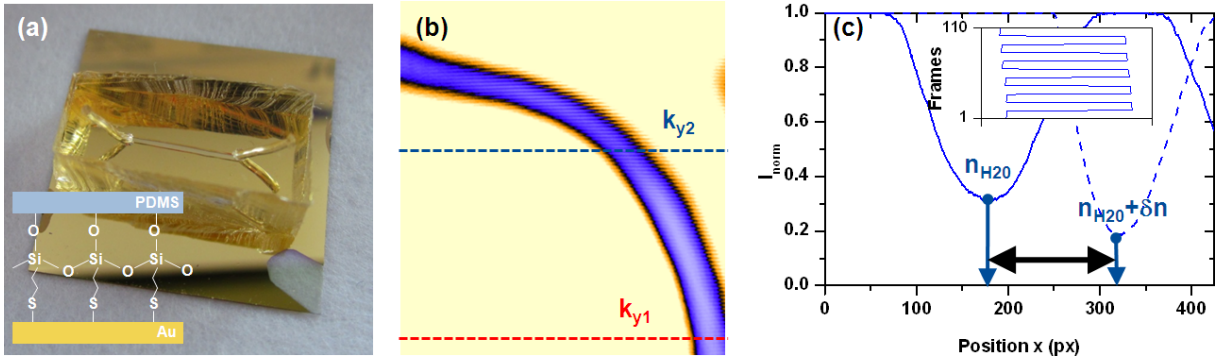

Figure 8.3.: (a) Sensing sample, encapsulated in a microfluidic cell. Binding of PDMS to gold by (3-Mercaptopropyl)trimethoxysilane is shown schematically in the inset. - (b) Zoom of the inner branch of the IFD around the M-point. The image is acquired by defocussing weakly the reciprocal space, and using an optical isolator in the illumination path. Operating points close to the bandgap (k_{y2}) and far off the bandgap (k_{y1}) are marked by dashed lines. - (c) Cross-sections of defocused LR images at k_{y2} as used for sensitivity evaluation. The profiles were taken in an ultra-pure water environment (solid line) and in a solution corresponding to a refractive index difference of $\delta n = 4.3 \times 10^{-3}$ RIU (dashed). The variation of detected peak centers x_j by iterative exchange of these liquids is shown in the inset.

Sensing in the magnified reciprocal space of an LR microscope was performed using the same configuration as in the previous chapter. Targeting low sensing noise levels, a Faraday optical isolator was introduced in the illumination beam path for the noise analysis and peak widths evaluation presented later in this chapter. It prevents back-reflections into the laser diode and thus increases the stability of the source. At the same time the beam expander was removed to increase the optical signal strength.

As can be seen from Fig. 8.1(b), simple reciprocal space LR images only provide weak contrast at the level of the SP bandgap. To overcome this limitation, defocused images of the reciprocal space were acquired. The resulting interference pattern contains a well defined first diffraction dip, following approximately the shape of the SP bandstructure. The image was further saturated around the minimum to reduce the dip width. A sample image is shown in Fig. 8.3(b).

This dip has been chosen as the refractive index probe for the presented sensing experiments. Cross-sections of the image were taken close to bandgap region (k_{y2}), and far off the bandgap (k_{y1}), as marked in Fig. 8.3(b). Vertical spatial averaging of 17 lines of the CCD around these operating points yielded profiles as the one depicted in Fig. 8.3(c). As straightforward scaling of the defocused images to reciprocal wavevector units was not possible, resonance shifts were measured in pixel units (px).

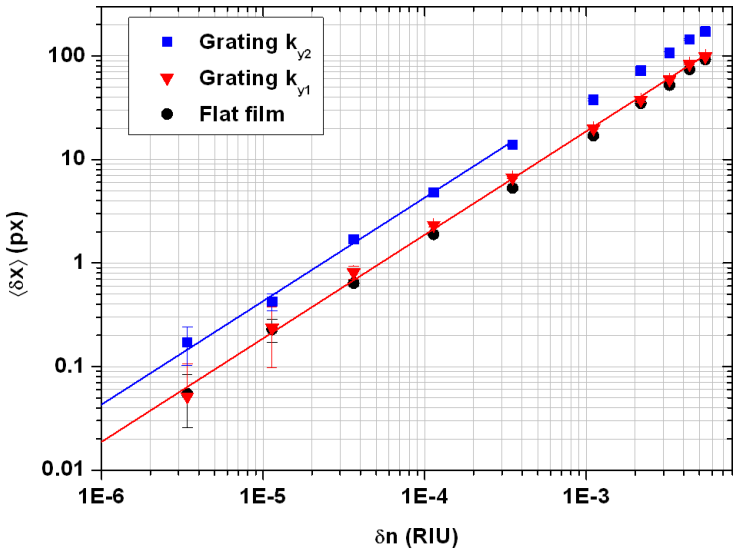

Figure 8.4.: Variation of peak centers $\langle \delta x \rangle$ as a function of refractive index difference δn, plotted in double-logarithmic scale. Data was acquired for aqueous solutions of ethanol with known refractive index on a 1PG close to the bandgap at k_{y2} (blue squares) and far off the bandgap at k_{y1} (red triangles) from defocused LR imaging (see Fig 8.3). Data acquired for standard LR sensing on a flat film is also shown (black circles). The data was fitted by linear regression (for k_{y2} only in the regime of linear response below $\delta n = 10^{-3}$). Sensitivities of $\delta x/\delta n = 43.0 \times 10^3$ px/RIU close to the bandgap (at k_{y2}), compared to 18.8×10^3 px/RIU at k_{y1}, and 16.6×10^3 px/RIU for a flat film were extracted.

A measure for the peak position was calculated by the centroid method [92]. The method is based on finding the geometric center of the dip as $x_j = \sum x_i (I_{\mathrm{th}} - I_i) / \sum (I_{\mathrm{th}} - I_i)$, while only including pixels i with intensity I_i below a specific intensity threshold I_{th} in the calculation. A threshold I_{th} of half the peak depth was chosen. The resulting values x_j were subsequently averaged temporally over $N = 10$ frames, yielding an average position value $\overline{x}_l$.

To probe the sensor sensitivity, the same aqueous solutions of ethanol as in the previous chapter were used as a refractive index reference, providing controlled refractive index differences to pure water ranging from $\delta n_{\mathrm{max}} = 5.4 \times 10^{-3}$ RIU to $\delta n_{\mathrm{min}} = 3.4 \times 10^{-6}$ RIU. For each of these solutions, the peak position was determined as described. Subsequently, the solution was referenced against pure water to compensate low-noise signal drift. A resulting temporal evolution of the measured peak-position is depicted in the inset of Fig. 8.3(c).

Refractive index differences were subsequently determined as $\delta x_j = (-1)^j (\overline{x}_j - 2\overline{x}_{j+1} + \overline{x}_{j+2})/2$, and averaged over $M = 10$ cycles, yielding $\langle \delta x \rangle$. Resulting values of $\langle \delta x \rangle$ from all solutions are depicted in Fig. 8.4 in logarithmic scale. Data for an operating point k_{y2}

close to the bandgap and for a point k_{y1} far off the bandgap are shown. For comparison, also results from a flat film of the same thickness are plotted. Slopes of the curves were extracted by fitting the logarithmic intensities over the range of linear response. Slopes of $\partial x/\partial n = 43.0\times10^3$ px/RIU at point k_{y2} close the M point, and $\partial x/\partial n = 18.8\times10^3$ px/RIU at point k_{y1} were found, corresponding to a more than twofold increase in sensitivity.

Full peak widths were measured at half the peak depth, and widths of $w_{\mathrm{ky2}} = 98.1$ px close to the bandgap compared to $w_{\mathrm{ky1}} = 82.3$ px in the flat band region at k_{y1} were observed. Together with the sensitivity enhancement, this results in figures of merit of FOM = 438 at k_{y2} and FOM = 228 at k_{y1}, corresponding to a more than 90% improvement. As both values were derived from the same images, only differing in the choice of operating point k_y, the potential of anisotropic bandstructures for improving SP sensing figures of merit is clearly demonstrated.

The observed increase and the reported figures of merit genuinely characterize the implemented sensing setup. Note, however, that both values are larger than the theoretically predicted ones. From the comparison of defocused data at k_{y1} to focused data from a flat gold film as given in Fig. 8.4, the sensitivity is observed to be not affected by the defocused image acquisition. The increase in FOM far from the bandgap must thus stem from a reduction of the peak width. We attribute this reduction to the chosen defocused image acquisition process. Indeed by working with dips instead of peaks, the detector can be saturated around the resonance, yielding an effective reduction of the dip width. The applied defocusing technique, which is conveniently accessible in the presented LR microscopy setup, could hence prove interesting for improving the peak quality also in conventional sensing configurations. The quantification of achievable improvements in such a scheme would require a thorough analysis, also taking into account effects of reduced peak depth and changes of the centroid threshold level. However, such an analysis goes beyond the scope of the study presented here.

It shall also be mentioned that, for the implemented sensing scheme, operation on the inner branch of the IFD around the M point was chosen, as the difference in loss characteristics between the two branches was not yet understood at the time the experiments were performed. Choosing operation points on the opposite branch is expected to yield even better figures of merit due to lower scattering loss (see chapter 5), leaving room for improvement of the setup.

8.3. Noise and Resolution

The practical performance of the implemented sensor was characterized by evaluation of the signal uncertainty $\sigma_{\langle \delta x \rangle}$ over 3×10^5 frames, as discussed in the previous section. For a liquid exchange time $\tau = 20$ s and the chosen averaging ranges $N = M = 10$, an uncertainty of $\sigma_{\langle \delta x \rangle} = 6.2 \times 10^{-2}$ px was determined at k_{y2}, corresponding to a resolution of $\sigma_{\langle \delta x \rangle}/S_{k2} = 1.4 \times 10^{-6}$. Neglecting liquid exchange times, $\sigma_{\langle \delta x \rangle} = 9.6 \times 10^{-3}$ was measured and thus $\sigma_{\langle \delta x \rangle}/S_{k2} = 2.2 \times 10^{-7}$ could be expected, comparable to the best systems reported to date [116].

8.4. Conclusions

High refractive index sensing on metal gratings was discussed in this chapter. Bandstructure anisotropy in such gratings was shown to lead to a more than twofold enhancement of the refractive index sensing sensitivity in such devices. Moreover, analysis of resonance widths revealed a resulting 90% increase in sensing figures of merit. By characterization of the signal uncertainty of the implemented optical setup, sensing resolutions on the order of 10^{-6} were reached in a high-resolution sensing experiment.

9 Summary and Outlook

A variety of advanced methods for controlling the flow of propagating surface plasmons was described in this thesis. Such control was put to use for the optomechanical micromanipulation of gold particles as well as two complementary ways of improving plasmon based refractive index sensing.

Dielectric and metallic surface optical components for the manipulation of propagating surface plasmon polaritons were presented. Conventional refractive optical elements such as prisms and lenses made from polymer on metal substrates were implemented for redirecting and focusing surface plasmon beams. The effective refractive index of such components was rendered tunable at will by the development of a metamaterial consisting of dielectric rods with subwavelength spacing. This novel material system was used to design gradient index optical elements. Moreover, scattering loss of SPs to the air light cone from device interfaces, which represents one of the most limiting factors of sharp-edged dielectric components, could be significantly reduced by smooth gradient transitions made from the developed metamaterial.

Diffractive optical phenomena in designed singly and doubly periodic sinusoidal metal gratings were discussed subsequently. The interaction of different diffraction orders led to regions of bandgaps in such structures. Such effects were exploited previously for a variety of applications, the most common being SP Bragg reflectors. By careful study of achievable gap-widths and related losses in such gratings, as well as by the fabrication of smooth gratings with tapered transitions, it was possible to design low-loss gratings leading to the demonstration of a plasmonic analogue of the superprism effect. The effect could be related to experimentally and theoretically revealed bandstructure anisotropy in the vicinity of the SP bandgap. Regions of operation could be identified which correspond to effective negative refraction of SP beams.

Using a similar design strategy, the curvature of isolated features in the SP bandstruture of two-dimensional gratings was additionally molded to result in flat isofrequency curves. Such flat bands were shown to lead to diffraction free propagation of SP beams over

unprecedented distances by a self-collimation effect.

Recent experiments on the propulsion of metal nanoparticles by plasmon near-fields [25] inspired us to use this newly achieved control of SP flow for optical micromanipulation. In a similar grating geometry, adapted for SPs in a water environment, steering and negative refraction of SP beams were applied for routing gold nanoparticles to a wide range of directions.

An advanced leakage radiation microscope was implemented in the laboratory as the central tool for the analysis of these plasmonic devices. To achieve the required control over launched SP fields, especially needed for SP steering experiments, a variety of spatial filtering techniques in the incident as well as in the imaging beam path of the microscope had to be implemented. SP imaging over multiple decay lengths could be rendered possible by high-dynamic range imaging techniques.

Leakage radiation microscopy was also introduced as a novel tool for refractive index sensing. The asymmetry of Fano resonances natural to SPs launched from nanoapertures was exploited to achieve increased sensing figures of merit in an intensity interrogation scheme. Additional features such as reciprocal space magnification and combined LR-ATR microscopy had to be included in the optical setup for this purpose.

Besides the optimization of resonance profiles, also molding of the SP dispersion relation itself was accomplished. The anisotropy of plasmonic bandstructures in metal gratings could be used to achieve a multiple increase of sensing sensitivities, and significant enhancement of sensing figures of merit.

The presented results may have some impact on future fundamental and applied plasmonics research. While the developed dielectric metamaterial system has already proven to limit SP scattering loss, it also allows designed lateral variation of the refractive index for SPs. This is the key ingredient for the fabrication of plasmon transformation optical components. A similar dielectric system using polymer components of varying height has thus been used recently for the design of Luneburg and Eaton lenses [54], and a discretized dielectric system made from TiO_2 has led to the design of a plasmonic cloak [212]. Considering the variety of transformation optical systems which have already been theoretically proposed [53, 213], such fabrication technologies are expected to lead to further experimental implementations in the near future.

Throughout this thesis an understanding of SP bandstructures has been developed, and dedicated design of SP bandstructures has been rendered possible. It has been shown how

such control can be applied for sensing and optical micromanipulation, and is expected to have further impact on the design of efficient metal optical devices. The presented approach on particle routing could also be developed further to permit sorting and guiding of metal nanoparticles on gratings. Furthermore, first steps have been already undertaken in the laboratory to explore bandstructure effects in plasmonic quasicrystal geometries. Such structures bear the potential for increasing the range of crystal geometries and extending its use to broadband devices.

As a result of continuous development, additions and improvements over the past years, a mature and versatile leakage radiation microscope is now at hand in the laboratory. The implemented possibility for polarization tomography has been applied in a first study for weak measurements of light chirality [149]. Further understanding of the vectorial nature of fields imaged by LR microscopy [141, 142], together with homogeneous or spatial control of the polarization of excited and imaged fields, could permit exploring effects such as, e.g., orbital angular momentum in plasmonic nanostrutures [146, 147, 214]. Expansion of the introduced binary spatial filters to the use of spatial light modulators bears moreover the potential to achieve complex SP excitation fields and additional degrees of control [47, 49].

The introduced sensing scheme based on a leakage radiation microscope should find use in the chemical and life sciences. LR microscopy allows sensing simultaneous to high-resolution imaging of events at the metal surface. Moreover, as a microscopy technique, it facilitates imaging of SPs propagating in all in-plane directions. This could be expected to be further exploited for parallelization of SP sensing in radial geometries, or alternatively, the contained two-dimensional reciprocal space information could be used for improving sensing noise figures and thus achievable resolutions.

Apart from their function as a controlled sensing environment, the developed microfluidic cells in combination with a high numerical aperture immersion objective may pave the way towards novel SP based optofluidic applications. On the one hand, plasmonic structures could be applied to adding new or improved functionalities to microfluidic circuits. On the other hand, it could be imagined to mold the flow of SP propagation by tunable and reconfigurable liquid dielectric devices. Also SP waveguides based on sharp as well as diffusive liquid-liquid interfaces could be envisaged.

Such a combination of understanding of devices, novel material systems and a set of mature methods in SP launching, imaging and the fabrication of nanostructures and controlled microfluidic environments may pave the way towards a variety of exciting novel insights and applications.

Bibliography

[1] E. Devaux, J.-Y. Laluet, B. Stein, C. Genet, T. Ebbesen, J.-C. Weeber, and A. Dereux. *Refractive micro-optical elements for surface plasmons: from classical to gradient index optics.* Opt. Express **18**, 20:20610–20619 (2010)

[2] B. Stein, J.-Y. Laluet, E. Devaux, C. Genet, and T. W. Ebbesen. *Surface plasmon mode steering and negative refraction.* Phys. Rev. Lett. **105**:266804 (2010)

[3] B. Stein, E. Devaux, C. Genet, and T. W. Ebbesen. *Self-collimation of surface plasmon beams.* Opt. Lett. **37**, 11:1916–1918 (2012)

[4] A. Cuche, B. Stein, A. Canaguier-Durand, E. Devaux, C. Genet, and T. W. Ebbesen. *Brownian motion in a designer force field: dynamical effects of negative refraction on nanoparticles.* Nano Lett. **12**, 8:4329–4332 (2012)

[5] B. Stein, J.-Y. Laluet, E. Devaux, C. Genet, and T. W. Ebbesen. *Fano resonances and leakage radiation for high-resolution plasmonic sensing.* J. Phys. Chem. C **116**, 10:6092–6096 (2012)

[6] P. B. Johnson and R. W. Christy. *Optical constants of the noble metals.* Phys. Rev. B **6**, 12:4370–4379 (1972)

[7] C. Kittel. *Introduction to solid state physics.* Wiley, New York, 8 ed. (2005)

[8] N. D. Ashcroft, Neil W. ; Mermin. *Solid state physics.* Brooks/Coole Cengage Learning, Belmont, CA (2009)

[9] L. Novotny and B. Hecht. *Principles of nano-optics.* Cambridge University Press, 1 ed. (2007)

[10] S. Hunklinger. *Festkörperphysik.* Oldenbourg (2007)

[11] P. Drude. *Zur Elektronentheorie der Metalle.* Ann. Phys. **306**, 3:566–613 (1900)

[12] J. B. Smith and H. Ehrenreich. *Frequency dependence of the optical relaxation time in metals.* Phys. Rev. B **25**:923–930 (1982)

[13] A. Sommerfeld. *Zur Elektronentheorie der Metalle auf Grund der Fermischen Statistik.* Z. Phys. A-Hadron. Nucl. **47**:1–32 (1928)

[14] M. Guerrisi, R. Rosei, and P. Winsemius. *Splitting of the interband absorption edge in Au.* Phys. Rev. B **12**:557–563 (1975)

[15] A. Taflove and S. C. Hagness. *Computational Electrodynamics: The Finite-Difference*

Time-Domain Method. Artech House, Inc., 3 ed. (2005)

[16] A. Vial, A.-S. Grimault, D. Macias, D. Barchiesi, and M. L. de la Chapelle. *Improved analytical fit of gold dispersion: Application to the modeling of extinction spectra with a finite-difference time-domain method*. Phys. Rev. B **71**:085416 (2005)

[17] M. A. Ordal, L. L. Long, R. J. Bell, S. E. Bell, R. R. Bell, J. R. W. Alexander, and C. A. Ward. *Optical properties of the metals Al, Co, Cu, Au, Fe, Pb, Ni, Pd, Pt, Ag, Ti, and W in the infrared and far infrared*. Appl. Opt. **22**, 7:1099–1119 (1983)

[18] H. Raether. *Surface plasmons on smooth and rough surfaces and on gratings*, vol. 111 of *Springer tracts in modern physics*. Springer, Berlin (1988)

[19] G. I. Stegeman, J. J. Burke, and D. G. Hall. *Surface-polaritonlike waves guided by thin, lossy metal films*. Opt. Lett. **8**, 7:383–385 (1983)

[20] J. J. Burke, G. I. Stegeman, and T. Tamir. *Surface-polariton-like waves guided by thin, lossy metal films*. Phys. Rev. B **33**:5186–5201 (1986)

[21] A. Drezet, A. Hohenau, D. Koller, A. Stepanov, H. Ditlbacher, B. Steinberger, F. Aussenegg, A. Leitner, and J. Krenn. *Leakage radiation microscopy of surface plasmon polaritons*. Mat. Sci. Eng. B-Solid **149**, 3:220 – 229 (2008)

[22] D. Sarid. *Long-range surface-plasma waves on very thin metal films*. Phys. Rev. Lett. **47**:1927–1930 (1981)

[23] P. Berini. *Long-range surface plasmon polaritons*. Adv. Opt. Photon. **1**, 3:484–588 (2009)

[24] J. G. II and S. Ernst. *Surface plasmons as a probe of the electrochemical interface*. Surf. Sci. **101**:499 – 506 (1980)

[25] K. Wang, E. Schonbrun, and K. B. Crozier. *Propulsion of gold nanoparticles with surface plasmon polaritons: Evidence of enhanced optical force from near-field coupling between gold particle and gold film*. Nano Lett. **9**, 7:2623–2629 (2009)

[26] K. Wang, E. Schonbrun, P. Steinvurzel, and K. B. Crozier. *Scannable plasmonic trapping using a gold stripe*. Nano Lett. **10**, 9:3506–3511 (2010)

[27] S. A. Maier, M. D. Friedman, P. E. Barclay, and O. Painter. *Experimental demonstration of fiber-accessible metal nanoparticle plasmon waveguides for planar energy guiding and sensing*. Appl. Phys. Lett. **86**, 7:071103 (2005)

[28] B. Hecht, H. Bielefeldt, L. Novotny, Y. Inouye, and D. W. Pohl. *Local excitation, scattering, and interference of surface plasmons*. Phys. Rev. Lett. **77**:1889–1892 (1996)

[29] J. Renger, R. Quidant, N. van Hulst, S. Palomba, and L. Novotny. *Free-space excitation of propagating surface plasmon polaritons by nonlinear four-wave mixing*. Phys. Rev. Lett. **103**:266802 (2009)

[30] G. I. Stegeman, R. F. Wallis, and A. A. Maradudin. *Excitation of surface polaritons*

by end-fire coupling. Opt. Lett. **8**, 7:386–388 (1983)

[31] C. J. Powell and J. B. Swan. *Effect of oxidation on the characteristic loss spectra of aluminum and magnesium.* Phys. Rev. **118**:640–643 (1960)

[32] D. M. Koller, A. Hohenau, H. Ditlbacher, N. Galler, F. Reil, F. R. Aussenegg, A. Leitner, E. J. W. List, and J. R. Krenn. *Organic plasmon-emitting diode.* Nat. Phot. **2**:684–687 (2008)

[33] P. Berini and I. D. Leon. *Surface plasmon polariton amplifiers and lasers.* Nat. Phot. **6**:16–24 (2012)

[34] E. Kretschmann and H. Raether. *Radiative decay of non-radiative surface plasmons excited by light.* Z. Naturforsch. A **23**, 23:2135 (1968)

[35] A. Otto. *Excitation of nonradiative surface plasma waves in silver by the method of frustrated total reflection.* Z. Phys. A-Hadron. Nucl. **216**:398–410 (1968)

[36] E. Devaux, T. W. Ebbesen, J.-C. Weeber, and A. Dereux. *Launching and decoupling surface plasmons via micro-gratings.* Appl. Phys. Lett. **83**, 24:4936–4938 (2003)

[37] A. Archambault, T. V. Teperik, F. Marquier, and J. J. Greffet. *Surface plasmon Fourier optics.* Phys. Rev. B **79**:195414 (2009)

[38] J.-Y. Laluet, E. Devaux, C. Genet, T. W. Ebbesen, J.-C. Weeber, and A. Dereux. *Optimization of surface plasmons launching from subwavelength hole arrays: modelling and experiments.* Opt. Express **15**, 6:3488–3495 (2007)

[39] T. V. Teperik, A. Archambault, F. Marquier, and J. J. Greffet. *Huygens-Fresnel principle for surface plasmons.* Opt. Express **17**, 20:17483–17490 (2009)

[40] H. Ditlbacher, J. R. Krenn, N. Felidj, B. Lamprecht, G. Schider, M. Salerno, A. Leitner, and F. R. Aussenegg. *Fluorescence imaging of surface plasmon fields.* Appl. Phys. Lett. **80**, 3:404–406 (2002)

[41] J.-Y. Laluet, A. Drezet, C. Genet, and T. W. Ebbesen. *Generation of surface plasmons at single subwavelength slits: from slit to ridge plasmon.* New J. Phys. **10**, 10:105014 (2008)

[42] J. W. Goodman. *Introduction to Fourier optics.* Roberts, Englewood, Colo., 3. ed. ed. (2005)

[43] L. Yin, V. K. Vlasko-Vlasov, J. Pearson, J. M. Hiller, J. Hua, U. Welp, D. E. Brown, and C. W. Kimball. *Subwavelength focusing and guiding of surface plasmons.* Nano Lett. **5**, 7:1399–1402 (2005)

[44] C. Zhao and J. Zhang. *Binary plasmonics: launching surface plasmon polaritons to a desired pattern.* Opt. Lett. **34**, 16:2417–2419 (2009)

[45] W. Zhang, C. Zhao, J. Wang, and J. Zhang. *An experimental study of the plasmonic talbot effect.* Opt. Express **17**, 22:19757–19762 (2009)

[46] A. Minovich, A. E. Klein, N. Janunts, T. Pertsch, D. N. Neshev, and Y. S. Kivshar. *Generation and near-field imaging of Airy surface plasmons.* Phys. Rev. Lett. **107**:116802 (2011)

[47] B. Gjonaj, J. Aulbach, P. M. Johnson, A. P. Mosk, L. Kuipers, and A. Lagendijk. *Active spatial control of plasmonic fields.* Nat. Phot. **5**:360–363 (2011)

[48] P. Zhang, S. Wang, Y. Liu, X. Yin, C. Lu, Z. Chen, and X. Zhang. *Plasmonic Airy beams with dynamically controlled trajectories.* Opt. Lett. **36**, 16:3191–3193 (2011)

[49] B. Gjonaj, J. Aulbach, P. M. Johnson, A. P. Mosk, L. Kuipers, and A. Lagendijk. *Optical control of plasmonic Bloch modes on periodic nanostructures.* Nano Lett. **12**, 2:546–550 (2012)

[50] T. W. Ebbesen, C. Genet, and S. I. Bozhevolnyi. *Surface-plasmon circuitry.* Phys. Today **61**, 5:44–50 (2008)

[51] S. Bozhevolnyi. *Plasmonic nanoguides and circuits.* Pan Stanford (2008)

[52] A. Hohenau, J. R. Krenn, A. L. Stepanov, A. Drezet, H. Ditlbacher, B. Steinberger, A. Leitner, and F. R. Aussenegg. *Dielectric optical elements for surface plasmons.* Opt. Lett. **30**, 8:893–895 (2005)

[53] Y. Liu, T. Zentgraf, G. Bartal, and X. Zhang. *Transformational plasmon optics.* Nano Lett. **10**, 6:1991–1997 (2010)

[54] T. Zentgraf, Y. Liu, M. H. Mikkelsen, J. Valentine, and X. Zhang. *Plasmonic Luneburg and Eaton lenses.* Nat. Nanotech. (2011)

[55] H. J. Lezec, J. A. Dionne, and H. A. Atwater. *Negative refraction at visible frequencies.* Science **316**, 5823:430–432 (2007)

[56] L. Novotny, B. Hecht, and D. W. Pohl. *Interference of locally excited surface plasmons.* J. Appl. Phys. **81**, 4:1798–1806 (1997)

[57] H. Ditlbacher, J. R. Krenn, G. Schider, A. Leitner, and F. R. Aussenegg. *Two-dimensional optics with surface plasmon polaritons.* Appl. Phys. Lett. **81**, 10:1762–1764 (2002)

[58] A. Drezet, A. L. Stepanov, H. Ditlbacher, A. Hohenau, B. Steinberger, F. R. Aussenegg, A. Leitner, and J. R. Krenn. *Surface plasmon propagation in an elliptical corral.* Appl. Phys. Lett. **86**, 7:074104 (2005)

[59] Z.-W. Liu, Q.-H. Wei, and X. Zhang. *Surface plasmon interference nanolithography.* Nano Lett. **5**, 5:957–961 (2005)

[60] L. Feng, K. A. Tetz, B. Slutsky, V. Lomakin, and Y. Fainman. *Fourier plasmonics: Diffractive focusing of in-plane surface plasmon polariton waves.* Appl. Phys. Lett. **91**, 8:081101 (2007)

[61] S. C. Kitson, W. L. Barnes, and J. R. Sambles. *Full photonic band gap for surface modes in the visible.* Phys. Rev. Lett. **77**:2670–2673 (1996)

[62] M. U. González, J.-C. Weeber, A.-L. Baudrion, A. Dereux, A. L. Stepanov, J. R. Krenn, E. Devaux, and T. W. Ebbesen. *Design, near-field characterization, and modeling of surface-plasmon Bragg mirrors.* Phys. Rev. B **73**:155416 (2006)

[63] M. U. González, A. L. Stepanov, J.-C. Weeber, A. Hohenau, A. Dereux, R. Quidant, and J. R. Krenn. *Analysis of the angular acceptance of surface plasmon Bragg mirrors.* Opt. Lett. **32**, 18:2704–2706 (2007)

[64] S. I. Bozhevolnyi, J. Erland, K. Leosson, P. M. W. Skovgaard, and J. M. Hvam. *Waveguiding in surface plasmon polariton band gap structures.* Phys. Rev. Lett. **86**:3008–3011 (2001)

[65] A. Drezet, D. Koller, A. Hohenau, A. Leitner, F. R. Aussenegg, and J. R. Krenn. *Plasmonic crystal demultiplexer and multiports.* Nano Lett. **7**, 6:1697–1700 (2007)

[66] M. Sandtke and L. Kuipers. *Slow guided surface plasmons at telecom frequencies.* Nat. Phot. **1**:573–576 (2007)

[67] A. Drezet, D. Koller, A. Hohenau, A. Leitner, F. R. Aussenegg, and J. R. Krenn. *Surface plasmon polariton microscope with parabolic reflectors.* Opt. Lett. **32**, 16:2414–2416 (2007)

[68] L. Li, T. Li, S. Wang, S. Zhu, and X. Zhang. *Broad band focusing and demultiplexing of in-plane propagating surface plasmons.* Nano Lett. **11**, 10:4357–4361 (2011)

[69] L. Li, T. Li, S. M. Wang, C. Zhang, and S. N. Zhu. *Plasmonic Airy beam generated by in-plane diffraction.* Phys. Rev. Lett. **107**:126804 (2011)

[70] Y.-J. Tsai, A. Degiron, N. M. Jokerst, and D. R. Smith. *Plasmonic multi-mode interference couplers.* Opt. Express **17**, 20:17471–17482 (2009)

[71] J. Dintinger, I. Robel, P. Kamat, C. Genet, and T. Ebbesen. *Terahertz all-optical molecule-plasmon modulation.* Adv. Mater. **18**, 13:1645–1648 (2006)

[72] O. Solgaard, F. Ho, J. I. Thackara, and D. M. Bloom. *High frequency attenuated total internal reflection light modulator.* Appl. Phys. Lett. **61**, 21:2500–2502 (1992)

[73] M. J. Dicken, L. A. Sweatlock, D. Pacifici, H. J. Lezec, K. Bhattacharya, and H. A. Atwater. *Electrooptic modulation in thin film barium titanate plasmonic interferometers.* Nano Lett. **8**, 11:4048–4052 (2008)

[74] K. F. MacDonald, Z. L. Sámson, M. I. Stockman, and N. I. Zheludev. *Ultrafast active plasmonics.* Nat. Phot. **3**:55–58 (2009)

[75] D. Pacifici, H. J. Lezec, and H. A. Atwater. *All-optical modulation by plasmonic excitation of CdSe quantum dots.* Nat. Phot. **1**:402–406 (2007)

[76] R. A. Pala, K. T. Shimizu, N. A. Melosh, and M. L. Brongersma. *A nonvolatile plasmonic switch employing photochromic molecules.* Nano Lett. **8**, 5:1506–1510 (2008)

[77] J. Seidel, S. Grafström, and L. Eng. *Stimulated emission of surface plasmons at*

the interface between a silver film and an optically pumped dye solution. Phys. Rev. Lett. **94**:177401 (2005)

[78] M. A. Noginov, V. A. Podolskiy, G. Zhu, M. Mayy, M. Bahoura, J. A. Adegoke, B. A. Ritzo, and K. Reynolds. *Compensation of loss in propagating surface plasmon polariton by gain in adjacent dielectric medium.* Opt. Express **16**, 2:1385–1392 (2008)

[79] P. Bolger, W. Dickson, A. Krasavin, L. Liebscher, S. Hickey, D. Skryabin, and A. Zayats. *Amplified spontaneous emission of surface plasmon polaritons and limitations on the increase of their propagation length.* Opt. Lett. **35**, 8:1197–1199 (2010)

[80] K. MacDonald and N. Zheludev. *Active plasmonics: current status.* Laser & Photon. Rev. **4**, 4:562–567 (2010)

[81] D. K. Gramotnev and S. I. Bozhevolnyi. *Plasmonics beyond the diffraction limit.* Nat. Phot. **4**:83–91 (2010)

[82] B. Steinberger, A. Hohenau, H. Ditlbacher, A. L. Stepanov, A. Drezet, F. R. Aussenegg, A. Leitner, and J. R. Krenn. *Dielectric stripes on gold as surface plasmon waveguides.* Appl. Phys. Lett. **88**, 9:094104 (2006)

[83] J.-C. Weeber, J. R. Krenn, A. Dereux, B. Lamprecht, Y. Lacroute, and J. P. Goudonnet. *Near-field observation of surface plasmon polariton propagation on thin metal stripes.* Phys. Rev. B **64**:045411 (2001)

[84] P. Berini. *Plasmon-polariton waves guided by thin lossy metal films of finite width: Bound modes of symmetric structures.* Phys. Rev. B **61**:10484–10503 (2000)

[85] A. Boltasseva, T. Nikolajsen, K. Leosson, K. Kjaer, M. Larsen, and S. Bozhevolnyi. *Integrated optical components utilizing long-range surface plasmon polaritons.* J. Lightwave Technol. **23**, 1:413 –422 (2005)

[86] V. S. Volkov, Z. Han, M. G. Nielsen, K. Leosson, H. Keshmiri, J. Gosciniak, O. Albrektsen, and S. I. Bozhevolnyi. *Long-range dielectric-loaded surface plasmon polariton waveguides operating at telecommunication wavelengths.* Opt. Lett. **36**, 21:4278–4280 (2011)

[87] S. I. Bozhevolnyi, V. S. Volkov, E. Devaux, and T. W. Ebbesen. *Channel plasmon-polariton guiding by subwavelength metal grooves.* Phys. Rev. Lett. **95**:046802 (2005)

[88] S. I. Bozhevolnyi, V. S. Volkov, E. Devaux, J.-Y. Laluet, and T. W. Ebbesen. *Channel plasmon subwavelength waveguide components including interferometers and ring resonators.* Nature **440**:508–511 (2006)

[89] E. Zubritsky. *Product review: New choices for SPR.* Anal. Chem. **72**, 7:289 A–292 A (2000)

[90] E. Abbe. *Neue Apparate zur Bestimmung des Brechungs- und Zerstreuungsvermögens fester und flüssiger Körper.* Mauke's Verlag (Hermann Dufft) (1874)

[91] P. Grosso, D. Malarde, M. L. Menn, Z. Wu, and J.-L. de Bougrenet de la Tocnaye.

Refractometer resolution limits for measuring seawater refractive index. Opt. Eng. **49**, 10:103603 (2010)

[92] J. Homola. *Surface plasmon resonance based sensors.* Springer, Dordrecht (2006)

[93] P. Englebienne. *Use of colloidal gold surface plasmon resonance peak shift to infer affinity constants from the interactions between protein antigens and antibodies specific for single or multiple epitopes.* Analyst **123**:1599–1603 (1998)

[94] A. J. Haes and R. P. Van Duyne. *A nanoscale optical biosensor: Sensitivity and selectivity of an approach based on the localized surface plasmon resonance spectroscopy of triangular silver nanoparticles.* J. Am. Chem. Soc. **124**, 35:10596–10604 (2002)

[95] J. J. Mock, D. R. Smith, and S. Schultz. *Local refractive index dependence of plasmon resonance spectra from individual nanoparticles.* Nano Lett. **3**, 4:485–491 (2003)

[96] L. R. Hirsch, J. B. Jackson, A. Lee, N. J. Halas, and J. L. West. *A whole blood immunoassay using gold nanoshells.* Anal. Chem. **75**, 10:2377–2381 (2003)

[97] T. Rindzevicius, Y. Alaverdyan, A. Dahlin, F. Höök, D. S. Sutherland, and M. Käll. *Plasmonic sensing characteristics of single nanometric holes.* Nano Lett. **5**, 11:2335–2339 (2005)

[98] M. Svedendahl, S. Chen, A. Dmitriev, and M. Käll. *Refractometric sensing using propagating versus localized surface plasmons: A direct comparison.* Nano Lett. **9**, 12:4428–4433 (2009)

[99] L. Zhang and D. Uttamchandani. *Optical chemical sensing employing surface plasmon resonance.* Electron. Lett. **24**, 23:1469 –1470 (1988)

[100] K. Matsubara, S. Kawata, and S. Minami. *Optical chemical sensor based on surface plasmon measurement.* Appl. Opt. **27**, 6:1160–1163 (1988)

[101] C. Nylander, B. Liedberg, and T. Lind. *Gas detection by means of surface plasmon resonance.* Sensor Actuator **3**:79 – 88 (1982-1983)

[102] J. Brockman, B. Nelson, and R. Corn. *Surface plasmon resonance imaging measurements of ultrathin organic films.* Annu. Rev. Phys. Chem. **51**:41–63 (2000)

[103] A. A. Kruchinin and Y. G. Vlasov. *Surface plasmon resonance monitoring by means of polarization state measurement in reflected light as the basis of a DNA-probe biosensor.* Sensor Actuat. B **30**, 1:77 – 80 (1996)

[104] B. Ran and S. G. Lipson. *Comparison between sensitivities of phase and intensity detection in surface plasmon resonance.* Opt. Express **14**, 12:5641–5650 (2006)

[105] M. Jory, P. Vukusic, and J. Sambles. *Development of a prototype gas sensor using surface plasmon resonance on gratings.* Sensor Actuat. B **17**, 3:203 – 209 (1994)

[106] R. Jorgenson and S. Yee. *A fiber-optic chemical sensor based on surface plasmon resonance.* Sensor Actuat. B **12**, 3:213 – 220 (1993)

[107] C. Lavers and J. Wilkinson. *A waveguide-coupled surface-plasmon sensor for an aqueous environment.* Sensor Actuat. B **22**, 1:75 – 81 (1994)

[108] H. Q. Zhang, S. Boussaad, and N. J. Tao. *High-performance differential surface plasmon resonance sensor using quadrant cell photodetector.* Rev. Sci. Instrum. **74**, 1:150–153 (2003)

[109] G. Nenninger, P. Tobiska, J. Homola, and S. Yee. *Long-range surface plasmons for high-resolution surface plasmon resonance sensors.* Sensor Actuat. B **74**:145 – 151 (2001). Proceedings of the 5th European Conference on Optical Chemical Sensors and Biosensors

[110] J. Homola, H. Vaisocherová, J. Dostálek, and M. Piliarik. *Multi-analyte surface plasmon resonance biosensing.* Methods **37**, 1:26 – 36 (2005)

[111] B. Rothenhäusler and W. Knoll. *Surface-plasmon microscopy.* Nature **332**:615–617 (1988)

[112] N. Bassil, E. Maillart, M. Canva, Y. Lévy, M.-C. Millot, S. Pissard, R. Narwa, and M. Goossens. *One hundred spots parallel monitoring of DNA interactions by SPR imaging of polymer-functionalized surfaces applied to the detection of cystic fibrosis mutations.* Sensor Actuat. B **94**, 3:313 – 323 (2003)

[113] M. Piliarik, H. Vaisocherová, and J. Homola. *A new surface plasmon resonance sensor for high-throughput screening applications.* Biosens. Bioelectron. **20**, 10:2104 – 2110 (2005)

[114] H. Kano and W. Knoll. *Locally excited surface-plasmon-polaritons for thickness measurement of LBK films.* Opt. Commun. **153**:235 – 239 (1998)

[115] H. Kano and W. Knoll. *A scanning microscope employing localized surface-plasmon-polaritons as a sensing probe.* Opt. Commun. **182**:11 – 15 (2000)

[116] M. Piliarik and J. Homola. *Surface plasmon resonance (SPR) sensors: approaching their limits?* Opt. Express **17**, 19:16505–16517 (2009)

[117] I. P. Kaminow, W. L. Mammel, and H. P. Weber. *Metal-clad optical waveguides: Analytical and experimental study.* Appl. Opt. **13**, 2:396–405 (1974)

[118] D. W. Pohl, W. Denk, and M. Lanz. *Optical stethoscopy: Image recording with resolution lambda/20.* Appl. Phys. Lett. **44**, 7:651–653 (1984)

[119] B. Hecht, B. Sick, U. P. Wild, V. Deckert, R. Zenobi, O. J. F. Martin, and D. W. Pohl. *Scanning near-field optical microscopy with aperture probes: Fundamentals and applications.* J. Chem Phys. **112**, 18:7761–7774 (2000)

[120] M. Ashino and M. Ohtsu. *Fabrication and evaluation of a localized plasmon resonance probe for near-field optical microscopy/spectroscopy.* Applied Physics Letters **72**, 11:1299–1301 (1998)

[121] T. Kalkbrenner, M. Ramstein, J. Mlynek, and V. Sandoghdar. *A single gold particle*

as a probe for apertureless scanning near-field optical microscopy. J. Microsc. **202**, 1:72–76 (2001)

[122] J. Michaelis, C. Hettich, J. Mlynek, and V. Sandoghdar. *Optical microscopy using a single-molecule light source.* Nature **405**:325–328 (2000)

[123] A. Lewis, M. Isaacson, A. Harootunian, and A. Muray. *Development of a 500 Å spatial resolution light microscope: I. light is efficiently transmitted through lambda/16 diameter apertures.* Ultramicroscopy **13**, 3:227 – 231 (1984)

[124] U. C. Fischer and D. W. Pohl. *Observation of single-particle plasmons by near-field optical microscopy.* Phys. Rev. Lett. **62**:458–461 (1989)

[125] O. Marti, H. Bielefeldt, B. Hecht, S. Herminghaus, P. Leiderer, and J. Mlynek. *Near-field optical measurement of the surface plasmon field.* Opt. Commun. **96**:225 – 228 (1993)

[126] P. Dawson, F. de Fornel, and J.-P. Goudonnet. *Imaging of surface plasmon propagation and edge interaction using a photon scanning tunneling microscope.* Phys. Rev. Lett. **72**:2927–2930 (1994)

[127] M. Sandtke, R. J. P. Engelen, H. Schoenmaker, I. Attema, H. Dekker, I. Cerjak, J. P. Korterik, F. B. Segerink, and L. Kuipers. *Novel instrument for surface plasmon polariton tracking in space and time.* Rev. Sci. Instrum. **79**, 1:013704 (2008)

[128] M. L. M. Balistreri, H. Gersen, J. P. Korterik, L. Kuipers, and N. F. van Hulst. *Tracking femtosecond laser pulses in space and time.* Science **294**, 5544:1080–1082 (2001)

[129] M. L. M. Balistreri, J. P. Korterik, L. Kuipers, and N. F. van Hulst. *Local observations of phase singularities in optical fields in waveguide structures.* Phys. Rev. Lett. **85**:294–297 (2000)

[130] E. Devaux, A. Dereux, E. Bourillot, J.-C. Weeber, Y. Lacroute, J.-P. Goudonnet, and C. Girard. *Local detection of the optical magnetic field in the near zone of dielectric samples.* Phys. Rev. B **62**:10504–10514 (2000)

[131] M. Burresi, D. van Oosten, T. Kampfrath, H. Schoenmaker, R. Heideman, A. Leinse, and L. Kuipers. *Probing the magnetic field of light at optical frequencies.* Science **326**, 5952:550–553 (2009)

[132] P. Mühlschlegel, H.-J. Eisler, O. J. F. Martin, D. Pohl, and B. Hecht. *Resonant optical antennas.* Science **308**:1607–1609 (2005)

[133] P. Biagioni, J.-S. Huang, and B. Hecht. *Nanoantennas for visible and infrared radiation.* Rep. Prog. Phys. **75**, 2:024402 (2012)

[134] I. I. Smolyaninov, D. L. Mazzoni, and C. C. Davis. *Imaging of surface plasmon scattering by lithographically created individual surface defects.* Phys. Rev. Lett. **77**:3877–3880 (1996)

[135] S. Schultz, D. R. Smith, J. J. Mock, and D. A. Schultz. *Single-target molecule detection with nonbleaching multicolor optical immunolabels.* PNAS **97**, 3:996–1001 (2000)

[136] K. Lindfors, T. Kalkbrenner, P. Stoller, and V. Sandoghdar. *Detection and spectroscopy of gold nanoparticles using supercontinuum white light confocal microscopy.* Phys. Rev. Lett. **93**:037401 (2004)

[137] S. Enoch and N. Bonod. *Plasmonics: from basics to advanced topics*, vol. 167 of *Springer Series in Optical Sciences.* Springer Verlag (2012)

[138] H. Simon and J. Guha. *Directional surface plasmon scattering from silver films.* Opt. Commun. **18**:391 – 394 (1976)

[139] A. Giannattasio and W. Barnes. *Direct observation of surface plasmon-polariton dispersion.* Opt. Express **13**, 2:428–434 (2005)

[140] S. Massenot, J. Grandidier, A. Bouhelier, G. C. des Francs, L. Markey, J.-C. Weeber, A. Dereux, J. Renger, M. U. Gonzalez, and R. Quidant. *Polymer-metal waveguides characterization by Fourier plane leakage radiation microscopy.* Appl. Phys. Lett. **91**, 24:243102 (2007)

[141] A. Hohenau, J. R. Krenn, A. Drezet, O. Mollet, S. Huant, C. Genet, B. Stein, and T. W. Ebbesen. *Surface plasmon leakage radiation microscopy at the diffraction limit.* Opt. Express **19**, 25:25749–25762 (2011)

[142] J. Wang, C. Zhao, and J. Zhang. *Does the leakage radiation profile mirror the intensity profile of surface plasmon polaritons?* Opt. Lett. **35**, 12:1944–1946 (2010)

[143] A. Drezet, A. Hohenau, A. L. Stepanov, H. Ditlbacher, B. Steinberger, N. Galler, F. R. Aussenegg, A. Leitner, and J. R. Krenn. *How to erase surface plasmon fringes.* Appl. Phys. Lett. **89**, 9:091117 (2006)

[144] E. Altewischer, M. P. van Exter, and J. P. Woerdman. *Polarization analysis of propagating surface plasmons in a subwavelength hole array.* J. Opt. Soc. Am. B **20**, 9:1927–1931 (2003)

[145] K. A. Tetz, R. Rokitski, M. Nezhad, and Y. Fainman. *Excitation and direct imaging of surface plasmon polariton modes in a two-dimensional grating.* Appl. Phys. Lett. **86**, 11:111110 (2005)

[146] Y. Gorodetski, A. Niv, V. Kleiner, and E. Hasman. *Observation of the spin-based plasmonic effect in nanoscale structures.* Phys. Rev. Lett. **101**:043903 (2008)

[147] Y. Gorodetski, N. Shitrit, I. Bretner, V. Kleiner, and E. Hasman. *Observation of optical spin symmetry breaking in nanoapertures.* Nano Lett. **9**, 8:3016–3019 (2009)

[148] O. Hosten and P. Kwiat. *Observation of the spin hall effect of light via weak measurements.* Science **319**, 5864:787–790 (2008)

[149] Y. Gorodetski, K. Y. Bliokh, B. Stein, C. Genet, N. Shitrit, V. Kleiner, E. Hasman,

and T. W. Ebbesen. *Weak measurements of light chirality with a plasmonic slit.* Phys. Rev. Lett. **109**:013901 (2012)

[150] J. Janesick. *Scientific charge-coupled devices.* SPIE Press monograph. SPIE Press (2001)

[151] A. E. Gamal. *High dynamic range image sensors.* In *Tutorial at International Solid-State Circuits Conference* (2002)

[152] D. G. Zhang, X.-C. L. Yuan, J. Bu, G. H. Yuan, Q. Wang, J. Lin, X. J. Zhang, P. Wang, H. Ming, and T. Mei. *Surface plasmon converging and diverging properties modulated by polymer refractive structures on metal films.* Opt. Express **17**, 14:11315–11320 (2009)

[153] J. Dintinger, S. Klein, and T. Ebbesen. *Molecule surface plasmon interactions in hole arrays: Enhanced absorption, refractive index changes, and all-optical switching.* Adv. Mater. **18**, 10:1267–1270 (2006)

[154] J. Grandidier, G. Colas des Francs, S. Massenot, A. Bouhelier, L. Markey, J.-C. Weeber, C. Finot, and A. Dereux. *Gain-assisted propagation in a plasmonic waveguide at telecom wavelength.* Nano Lett. **9**, 8:2935–2939 (2009)

[155] P. Rai-Choudhury. *Handbook of microlithography, micromachining, and microfabrication.* SPIE Optical Engineering Press ; Institution of Electrical Engineers (1997)

[156] E. Hecht. *Optics.* Addison-Wesley, 4. ed. (2002). International Edition

[157] S. Massenot, J.-C. Weeber, A. Bouhelier, G. C. des Francs, J. Grandidier, L. Markey, and A. Dereux. *Differential method for modeling dielectric-loaded surface plasmon polariton waveguides.* Opt. Express **16**, 22:17599–17608 (2008)

[158] M. Nevière and E. Popov. *Light propagation in periodic media: differential theory and design.* Optical engineering. Marcel Dekker (2003)

[159] I. P. Radko, A. B. Evlyukhin, A. Boltasseva, and S. I. Bozhevolnyi. *Refracting surface plasmon polaritons with nanoparticle arrays.* Opt. Express **16**, 6:3924–3930 (2008)

[160] C. Gomez-Reino, M. Perez, and C. Bao. *Gradient-index optics: fundamentals and applications.* Springer (2002)

[161] E. Yablonovitch. *Inhibited spontaneous emission in solid-state physics and electronics.* Phys. Rev. Lett. **58**:2059–2062 (1987)

[162] J. Joannopoulos, S. Johnson, J. Winn, and R. Meade. *Photonic crystals: molding the flow of light.* Princeton University Press, 2 ed. (2008)

[163] V. Mikhailov, G. A. Wurtz, J. Elliott, P. Bayvel, and A. V. Zayats. *Dispersing light with surface plasmon polaritonic crystals.* Phys. Rev. Lett. **99**:083901 (2007)

[164] R. Zengerle. *Lichtausbreitung in ebenen periodischen Wellenleitern.* Ph.D. thesis,

Universität Stuttgart (1979)

[165] P. S. J. Russell. *Interference of integrated Floquet-Bloch waves.* Phys. Rev. A **33**:3232–3242 (1986)

[166] R. Zengerle. *Light propagation in singly and doubly periodic planar waveguides.* J. Mod. Opt. **34**, 12:1589–1617 (1987)

[167] H. Kosaka, T. Kawashima, A. Tomita, M. Notomi, T. Tamamura, T. Sato, and S. Kawakami. *Superprism phenomena in photonic crystals.* Phys. Rev. B **58**:R10096–R10099 (1998)

[168] C. Luo, S. G. Johnson, J. D. Joannopoulos, and J. B. Pendry. *All-angle negative refraction without negative effective index.* Phys. Rev. B **65**:201104 (2002)

[169] C. Luo, S. Johnson, J. Joannopoulos, and J. Pendry. *Negative refraction without negative index in metallic photonic crystals.* Opt. Express **11**, 7:746–754 (2003)

[170] M. Davanco, Y. Urzhumov, and G. Shvets. *The complex Bloch bands of a 2D plasmonic crystal displaying isotropic negative refraction.* Opt. Express **15**, 15:9681–9691 (2007)

[171] J. Parsons, E. Hendry, J. R. Sambles, and W. L. Barnes. *Localized surface-plasmon resonances and negative refractive index in nanostructured electromagnetic metamaterials.* Phys. Rev. B **80**:245117 (2009)

[172] K. Sakoda. *Optical properties of photonic crystals.* Springer-Verlag, Heidelberg (2005)

[173] C. Soukoulis, ed. *Photonic band gap materials.* NATO ASI series: Applied sciences. Kluwer Academic Publishers (1996)

[174] S. Randhawa, M. U. González, J. Renger, S. Enoch, and R. Quidant. *Design and properties of dielectric surface plasmon bragg mirrors.* Opt. Express **18**, 14:14496–14510 (2010)

[175] J. A. Sanchez-Gil and A. A. Maradudin. *Surface-plasmon polariton scattering from a finite array of nanogrooves/ridges: Efficient mirrors.* Appl. Phys. Lett. **86**, 25:251106 (2005)

[176] H. Shin and S. Fan. *All-angle negative refraction for surface plasmon waves using a metal-dielectric-metal structure.* Phys. Rev. Lett. **96**:073907 (2006)

[177] V. M. Shalaev. *Optical negative-index metamaterials.* Nat. Phot. **1**:41–48 (2007)

[178] J. Valentine, S. Zhang, T. Zentgraf, E. Ulin-Avila, D. A. Genov, G. Bartal, and X. Zhang. *Three-dimensional optical metamaterial with a negative refractive index.* Nature **455**:376–379 (2008)

[179] H. Kosaka, T. Kawashima, A. Tomita, M. Notomi, T. Tamamura, T. Sato, and S. Kawakami. *Self-collimating phenomena in photonic crystals.* Appl. Phys. Lett. **74**, 9:1212–1214 (1999)

[180] P. T. Rakich, M. S. Dahlem, S. Tandon, M. Ibanescu, M. Soljačić, G. S. Petrich, J. D. Joannopoulos, L. A. Kolodziejski, and E. P. Ippen. *Achieving centimetre-scale supercollimation in a large-area two-dimensional photonic crystal.* Nat. Mater. **5**:93–96 (2006)

[181] J. Arlandis, E. Centeno, R. Pollès, A. Moreau, J. Campos, O. Gauthier-Lafaye, and A. Monmayrant. *Mesoscopic self-collimation and slow light in all-positive index layered photonic crystals.* Phys. Rev. Lett. **108**:037401 (2012)

[182] J. Durnin, J. J. Miceli, and J. H. Eberly. *Diffraction-free beams.* Phys. Rev. Lett. **58**:1499–1501 (1987)

[183] J. C. Gutiérrez-Vega, M. D. Iturbe-Castillo, and S. Chávez-Cerda. *Alternative formulation for invariant optical fields: Mathieu beams.* Opt. Lett. **25**, 20:1493–1495 (2000)

[184] G. A. Siviloglou, J. Broky, A. Dogariu, and D. N. Christodoulides. *Observation of accelerating Airy beams.* Phys. Rev. Lett. **99**:213901 (2007)

[185] A. Salandrino and D. N. Christodoulides. *Airy plasmon: a nondiffracting surface wave.* Opt. Lett. **35**, 12:2082–2084 (2010)

[186] A. Ashkin. *Acceleration and trapping of particles by radiation pressure.* Phys. Rev. Lett. **24**:156–159 (1970)

[187] A. Ashkin, J. M. Dziedzic, J. E. Bjorkholm, and S. Chu. *Observation of a single-beam gradient force optical trap for dielectric particles.* Opt. Lett. **11**, 5:288–290 (1986)

[188] M. Krishnan, N. Mojarad, P. Kukura, and V. Sandoghdar. *Geometry-induced electrostatic trapping of nanometric objects in a fluid.* Nature **467**:692–695 (2010)

[189] M. Righini, A. S. Zelenina, C. Girard, and R. Quidant. *Parallel and selective trapping in a patterned plasmonic landscape.* Nature Phys. **3**:477–480 (2007)

[190] M. L. Juan, M. Righini, and R. Quidant. *Plasmon nano-optical tweezers.* Nat. Phot. **5**:349–356 (2011)

[191] A. Cuche, O. Mahboub, E. Devaux, C. Genet, and T. W. Ebbesen. *Plasmonic coherent drive of an optical trap.* Phys. Rev. Lett. **108**:026801 (2012)

[192] L. N. Ng, M. N. Zervas, J. S. Wilkinson, and B. J. Luff. *Manipulation of colloidal gold nanoparticles in the evanescent field of a channel waveguide.* Appl. Phys. Lett. **76**, 15:1993–1995 (2000)

[193] K. Sasaki, J. ichi Hotta, K. ichiro Wada, and H. Masuhara. *Analysis of radiation pressure exerted on a metallic particle within an evanescent field.* Opt. Lett. **25**, 18:1385–1387 (2000)

[194] A. H. J. Yang, T. Lerdsuchatawanich, and D. Erickson. *Forces and transport velocities for a particle in a slot waveguide.* Nano Lett. **9**, 3:1182–1188 (2009)

[195] S. Lin, E. Schonbrun, and K. Crozier. *Optical manipulation with planar silicon*

microring resonators. Nano Lett. **10**, 7:2408–2411 (2010)

[196] P. C. Chaumet and M. Nieto-Vesperinas. *Time-averaged total force on a dipolar sphere in an electromagnetic field.* Opt. Lett. **25**, 15:1065–1067 (2000)

[197] L. Huang and O. J. F. Martin. *Reversal of the optical force in a plasmonic trap.* Opt. Lett. **33**, 24:3001–3003 (2008)

[198] S. H. Behrens and D. G. Grier. *The charge of glass and silica surfaces.* J. Chem. Phys. **115**, 14:6716–6721 (2001)

[199] J. C. Crocker and D. G. Grier. *Methods of digital video microscopy for colloidal studies.* J. Colloid Interface Sci. **179**, 1:298 – 310 (1996)

[200] V. Pelletier, N. Gal, P. Fournier, and M. L. Kilfoil. *Microrheology of microtubule solutions and actin-microtubule composite networks.* Phys. Rev. Lett. **102**:188303 (2009)

[201] M. D. Carbajal-Tinoco, R. Lopez-Fernandez, and J. L. Arauz-Lara. *Asymmetry in colloidal diffusion near a rigid wall.* Phys. Rev. Lett. **99**:138303 (2007)

[202] G. Volpe, L. Helden, T. Brettschneider, J. Wehr, and C. Bechinger. *Influence of noise on force measurements.* Phys. Rev. Lett. **104**:170602 (2010)

[203] U. Fano. *Effects of configuration interaction on intensities and phase shifts.* Phys. Rev. **124**:1866–1878 (1961)

[204] A. R. P. Rau. *Perspectives on the Fano resonance formula.* Phys. Scr. **69**, 1:C10 (2004)

[205] T. W. Ebbesen, H. J. Lezec, H. F. Ghaemi, T. Thio, and P. A. Wolff. *Extraordinary optical transmission through sub-wavelength hole arrays.* Nature **391**:667–669 (1998)

[206] C. Genet, M. van Exter, and J. Woerdman. *Fano-type interpretation of red shifts and red tails in hole array transmission spectra.* Opt. Commun. **225**:331 – 336 (2003)

[207] F. Hao, Y. Sonnefraud, P. V. Dorpe, S. A. Maier, N. J. Halas, and P. Nordlander. *Symmetry breaking in plasmonic nanocavities: Subradiant LSPR sensing and a tunable Fano resonance.* Nano Lett. **8**, 11:3983–3988 (2008)

[208] B. Luk'yanchuk, N. I. Zheludev, S. A. Maier, N. J. Halas, P. Nordlander, H. Giessen, and C. T. Chong. *The Fano resonance in plasmonic nanostructures and metamaterials.* Nat. Mater. **9**, 9:707–715 (2010)

[209] K. A. Tetz, L. Pang, and Y. Fainman. *High-resolution surface plasmon resonance sensor based on linewidth-optimized nanohole array transmittance.* Opt. Lett. **31**, 10:1528–1530 (2006)

[210] C. J. Alleyne, A. G. Kirk, R. C. McPhedran, N.-A. P. Nicorovici, and D. Maystre. *Enhanced SPR sensitivity using periodic metallic structures.* Opt. Express **15**, 13:8163–8169 (2007)

[211] S. Schuy and A. Janshoff. *Microstructuring of phospholipid bilayers on gold surfaces by micromolding in capillaries.* J. Colloid Interface Sci. **295**, 1:93 – 99 (2006)

[212] J. Renger, M. Kadic, G. Dupont, S. S. Aćimović, S. Guenneau, R. Quidant, and S. Enoch. *Hidden progress: broadband plasmonic invisibility.* Opt. Express **18**, 15:15757–15768 (2010)

[213] P. A. Huidobro, M. L. Nesterov, L. Martin-Moreno, and F. J. Garcia-Vidal. *Transformation optics for plasmonics.* Nano Lett. **10**, 6:1985–1990 (2010)

[214] H. Kim, J. Park, S.-W. Cho, S.-Y. Lee, M. Kang, and B. Lee. *Synthesis and dynamic switching of surface plasmon vortices with plasmonic vortex lens.* Nano Lett. **10**, 2:529–536 (2010)

Benedikt Alexander Hugo STEIN

Plasmonic Devices for Surface Optics and Refractive Index Sensing

Résumé

Ce manuscrit s'inscrit dans le contexte du contrôle de la propagation des plasmons de surface. A cet effet, des nanostructures diélectriques et métalliques ont été conçues et caractérisées par microscopie à champ de fuite dans les espaces réel et réciproque. La manipulation des plasmons de surface à l'aide de lentilles diélectriques et d'éléments à gradient d'indice est présentée, et la réfraction négative, la direction et l'auto-collimation des plasmons de surface dans des cristaux plasmoniques à une ou deux dimensions sont démontrées. Ces résultats ont été utilisés pour le guidage de nanoparticules à l'aide de forces optiques, ainsi que pour deux méthodes permettant de renforcer le facteur de mérite de sondes plasmoniques de variation d'indice de réfraction, basées l'une sur les résonances de Fano naturelles de la microscopie à champ de fuite, et pour la seconde sur les structures des bandes plasmoniques anisotropes.

Mots-clés: nano-optique, plasmons de surface, microscopie a champ de fuite, métamatériaux, cristaux plasmoniques, effet superprisme, réfraction négative, auto-collimation, micromanipulation optique, détection de variation d'indice, résonance de Fano

Résumé en anglais

In this thesis devices for controlling the flow of surface plasmon polaritons are described. Dielectric and metallic nanostructures were designed for this purpose, and characterized by leakage radiation microscopy in real and in reciprocal spaces. Manipulation of surface plasmons by dielectric lenses and gradient index elements is presented, and negative refraction, steering and self-collimation of surface plasmons in one- and two-dimensional plasmonic crystals is demonstrated. The achieved degree of control was applied for routing of nanoparticles by optical forces, as well as for two methods of enhancing the figures of merit of plasmonic refractive index sensors, based on the one hand on Fano resonances natural to leakage radiation microscopy, and on the other hand on anisotropic plasmonic bandstructures.

Keywords: nano-optics, surface plasmons, leakage radiation microscopy, metamaterials, plasmonic crystals, superprism effect, negative refraction, self-collimation, optical micromanipulation, refractive index sensing, Fano resonances